



3 1293 00639 4054

L

THESIS
C.1

This is to certify that the

dissertation entitled

Three-Dimensional Finite Element Analysis of the Flow
Field in Cylindrical Grain Storages.

presented by

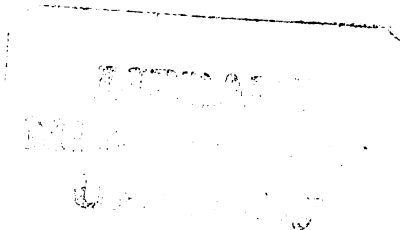
Vorapot Khompis

has been accepted towards fulfillment
of the requirements for

Ph.D. degree in Agricultural Engineering


Major professor

Date May 2, 1983



PLACE IN RETURN BOX to remove this checkout from your record.
TO AVOID FINES return on or before date due.

DATE DUE	DATE DUE	DATE DUE
FEB 2 1998 188	_____	_____
_____	_____	_____
_____	_____	_____
_____	_____	_____
_____	_____	_____
_____	_____	_____
_____	_____	_____

MSU is An Affirmative Action/Equal Opportunity Institution

c:\circ\date\due pm3-p.1

THREE-DIMENSIONAL FINITE ELEMENT ANALYSIS OF THE FLOW
FIELD IN CYLINDRICAL GRAIN STORAGES

By

Vorapot Khompis

A DISSERTATION

Submitted to
Michigan State University
in Partial fulfillment of the requirements
for the degree of

DOCTOR OF PHILOSOPHY

Department of Agricultural Engineering

1983

ABSTRACT

THREE-DIMENSIONAL FINITE ELEMENT ANALYSIS OF THE FLOW FIELD IN CYLINDRICAL GRAIN STORAGES

By

Vorapot Khompis

The purpose of this study was to use the three-dimensional finite element analysis to predict the pressure and velocity distributions in cylindrical grain storage using four perforated floor systems for aeration. The mathematics of airflow from the literature works were developed to get the three-dimensional nonlinear airflow equation. Shelled corn was selected as a grain media. The results of this study will provide a better understanding of the airflow patterns so design engineers may design an optimum cylindrical grain storage.

A three-dimensional finite element computer program was developed and used to calculate the pressure and velocity distributions in the cylindrical grain storages. Two and three-dimensional pressure and velocity distribution displays are presented.

The computer programs were written in general form to accomodate modification and use for future study. Suggestions for future work in optimizing the cylindrical grain storage are presented.

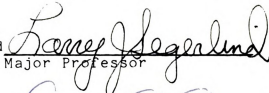
Vorapot Khompis

The computer results of the velocity distribution indicate that the velocity in the vertical direction plays a major role in the velocity distribution within the cylindrical grain storage. Apparent (or resultant) velocity was used for all of the velocity distribution displays.

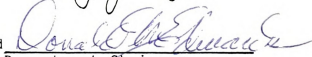
The results obtained in this study also indicate the minimum velocity regions for each type of the cylindrical grain storage.

The work demonstrates that the pressure and velocity distribution within the cylindrical grain storages are mostly effected by the perforated floor patterns.

Approved


Major Professor

Approved


Department Chairman

TO MY MOTHER'S SOUL

ACKNOWLEDGEMENTS

To all the individuals who have helped and encouraged me during the research and writing of this dissertation, I offer my sincere thanks. Foremost, appreciation is extended to my major professor, Dr. L. J. Segerlind, who supplied the original motivation and continues to give generously of his time and valuable consultation during the course of this work, as it made this portion of my program both a pleasing and a rewarding experience.

Other guidance committee members, Drs. M. C. Potter, R. C. Brook, and J. F. Steffe, are also warmly thanked for their constructive suggestions and interest in this work.

Grateful thanks are extended to Dr. F. W. Bakker-Arkema for providing numerous suggestions and valuable working experience.

Sincere appreciation is also extended to The Royal Thai Air Force for providing funds to finance my graduate program.

I extend my deepest gratitude to my mother and father for their continual understanding and encouragement throughout my academic endeavor.

TABLE OF CONTENTS

	Page
List of Tables	v
List of Figures	vi
Chapter	
I. INTRODUCTION	1
1.1 Background	1
1.2 Literature Review	2
1.3 Objectives	4
II. THE MATHEMATICS OF AIRFLOW	6
2.1 Assumptions and Fundamental Equations	6
2.2 The Governing Differential Equations	7
2.3 Field Equation Relates to Finite Element Method	9
III. SOLUTION TECHNIQUES	11
3.1 Finite Element Method	11
3.2 Finite Element Formulation	12
3.3 Solution Procedures	20
3.4 Application of Newton-Raphson Method	21
IV. COMPUTER PROGRAMMINGS	26
4.1 Sequences of Computer Program	26
4.1-1 The Finite Element Computer Program	26
4.1-2 Computer Program for the two-dimensional Cutting Plane	28
4.1-3 Three-Dimensional Display Computer Program	29
4.1-4 Developing Confidence in the Calculated Values	30
4.2 Types of the Cylindrical Grain Storage Under Study	31
4.3 Geometry	34
4.4 Input to the Program	34
4.4-1 Boundary Conditions	37
4.4-2 Grain Coefficients	38

V.	THE RESULTS FOR CYLINDRICAL GRAIN STORAGES	40
5.1	The Cutting Planes	40
5.2	Comments	45
5.3	Pressure and Velocity Distributions of The Total Perforated Floor System	45
5.4	Pressure and Velocity Distributions of The Straight Duct Perforated Floor System	46
5.5	Pressure and Velocity Distributions of The Square Duct Perforated Floor System	68
5.6	Pressure and Velocity Distributions of The Y-Duct Perforated Floor System	69
5.7	Three-Dimensional Pressure and Velocity Distribution Displays	90
VI.	CONCLUSIONS	113
VII.	SUGGESTIONS FOR FUTURE WORK	116
	BIBLIOGRAPHY	117

LIST OF TABLES

Table		Page
3-1	The shape functions for the twenty node prism element	17
3-2	Location of the sampling points and their weighting coefficients.	19
4-1	Sizes and perforated floor patterns of the cylindrical grain storages under study	31
4-2	Values of the pressure gradient and grain coefficients A and B for shelled corn	39

LIST OF FIGURES

Figure		Page
2-1	Relationships between the flow components and pressure gradients	8
3-1	The locations of the twenty nodes prism element	16
3-2	The location of cartesian and natural coordinates	18
3-3	The location of point $M(\bar{x}, \bar{y}, \bar{z})$ inside the twenty nodes element	22
4-1	A total perforated floor system (Type 1)	32
4-2	A straight duct perforated floor system (Type 2)	32
4-3	A square duct perforated floor system (Type 3)	33
4-4	A Y-duct perforated floor system (Type 4)	33
4-5	Cross-section of the elements in X-Y plane	35
4-6	Division into the elements of a half section of a half section of cylindrical grain storage	36
5-1a	Cutting plane: Type 1-1	42
5-1b	Cutting plane: Type 2-1	42
5-1c	Cutting plane: Type 3-1	42
5-1d	Cutting plane: Type 4-1P	42
5-2a	Cutting plane: Type 1-2, Type 2-2, Type 3-2, and Type 4-2	43
5-2b	Cutting plane: Type 1-3, Type 2-3, Type 3-3, and Type 4-3	43
5-3a	Full top grain configuration (Type 1F)	44
5-3b	Cutting plane: Type 1F-1F	44
5-3c	Cutting plane: Type 1F-3F	44



5-4a	Locations of the grid-elements on the cutting plane (Type 1-1)	47
5-4b	Locations of the grid-elements on the cutting plane (Type 1-2, 1-3, and 1F-3F)	48
5-4c	Pressure distribution (Type 1-1) in percent of perforated floor pressure	49
5-4d	Pressure distribution (Type 1-2) in percent of perforated floor pressure	50
5-4e	Pressure distribution (Type 1-3) in percent of perforated floor pressure	51
5-4f	Velocity distribution (Type 1-1) in m/min.	52
5-4g	Velocity distribution (Type 1-2) in m/min.	53
5-4h	Velocity distribution (Type 1-3) in m/min.	54
5-5a	Locations of the grid-elements on the cutting plane (Type 1F-1F)	55
5-5b	Pressure distribution (Type 1F-1F) in percent of perforated floor pressure	56
5-5c	Pressure distribution (Type 1F-3F) in percent of perforated floor pressure	57
5-5d	Velocity distribution (Type 1F-1F) in m/min.	58
5-5e	Velocity distribution (Type 1F-3F) in m/min.	59
5-6a	Locations of the grid-elements on the cutting plane (Type 2-1)	60
5-6b	Locations of the grid-elements on the cutting plane (Type 2-2, 2-3)	61
5-6c	Pressure distribution (Type 2-1) in percent of perforated floor pressure	62
5-6d	Pressure distribution (Type 2-2) in percent of perforated floor pressure	63
5-6e	Pressure distribution (Type 2-3) in percent of perforated floor pressure	64
5-6f	Velocity distribution (Type 2-1) in m/min.	65
5-6g	Velocity distribution (Type 2-2) in m/min.	66
5-6h	Velocity distribution (Type 2-3) in m/min.	67

5-6i	The minimum velocity regions of the straight duct perforated floor system	70
5-7a	Locations of the grid-elements on the cutting plane (Type 3-1)	71
5-7b	Locations of the grid-elements on the cutting plane	72
5-7c	Pressure distribution (Type 3-1) in percent of perforated floor pressure	73
5-7d	Pressure distribution (Type 3-2) in percent of perforated floor pressure	74
5-7e	Pressure distribution (Type 3-3) in percent of perforated floor pressure	75
5-7f	Velocity distribution (Type 3-1) in m/min.	76
5-7g	Velocity distribution (Type 3-2) in m/min.	77
5-7h	Velocity distribution (Type 3-3) in m/min.	78
5-7i	The minimum velocity regions of the square duct perforated floor system	79
5-8a	Locations of the grid-elements on the cutting plane (Type 4-1P)	80
5-8b	Locations of the grid-elements on the cutting plane (Type 4-2, 4-3)	81
5-8c	Pressure distribution (Type 4-1P) in percent of perforated floor pressure	82
5-8d	Pressure distribution (Type 4-2) in percent of perforated floor pressure	84
5-8e	Pressure distribution (Type 4-3) in percent of perforated floor pressure	85
5-8f	Velocity distribution (Type 4-1P) in m/min.	86
5-8g	Velocity distribution (Type 4-2) in m/min.	87
5-8h	Velocity distribution (type 4-3) in m/min.	88
5-8i	The minimum velocity regions of the Y-duct perforated floor system	89
5-9a	Constant pressure surface for the straight duct perforated floor system (at azimuth = 30)	91

5-9b	Constant pressure surface for the straight duct perforated floor system (at azimuth = 115)	92
5-9c	Constant pressure surface for the straight duct perforated floor system (at azimuth = -30)	93
5-10a	Constant velocity surface for the straight duct perforated floor system (at azimuth = 30)	94
5-10b	Constant velocity surface for the straight duct perforated floor system (at azimuth = 115)	95
5-10c	Constant velocity surface for the straight duct perforated floor system (at azimuth = -30)	96
5-11a	Constant pressure surface for the square duct perforated floor system (at azimuth = 30)	97
5-11b	Constant pressure surface for the square duct perforated floor system (at azimuth = 115)	98
5-11c	Constant pressure surface for the square duct perforated floor system (at azimuth = -30)	99
5-12a	Constant velocity surface for the square duct perforated floor system (at azimuth = 30)	100
5-12b	Constant velocity surface for the square duct perforated floor system (at azimuth = 115)	101
5-12c	Constant velocity surface for the square duct perforated floor system (at azimuth = -30)	102
5-13a	Constant pressure surface for the Y-duct perforated floor system (at azimuth = 30)	103
5-13b	Constant pressure surface for the Y-duct perforated floor system (at azimuth = 115)	104
5-13c	Constant pressure surface for the Y-duct perforated floor system (at azimuth = -30)	105
5-14a	Constant velocity surface for the Y-duct perforated floor system (at azimuth = -30)	106
5-14b	Constant velocity surface for the Y-duct perforated floor system (at azimuth = 115)	107
5-14c	Constant velocity surface for the Y-duct perforated floor system (at azimuth = -30)	108



CHAPTER I

INTRODUCTION

1.1 BACKGROUND

Air flowing through an agricultural product accomplishes one or more of the following objectives. Heating or cooling of the product and/or the addition or removal of moisture. The efficiency at which it accomplishes any of these functions depends on how it is introduced and flows through the bin or storage holding the commodity.

When air is forced through a layer of an agricultural product, resistance to the airflow is called pressure drop. The pressure drop develops as a result of the energy lost through friction and turbulence. The pressure drop for airflow through any product depends on the rate of airflow, the surface and shape characteristics of the product, the number, size and configuration of the voids, the depth of the product bed, and the variability of the particle size.

Uniform airflow is more efficient than nonuniform airflow because all locations in a particular plane receive the same treatment. The introduction of air uniformly into a product does not guarantee that it will remain uniform. Uneven distribution of fine material in a bulk storage of shelled corn, for example, changes the resistance to airflow



resulting in a nonuniform airflow.

Structural design and handling characteristics often dictate that air be introduced through a system of ducts. This produces a two or three-dimensional flow pattern. It is important that the designer be able to locate these ducts such that all parts of the storage receives enough air to accomplish the objectives associated with the air.

The knowledge and computational equipment for calculating the airflow patterns in bins or storages exists. The engineer should always make use of this information when designing airflow systems. This dissertation should contribute to his (or her) understanding of the airflow phenomenon and ease the work required to complete the design.

1.2 LITERATURE REVIEW

The flow of air through grain storages has been extensively studied (Ergun, 1952). However, the effects of nonuniform distribution of voids in grain storages are not well understood even though flow maldistribution contributes greatly to bacteria activity and hot spot generation. Problems of this type have been studied by several researchers.

Brooker (1961) generalized information given by Shedd (1951) to obtain the pressure equation for two-dimensional airflow. This differential equation was solved numerically using the finite difference method. The results agreed very well with experimental pressure values measured in a rectangular bin containing wheat.

Bunn and Hukill (1963) developed the two-dimensional linear and nonlinear airflow equations on the basis of their experiment that expressed the relation of the air velocity to the pressure gradient for air flow through a bed of packed shots.

Brooker (1969) developed the finite difference method to calculate the pressure and velocity distribution for two-dimensional linear airflow in a rectangular bin of shelled corn. His calculated values did not agree well with experimental measurements.

Jindal and Thomson (1972) modified Brooker's model and adapted it to triangular piles of sorghum to calculate the pressure distribution.

Pierce and Thomson (1975) subsequently modified the Jindal and Thomson's model for prediction of airflow patterns in a conical shaped pile of sorghum and corn. It is unclear in the paper whether the grain coefficient varied within the pile or remained constant.

Marchant (1976a) used the finite difference method to estimate the total airflow through large hay bales and included a small portion of three-dimensional airflow.

Marchant (1976b) used the finite element method to solve the linear airflow problem in two-dimensions. The experiments of Brooker (1958) and Barrowman and Boyce (1966) were used to verify the solution procedure.

Lai (1980) calculated the three-dimensional pressure and velocity distribution in a circular grain bin using the method of lines. This method is similar to the finite



difference method in that the pressure at a point is obtained in terms of the pressure values at the surrounding mesh points. Smith (1982) claims the line method generates excessive computing costs.

Segerlind (1982) developed the model for two-dimensional nonlinear airflow and used the finite element method to solve for the pressure patterns in a rectangular bin. The solution procedure used the six node quadratic triangular element. The element stiffness matrix numerically evaluated using a five point integration technique. The location of the isopressure lines for nonlinear flow through shelled corn were similar to the lines measured by Brooker (1969).

Smith (1982) applied the two-dimensional finite element method used by Marchant (1976a) to estimate the pressure and velocity distributions in the three-dimensional field of a rectangular grain heap (on-floor monoduct system). The solution of the non-linear equations was simulated by the frontal solution routine. His calculated results did not agree well with experimental results of Marchant (1976a). Air velocity was less accurate than the pressure with most of the error arises in regions of high velocity. The results indicated the computation time was relatively high.

1.3 OBJECTIVES

A review of the literature indicates that there does not exist a study which calculates the three-dimensional pressure and velocity fields in the cylindrical grain storage.



The specific objectives of this work are:

1. To unify the mathematical concepts related to the airflow through a granular material.
2. To develop the mathematics for the three-dimensional airflow problem along the lines which allow a finite element solution of the problem.
3. To develop the three-dimensional finite element computer program to solve for the pressure and velocity distributions in cylindrical grain storages.
4. To present the two- and three-dimensional pressure and velocity distribution displays for some typical (aeration) cylindrical grain storage situations.



CHAPTER II
THE MATHEMATICS OF AIRFLOW

The airflow patterns within a granular material can be established because the pressure distribution within the mass satisfies a specific differential equation. The objective of this chapter is to develop the governing differential equation for three-dimensional airflow.

2.1 ASSUMPTIONS AND FUNDAMENTAL EQUATIONS

Air flowing through a homogeneous mass is assumed to flow in a direction perpendicular to the lines of constant pressure, iso-pressure lines. The velocity is assumed to be related to the pressure gradient. This relationship was proposed by Shedd (1951) of the form

$$V_n = A \left(\frac{\partial P}{\partial n} \right)^B \quad (2-1)$$

V_n = the flow (apparent) velocity

P = the air pressure

A and B are experimentally determined grain coefficients.

The pressure gradients behave vectorally, that is, the gradients in the x , y and z directions are related to the gradient in the direction of flow by

$$\left(\frac{\partial P}{\partial n} \right)^2 = \left(\frac{\partial P}{\partial x} \right)^2 + \left(\frac{\partial P}{\partial y} \right)^2 + \left(\frac{\partial P}{\partial z} \right)^2 \quad (2-2)$$



It is assumed that the velocity components in the x, y and z directions, V_x , V_y , and V_z are related to V_n in proportion to the pressure gradients, that is

$$V_x = \left(\frac{\partial P}{\partial x}\right) \left(\frac{\partial P}{\partial n}\right)^{-1} V_n \quad (2-3a)$$

$$V_y = \left(\frac{\partial P}{\partial y}\right) \left(\frac{\partial P}{\partial n}\right)^{-1} V_n \quad (2-3b)$$

$$V_z = \left(\frac{\partial P}{\partial z}\right) \left(\frac{\partial P}{\partial n}\right)^{-1} V_n \quad (2-3c)$$

The relationships for V_x and V_y are illustrated in Figure 2-1.

The desired differential equation is a direct result of utilizing (2-1), (2-2), and (2-3) in conjunction with the continuity equation for incompressible and steady flow. The continuity equation relates the velocity gradients and is

$$\frac{\partial V_x}{\partial x} + \frac{\partial V_y}{\partial y} + \frac{\partial V_z}{\partial z} = 0 \quad (2-4)$$

2.2 THE GOVERNING DIFFERENTIAL EQUATION

To obtain the governing differential equation we begin by eliminating V_n from the velocity component equation (2-3) using (2-1). Considering V_x we have

$$\begin{aligned} V_x &= \left(\frac{\partial P}{\partial x}\right) \left(\frac{\partial P}{\partial n}\right)^{-1} V_n \\ &= \left(\frac{\partial P}{\partial x}\right) \left(\frac{\partial P}{\partial n}\right)^{-1} A \left(\frac{\partial P}{\partial n}\right)^B \\ V_x &= A \left(\frac{\partial P}{\partial x}\right) \left(\frac{\partial P}{\partial n}\right)^{B-1} \end{aligned} \quad (2-5a)$$

Proceeding in a similar manner

$$V_y = A \left(\frac{\partial P}{\partial y}\right) \left(\frac{\partial P}{\partial n}\right)^{B-1} \quad (2-5b)$$

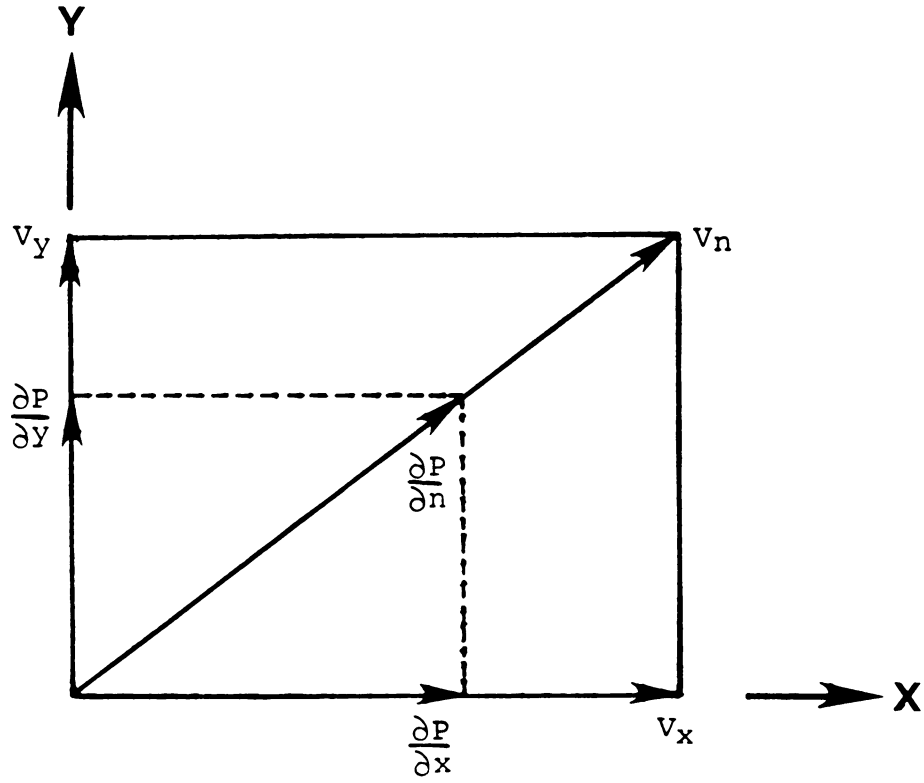


Figure 2-1. Relationships between the flow components and pressure gradients.

$$V_z = A \left(\frac{\partial P}{\partial z} \right) \left(\frac{\partial P}{\partial n} \right)^{B-1} \quad (2-5c)$$

The velocity gradients can be written in terms of the components of the pressure gradients by using (2-2) to eliminate $\frac{\partial P}{\partial n}$. This manipulation appears as

$$\begin{aligned} \left(\frac{\partial P}{\partial n} \right)^{B-1} &= \left[\left(\frac{\partial P}{\partial n} \right)^2 \right]^{\frac{B-1}{2}} \\ &= \left[\left(\frac{\partial P}{\partial x} \right)^2 + \left(\frac{\partial P}{\partial y} \right)^2 + \left(\frac{\partial P}{\partial z} \right)^2 \right]^{\frac{B-1}{2}} \end{aligned} \quad (2-6)$$

Replacing $\left(\frac{\partial P}{\partial n} \right)^{B-1}$ in each of (2-5) yields the velocity components

$$V_x = C \frac{\partial P}{\partial x} \quad (2-7a)$$

$$V_y = C \frac{\partial P}{\partial y} \quad (2-7b)$$

$$V_z = C \frac{\partial P}{\partial z} \quad (2-7c)$$

$$\text{where } C = A \left[\left(\frac{\partial P}{\partial x} \right)^2 + \left(\frac{\partial P}{\partial y} \right)^2 + \left(\frac{\partial P}{\partial z} \right)^2 \right]^{\frac{B-1}{2}} \quad (2-8)$$

The coefficient C is a granular permeability and is a function of x, y and z because A, B and P each are functions of x, y and z.

Substitute (2-7a), (2-7b) and (2-7c) into the continuity equation (2-4) yields

$$\frac{\partial}{\partial x} \left(C \frac{\partial P}{\partial x} \right) + \frac{\partial}{\partial y} \left(C \frac{\partial P}{\partial y} \right) + \frac{\partial}{\partial z} \left(C \frac{\partial P}{\partial z} \right) = 0 \quad (2-9)$$

which is the governing differential equation for pressure distribution within a three-dimensional mass of grain.

2.3 FIELD EQUATION RELATES TO FINITE ELEMENT METHOD

Equation (2-9) is one form of the field equation

$$\frac{\partial}{\partial x} \left(K \frac{\partial \phi}{\partial x} \right) + \frac{\partial}{\partial y} \left(K \frac{\partial \phi}{\partial y} \right) + \frac{\partial}{\partial z} \left(K \frac{\partial \phi}{\partial z} \right) + Q = 0$$

(2-10)

which occurs in the physically important areas of heat transfer, groundwater flow and solid mechanics. Equation (2-10) has an integral formulation which is the basis of the finite element method, a numerical solution technique which is applicable to irregular shapes with segmented boundary conditions. Equation (2-9) can be solved using the same technique except that the solution is an iteration process because the coefficient C is a function of x , y , z and P . The integral formulation and boundary conditions are discussed in the next chapter.

CHAPTER III
SOLUTION TECHNIQUES

3.1 FINITE ELEMENT METHOD

The finite element method is a numerical procedure for solving problems many areas of engineering. Its initial area of application was structural analysis but it then expanded to the solid mechanics problems of plates and shells. A finite formulation for the field equation

$$\frac{\partial}{\partial x} \left(k \frac{\partial \phi}{\partial x} \right) + \frac{\partial}{\partial y} \left(k \frac{\partial \phi}{\partial y} \right) + \frac{\partial}{\partial z} \left(k \frac{\partial \phi}{\partial z} \right) + Q = 0 \quad (3-1)$$

was found in the early 1960's and its application was immediately extended to include heat conduction, confined groundwater flow and the other physical problems governed by a form of (3-1). Finite element applications now also include time dependent field problem and fluid dynamics.

The finite element method has nearly replaced the finite difference method when solving the steady-state field equation (3-1). The superior aspect of the finite element method is not necessarily more accurate results but the generalness of the formulation. A computer program can be written that is independent of the boundary shape analyzed and the points at which the unknown parameter is to be calculated. Furthermore, many of the subroutines needed to solve a heat transfer problem are identical to those needed

to solve a solid mechanics problem. Once a subroutine has been written and checked, it can be used to solve many types of problems. Contrast this fact with the need to rewrite a finite difference program each time the grid is modified.

One other comparison is important. All of the grid points for a finite element model are either on the boundary or within the region. There are no points outside the region as there can be for the finite difference model.

There are several references covering the finite element method. Segerlind (1976) and Desai (1979) cover the basic concepts at a beginning level. Zienkiewicz (1978) is more advanced and also covers a broader range of applications.

3.2 FINITE ELEMENT FORMULATION

The pair of equations which govern nonlinear airflow within a grain storage are (2-8) and (2-9).

$$\frac{\partial}{\partial x}(C \frac{\partial P}{\partial x}) + \frac{\partial}{\partial y}(C \frac{\partial P}{\partial y}) + \frac{\partial}{\partial z}(C \frac{\partial P}{\partial z}) = 0$$

where

$$C = A \left[\left(\frac{\partial P}{\partial x} \right)^2 + \left(\frac{\partial P}{\partial y} \right)^2 + \left(\frac{\partial P}{\partial z} \right)^2 \right]^{\frac{B-1}{2}} \quad (3-2)$$

(3-3)

These two equations must be solved simultaneously in iterative fashion since C is nonlinear in P.

Equation (3-2) is the general form of the field equation. There is a wealth of information available for solving this equation using finite element method, (Segerlind (1976) and Zienkiewicz (1978)). An approximate solution to (3-2) can be obtained by using continuous piecewise smooth

functions to approximate P while minimizing the functional given by Segerlind (1976) as

$$\Pi = \int_V \frac{C}{2} \left[\left(\frac{\partial P}{\partial x} \right)^2 + \left(\frac{\partial P}{\partial y} \right)^2 + \left(\frac{\partial P}{\partial z} \right)^2 \right] dV \quad (3-4)$$

where C is considered to be a constant for any particular solution step.

Application of the finite element method to the solution of (3-2) by minimizing (3-4) is discussed in Segerlind (1976).

The twenty node prism element in Figure 3-1 was used in this study.

The element stiffness matrix is given by Segerlind (1976) as

$$[k^{(e)}] = \int_V [B]^T [D] [B] dV \quad (3-5)$$

where V is the volume of the element, [D] is a diagonal matrix with the value of C for each diagonal entry and [B] is a matrix related to the derivatives of the shape functions. The element has twenty shape (interpolating) functions. If the shape functions are contained in a row vector [N] where

$$[N] = [N_1 \ N_2 \ N_3 \ \dots \ N_{20}]$$

Then

$$[B] = \begin{bmatrix} \partial N_1 / \partial x & \partial N_2 / \partial x & \dots & \partial N_{20} / \partial x \\ \partial N_1 / \partial y & \partial N_2 / \partial y & \dots & \partial N_{20} / \partial y \\ \partial N_1 / \partial z & \partial N_2 / \partial z & \dots & \partial N_{20} / \partial z \end{bmatrix}$$

The shape functions for the element in Figure 3-1 are given in Table 3-1 and are those given by Zienkiewicz (1978).

The element matrix defined by (3-5) can be evaluated using numerical integration techniques. The numerical integration of an equation of this type is discussed by Segerlind (1976). The numerical integration requires a change of variables from the (x,y,z) coordinate system to the natural coordinate system (ξ, η, ζ), where each coordinate variable varies between -1 and +1. Figure 3-2 shows of these two coordinate systems with the origin is at the center of the element. The equation for the change of integration variables is given by Segerlind (1976) as

$$dV = dx.dy.dz = |\det[J]| \cdot d\xi d\eta d\zeta \quad (3-6a)$$

where [J] is the Jacobian matrix of the transformation given by

$$[J] = \begin{bmatrix} \partial x / \partial \xi & \partial y / \partial \xi & \partial z / \partial \xi \\ \partial x / \partial \eta & \partial y / \partial \eta & \partial z / \partial \eta \\ \partial x / \partial \zeta & \partial y / \partial \zeta & \partial z / \partial \zeta \end{bmatrix} \quad (3-6b)$$

The matrix [B] for the natural coordinate system is

$$[B(\xi, \eta, \zeta)] = [J]^{-1} \begin{bmatrix} \partial N_i / \partial \xi \\ \partial N_i / \partial \eta \\ \partial N_i / \partial \zeta \end{bmatrix} \quad (3-6c)$$

where $N_i = N_i(\xi, \eta, \zeta)$ and $i = 1, 2, 3, \dots, 20$

Substituting (3-6a), (3-6b) and (3-6c) into equation (3-5), the element stiffness matrix is

$$[k^{(e)}] = \int_{-1}^1 \int_{-1}^1 \int_{-1}^1 [B(\xi, \eta, \zeta)]^T [D] [B(\xi, \eta, \zeta)] |\det[J]| d\xi d\eta d\zeta \quad (3-7)$$

For twenty node prism elements, twenty seven Gauss Legendre integration points are required to numerically integrate the volume integral (3-7) (Seegerlind, 1976). The location of these integration points and their weighting coefficient are given in Table 3-2. The integral (3-7) is written as the sum

$$[k^{(e)}] = \sum_{i=1}^3 \sum_{j=1}^3 \sum_{k=1}^3 [f(\xi_i, \eta_j, \zeta_k) W_{ijk}] \quad (3-8)$$

where $f(\xi_i, \eta_j, \zeta_k) = [B]^T [D] [B] \cdot |\det[J]|$

and W_{ijk} are the weighting coefficients from Table 3-2 (Gauss-Legendre quadrature order 3) (Seegerlind, 1976).

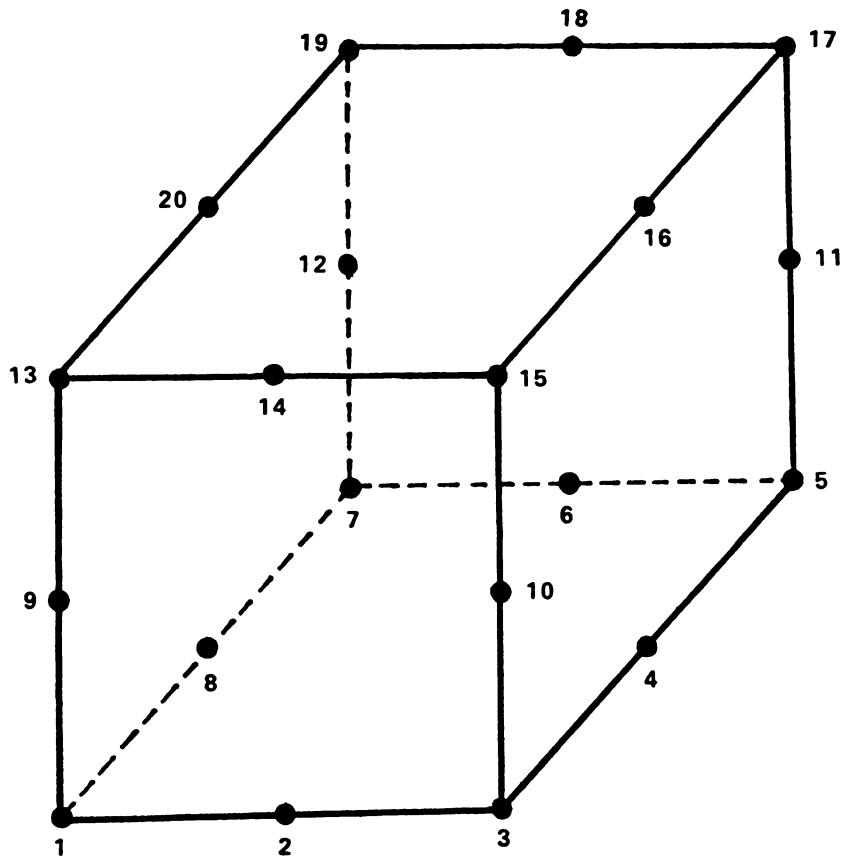


Figure 3-1. The locations of the twenty node prism element.

Table 3-1. The shape functions for the twenty node prism element.

$$\begin{aligned}
 N_1 &= 1/8(\xi-1)(1-\eta)(1-\zeta)(\xi+\eta+\zeta+2) \\
 N_2 &= 1/4(1-\xi^2)(1-\eta)(1-\zeta) \\
 N_3 &= 1/8(1+\xi)(1-\eta)(1-\zeta)(\xi-\eta-\zeta-2) \\
 N_4 &= 1/4(1-\eta^2)(1+\xi)(1-\zeta) \\
 N_5 &= 1/8(1+\xi)(1+\eta)(1-\zeta)(\xi+\eta-\zeta-2) \\
 N_6 &= 1/4(1-\xi^2)(1+\eta)(1-\zeta) \\
 N_7 &= 1/8(1-\xi)(1+\eta)(1-\zeta)(\eta-\xi-\zeta-2) \\
 N_8 &= 1/4(1-\eta^2)(1-\xi)(1-\zeta) \\
 N_9 &= 1/4(1-\zeta^2)(1-\xi)(1-\eta) \\
 N_{10} &= 1/4(1-\zeta^2)(1+\xi)(1-\eta) \\
 N_{11} &= 1/4(1-\zeta^2)(1+\xi)(1+\eta) \\
 N_{12} &= 1/4(1-\zeta^2)(1-\xi)(1+\eta) \\
 N_{13} &= 1/8(1-\xi)(1-\eta)(1+\zeta)(\zeta-\xi-\eta-2) \\
 N_{14} &= 1/4(1-\xi^2)(1-\eta)(1+\zeta) \\
 N_{15} &= 1/8(1+\xi)(1-\eta)(1+\zeta)(\xi-\eta+\zeta-2) \\
 N_{16} &= 1/4(1-\eta^2)(1+\zeta)(1+\xi) \\
 N_{17} &= 1/8(1-\xi^2)(1+\eta)(1+\zeta)(\xi+\eta+\zeta-2) \\
 N_{18} &= 1/4(1-\xi^2)(1+\eta)(1+\zeta) \\
 N_{19} &= 1/8(1-\xi)(1+\eta)(1+\zeta)(\eta+\zeta-\xi-2) \\
 N_{20} &= (1-\eta^2)(1-\xi)(1+\zeta)/4
 \end{aligned}$$

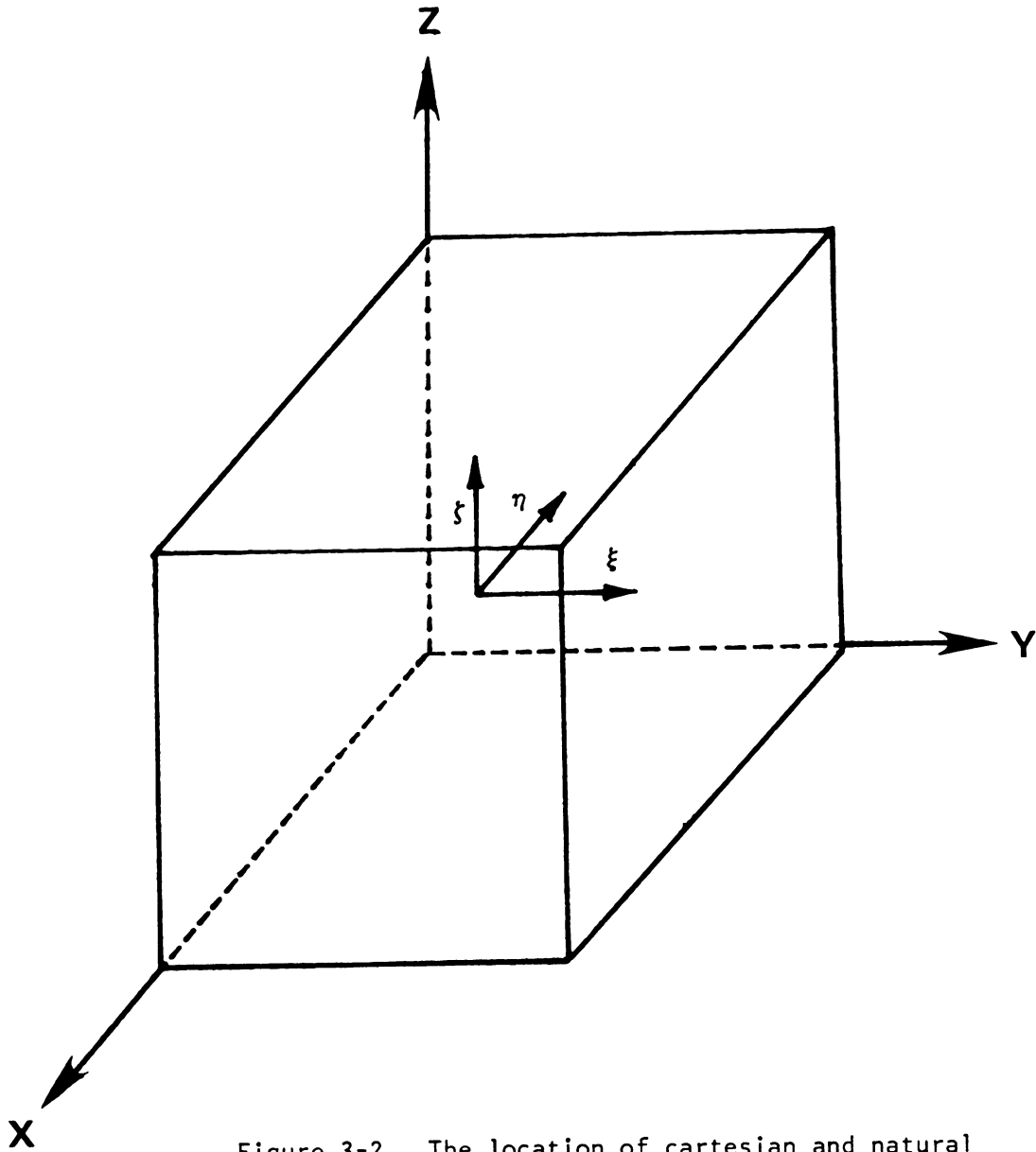


Figure 3-2. The location of cartesian and natural coordinates.

Table 3-2. Locations of the sampling points and their weighting coefficients.

ξ	η	ζ	W
0	0	0	Q^3
		$\underline{+P}$	Q^2R
0	$+P$	0	Q^2R
		$\underline{+P}$	QR^2
0	$-P$	0	Q^2R
		$\underline{+P}$	QR^2
$+P$	0	0	Q^2R
		$\underline{+P}$	QR^2
$+P$	$+P$	0	QR^2
		$\underline{+P}$	R^3
$+P$	$-P$	0	QR^2
		$\underline{+P}$	R^3
$-P$	0	0	Q^2R
		$\underline{+P}$	QR^2
$-P$	$+P$	0	QR^2
		$\underline{+P}$	R^3
$-P$	$-P$	0	QR^2
		$\underline{+P}$	R^3

$$P = 0.774597, Q = 8/9 \text{ and } R = 5/9$$

The system of linear equation is

$$[K]\{P\} = \{0\} \quad (3-9)$$

$$\text{where } [K] = \sum_{e=1}^n [k^{(e)}] \quad (3-10)$$

and the summation is done in the direct stiffness sense (Seegerlind, 1976).

The system of equations defined by (3-9) must be modified to include the nonzero values of $\{P\}$. Once this is done, the right hand column vector contains nonzero values and the system has a solution.

3.3 SOLUTION PROCEDURES

The governing airflow equation, (3-2), is nonlinear; thus, the solution must be obtained using an iterative procedure. The coefficient C in (3-3) is set equal to one on the first iteration. This reduces (3-2) to

$$\frac{\partial^2 P_2}{\partial x^2} + \frac{\partial^2 P_2}{\partial y^2} + \frac{\partial^2 P_2}{\partial z^2} = 0 \quad (3-11)$$

which is the three-dimensional form of Laplace's equation. On the second and all following iterations, the pressure value at each node exists and the coefficient C is calculated. The iterative process continues until the difference between the nodal values on the successive iterations is less than a prescribed value (say 0.001 in. of water or 0.25 pascals).

The airflow velocity is calculated from

$$V_n = A \left[\left(\frac{\partial P}{\partial x} \right)^2 + \left(\frac{\partial P}{\partial y} \right)^2 + \left(\frac{\partial P}{\partial z} \right)^2 \right] \frac{B}{2} \quad (3-12)$$

Once the pressure pattern is established. The values of A and B in (3-12) usually are not constant over a wide range of airflow velocities and pressure gradients. In fact

A and B can vary from location to location if there are fines in the product being analyzed. The correct values of A and B at each node were based on the pressure gradient at the point where the nodal velocity value was calculated. Again, appropriate values of A and B are selected according to the magnitude of the pressure gradient.

3.4 APPLICATION OF NEWTON - RAPHSON METHOD

In order to display the pressure and velocity distributions inside the cylindrical grain storage, the grain storage was cut by a plane at a selected location. A two-dimensional grid was generated on the a plane. Since the cartesian coordinates (x,y,z) of each node on the cutting plane were known, it was necessary to determine the natural coordinate (ξ, η, ζ) values in order to calculate the desired quantities.

Assume a point $M(\bar{x}, \bar{y}, \bar{z})$ within the twenty node prism element as shown in Figure 3-3. The cartesian coordinates can be written in terms of the nodal values using

$$x = [N]\{X\} \quad (3-13a)$$

$$y = [N]\{Y\} \quad (3-13b)$$

$$z = [N]\{Z\} \quad (3-13c)$$

(Segerlind, 1976)

where [N] is a row matrix containing the shape functions in Table 3-1. The column matrix {X}, {Y} and {Z} are the cartesian coordinate of the twenty nodes.

Rearranging (3-13a) through (3-13c)

$$F1 (\xi, \eta, \zeta) = [N]\{X\} - \bar{x} = 0 \quad (3-14a)$$

$$F2 (\xi, \eta, \zeta) = [N]\{Y\} - \bar{y} = 0 \quad (3-14b)$$

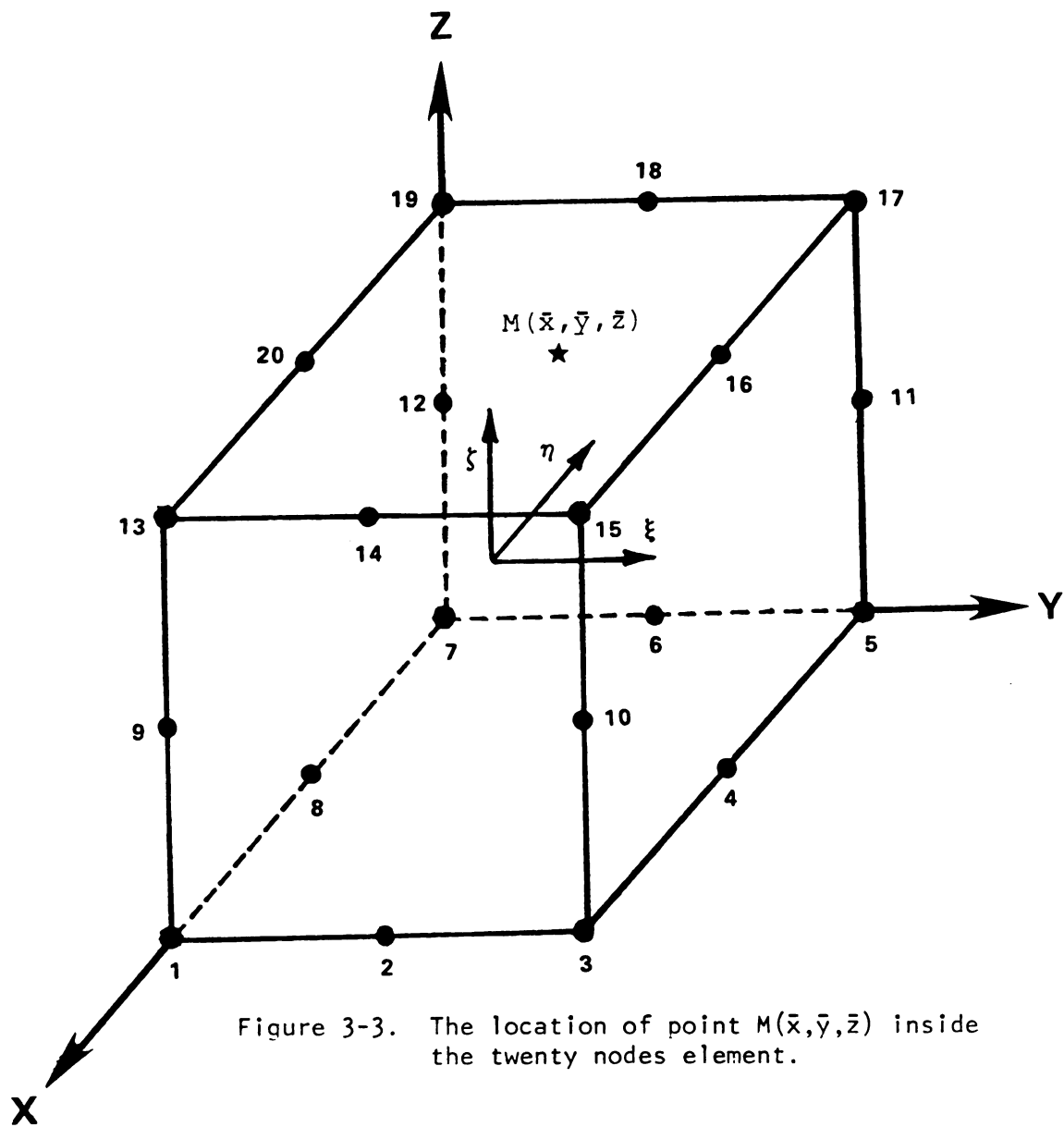


Figure 3-3. The location of point $M(\bar{x}, \bar{y}, \bar{z})$ inside the twenty nodes element.

$$F3(\xi, \eta, \zeta) = [N]\{Z\} - \bar{z} = 0 \quad (3-14c)$$

Equations (3-14a), (3-14b), and (3-14c) are nonlinear equations containing the three independent variables ξ , η and ζ .

Let a_1 , b_1 and c_1 be the first approximation value of ξ , η , and ζ then

$$\begin{aligned} F1(a_1 + \Delta\xi, b_1 + \Delta\eta, c_1 + \Delta\zeta) &= F1(a_1, b_1, c_1) \\ &+ \Delta\xi \frac{\partial F1(a_1, b_1, c_1)}{\partial \xi} + \Delta\eta \frac{\partial F1(a_1, b_1, c_1)}{\partial \eta} \\ &+ \Delta\zeta \frac{\partial F1(a_1, b_1, c_1)}{\partial \zeta} \end{aligned} \quad (3-15)$$

Similar equations can be written for $F2$ and $F3$.

From (3-14) and (3-15) we obtain

$$F1 + \Delta\xi \frac{\partial F1}{\partial \xi} + \Delta\eta \frac{\partial F1}{\partial \eta} + \Delta\zeta \frac{\partial F1}{\partial \zeta} = 0 \quad (3-15a)$$

$$F2 + \Delta\xi \frac{\partial F2}{\partial \xi} + \Delta\eta \frac{\partial F2}{\partial \eta} + \Delta\zeta \frac{\partial F2}{\partial \zeta} = 0 \quad (3-15b)$$

$$F3 + \Delta\xi \frac{\partial F3}{\partial \xi} + \Delta\eta \frac{\partial F3}{\partial \eta} + \Delta\zeta \frac{\partial F3}{\partial \zeta} = 0 \quad (3-15c)$$

Assume a starting set of values for ξ , η , and ζ and arrange a matrix to solve

$$\begin{bmatrix} \partial F1 / \partial \xi & \partial F1 / \partial \eta & \partial F1 / \partial \zeta \\ \partial F2 / \partial \xi & \partial F2 / \partial \eta & \partial F2 / \partial \zeta \\ \partial F3 / \partial \xi & \partial F3 / \partial \eta & \partial F3 / \partial \zeta \end{bmatrix} \begin{bmatrix} \Delta\xi \\ \Delta\eta \\ \Delta\zeta \end{bmatrix} = \begin{bmatrix} -F1 \\ -F2 \\ -F3 \end{bmatrix} \quad (3-16)$$

The solution for $\Delta\xi$ is

$$\Delta\xi = \frac{\begin{vmatrix} -F1 & \partial F1/\partial\eta & \partial F1/\partial\zeta \\ -F2 & \partial F2/\partial\eta & \partial F2/\partial\zeta \\ -F3 & \partial F3/\partial\eta & \partial F3/\partial\zeta \end{vmatrix}}{\begin{vmatrix} \partial F1/\partial\xi & \partial F1/\partial\eta & \partial F1/\partial\zeta \\ \partial F2/\partial\xi & \partial F2/\partial\eta & \partial F2/\partial\zeta \\ \partial F3/\partial\xi & \partial F3/\partial\eta & \partial F3/\partial\zeta \end{vmatrix}} \quad (3-17)$$

and $\Delta\eta$ and $\Delta\zeta$ can be found in a similar manner.

Note that $F1 = [N]\{X\} - \bar{x}$

$$\begin{aligned} \partial F1/\partial\xi &= \sum_{i=1}^{20} \frac{\partial N_i}{\partial\xi} X_i \\ \xi_{\text{new}} &= \xi_{\text{old}} + \Delta\xi \end{aligned} \quad (3-18)$$

and so forth for $F2$, $F3$, η and ζ

New values of ξ , η and ζ are recalculated until $\Delta\xi$, $\Delta\eta$ and $\Delta\zeta$ become zero (≤ 0.001).

Once the appropriate values of ξ , η and ζ are available using the above iteration, the natural coordinate of point M are available.

$$M(\bar{x}, \bar{y}, \bar{z}) \rightarrow M(\xi, \eta, \zeta)$$

The pressure at point M is

$$P_M = \sum_{i=1}^{20} N_i P_i \quad (3-19)$$

and the values of $(\partial P/\partial x)_M$, $(\partial P/\partial y)_M$, $(\partial P/\partial z)_M$

and $(\partial P/\partial n)_M$ can be calculated.

After determining the appropriate values of A and B from $(\partial P/\partial n)_M$, the velocities at point M on the cutting plane are

$$V_{n,M} = A(\partial P/\partial n)_M^B \quad (3-20)$$

$$V_{x,M} = (V_{n,M})(\partial P/\partial x)_M / (\partial P/\partial n)_M$$

$$V_{y,M} = (V_{n,M})(\partial P/\partial y)_M / (\partial P/\partial n)_M$$

$$V_{z,M} = (V_{n,M})(\partial P/\partial z)_M/(\partial P/\partial n)_M$$

At this point, the nodal pressure and velocity values on the cutting plane were calculated.

CHAPTER IV
COMPUTER PROGRAMMING

4.1 THE SEQUENCE OF COMPUTER PROGRAMS

Three computer programs were written to solve the flow field problem under study. The first computer program calculated the nodal pressure values in three-dimensions in the aeration cylindrical grain storage. The results were stored and used as the data input for the second computer program which generated the element two-dimensional data and calculated the nodal pressure and velocity values on the cutting surface. This computer program was also used to draw the pressure and velocity distribution contour lines for the cutting plane. The third computer program was written in order to display the pressure and velocity distribution in three-dimensions.

A more detailed discussion of these three computer programs is presented.

4.1-1 The Finite Element Computer Program

The three-dimensional nodal pressure values were generated by the first computer program with the following steps: 1) Read the number of elements, the number of equations, the bandwidth, and generate the element data. 2) Read the grain coefficients A and B (for shelled corn) along with the range of pressure gradients. 3) Input the

specified pressure values on the boundary nodes.

4) Calculate pressure gradients and select the appropriate values for the grain coefficients A and B. 5) Calculate the element stiffness matrix for each element and assemble these into a system of equations. 6) Modify the system of equations to incorporate specified nodal pressure values and then solve the equations for each nodal pressure value. 7) Compare the nodal pressures with the nodal pressures from the previous step. If the maximum difference between the pressures of the two consecutive steps at any one node is less than 0.25 pascals (0.001 in. of water), write the nodal pressure values, store the pressure values as the input data for the second computer program and end the first computer program. Otherwise, replace the old pressure values by the new calculated values and then repeat step four through seven, until the maximum difference between any consecutive pair of pressure values is less than 0.25 pascals (0.001 in. of water).

It was convenient and desirable to calculate only the three-dimensional nodal pressure values in the first computer program; the nodal velocity values are then obtained from equation (3-12) after the nodal pressure values are established (Section 3.3). The nodal velocity values were calculated in the second computer program on the cutting planes.

4.1-2 Computer Program for the Two-Dimensional Cutting Plane

The second computer program was generated with the following steps: 1) Read the number of regions, the number of boundary nodes, the coordinates, and the number of rows and columns of nodes in each region on the cutting plane. 2) Input the data for plotting options and generate the element data. 3) Read the element data along with the nodal pressure values obtained from the first computer program. 4) Generate the natural coordinates for each node on the cutting plane corresponding to the cubic element it is in. 5) Calculate the pressure and velocity at each node on the cutting plane. 6) Input specified pressure and velocity values which expected to be plotted. 7) Compare the nodal pressure and velocity values on the cutting plane and the specified values from step six, then generate the coordinates of the contour points of isopressure lines and equal velocity lines. 8) Plot isopressure lines and velocity distribution on the cutting plane and end the program.

Note that most of the available airflow data for grain have been reported in English units. The velocity is usually in feet per minute (ft/min.), while the pressure is in inches of water (in. of water). In the SI unit system, meter per minute is used for velocity while the pressure is in pascals. It was convenient to calculate the pressures and velocities in English units first and then convert them to SI units in the final step. The appropriate conversion

factors are

1.0 in. of water = 250 pascals

1.0 ft/min. = 0.3048 m/min.

The Colcomp Plotter System at the Computer Center (Michigan State University) was used for plotting.

4.1-3 Three-Dimensional Display Computer Program

The main objective of this computer program was to display the results from the second computer program in a three-dimensional configuration. This third computer program was a modification of SURFACE II GRAPHIC SYSTEM (Computer Center, Michigan State University). SURFACE II is a computer software system for creation of displays of spatial distribution data points. The spatial coordinates of these points constitute two variables, x and y, and the height of each point constitutes a third variable, z. The basis for operation in SURFACE II is a grid of values representing the surface to be displayed.

SURFACE II produced perspective block diagrams, sometimes called transect or fishnet plots. These can be envisioned as a deformed rectangular grid or mesh, where the spacing between lines of the mesh correspond to equal increments of the variables x and y. However, the mesh push upward until it conforms to values of the third variable, z. The resulting form allows the display to be modified and viewed from any elevation, at any angle, and from any distance. Such a graph gives a visual representation of surface topography. The steps of the third computer program could be described as follows: 1) Select the appropriate

pressure and velocity values to be displayed and run the second computer program. 2) Collect the spatial coordinate data points (x,y,z) from the numerical results of the second computer program and use them as the data input for the third computer program. 3) Attach and modify SURFACE II to generate a grid matrix from x,y,z data points. 4) Store the contents of the grid matrix on a local code file. 5) Restore a matrix stored in binary format into memory. 6) Create a perspective transect diagram of the grid matrix at the selected level, distance and angle to be viewed.

Note that in step four the contents of the grid matrix were saved in order to help reduce the execution costs of SURFACE II which used the same data set. In this case the grid matrix was saved on a local code file. In subsequent runs, this file was reused eliminating the need to regenerate the grid matrix. Graphic output from SURFACE II was routed directly to the Calcomp Plotter using the DEVICE command. This command might be used to retain the plot on local file PLOTFIL. PLOTFIL might then be cataloged and viewed at a Tektronix terminal.

4.1-4 Developing Confidence in the Calculated Values

Confidence in the calculated values of this study were based on the governing differential equation and the correctiveness of the finite element computer program.

1) The two-dimensional differential equation for airflow through grain mass has been solved using the finite difference and the finite element method by Marchant (1976a, 1976b). The calculated results agree well with

experimentally measured values.

2) The finite element computer program was checked using the following tests:

- 2-1) The sum of each row and column of the element stiffness matrix was checked to make sure it summed to one.
- 2-2) The subroutine containing the shape functions was checked to see if they satisfied their basic properties.
- 2-3) The sum of the derivatives of the shape functions with respect to x, y and z were checked to make sure they were zero at any point within an element.

4.2 TYPES OF THE CYLINDRICAL GRAIN STORAGE UNDER STUDY

There were four types of aeration systems for cylindrical grain storages studied. The four systems are differentiated by the size and shape of the perforated floor. Specific details of those sizes and shapes used are given in Table 4-1 and shown in Figures 4-1 through 4-4.

Table 4-1. Size and perforated floor patterns of the cylindrical grain storages under study.

Figure Number	Perforated Floor Type	Diameter (D) m	Perforated Floor Size m x m	Height (H) m
4-1	Total	7.32	7.32 (dia)	6.40
4-2	Straight	7.32	0.92 x 6.10	6.40
4-3	Square	18.30	9.15 x 9.15	12.80
4-4	Y	10.97	0.92 x 7.62	9.144

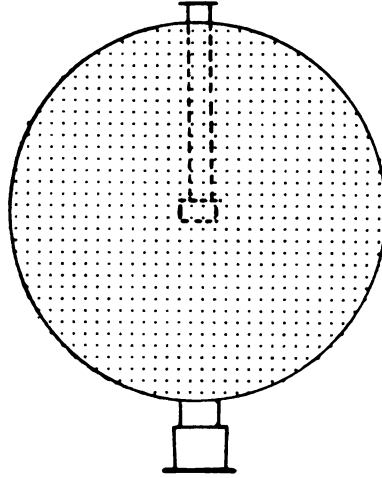


Figure 4-1. A total perforated floor system (Type 1).
(Brook, 1979).

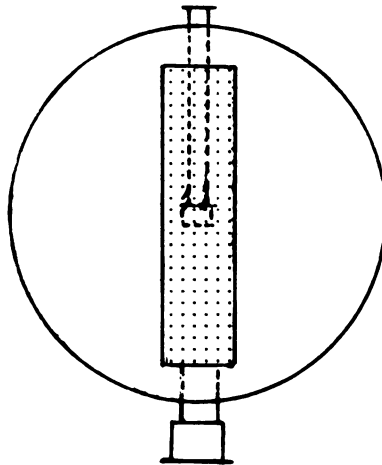


Figure 4-2. A straight duct perforated floor
system (Type 2).
(Noyes, 1967).

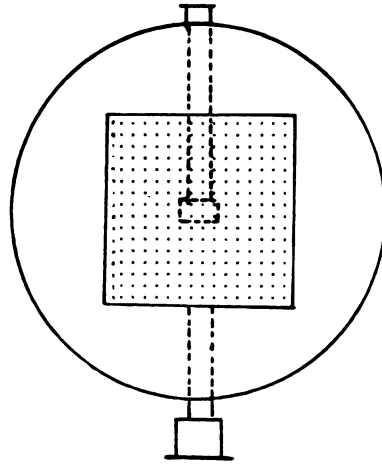


Figure 4-3. A square duct perforated floor system
(Type 3).
(Brook, 1979).

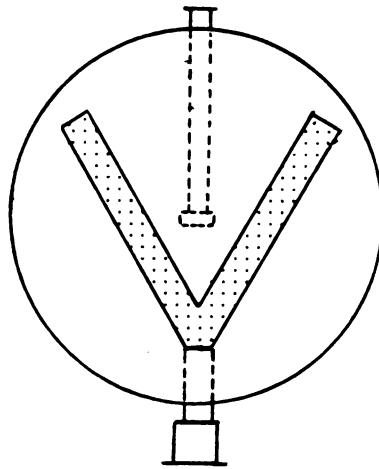


Figure 4-4. A Y-duct perforated floor system
(Type 4).
(Noyes, 1967).

The perforated floor section is the place where the air is distributed into the grain storage. Flush-floor ducts (ducts are set below floor level) are commonly used as the distribution systems for aeration.

4.3 GEOMETRY

Because of symmetry, the analysis of each cylindrical grain system can be done using only a half of bin. Figure 4-5 shows the example of an analyzed cross-section related to the configuration of the perforated floor and the dimension of each type of the grain storage. Figure 4-6 also shows the division into elements. Due to the limitation of the computer central memory and for reasonable computing time, five layers of elements were used with twelve elements per layer. The 60 elements had 406 nodes and bandwidth of 88. The height of the elements at each layer depended on their distance from the perforated floor and the height of the grain storage. The shortest elements in height (about 5% of the height of grain storage) were located in the layer contacting the perforated floor.

4.4 INPUT TO THE PROGRAM

The cylindrical grain storages mentioned in 4.2 were selected studied because they are the most popular types of commercial aeration grain storages. The sizes of these storages vary according to the customer's needs. The half circular cross-section of the grain storage was presented in Figure 4-6. The size of elements in each layer depends on the size and perforated floor shape of the grain storage.

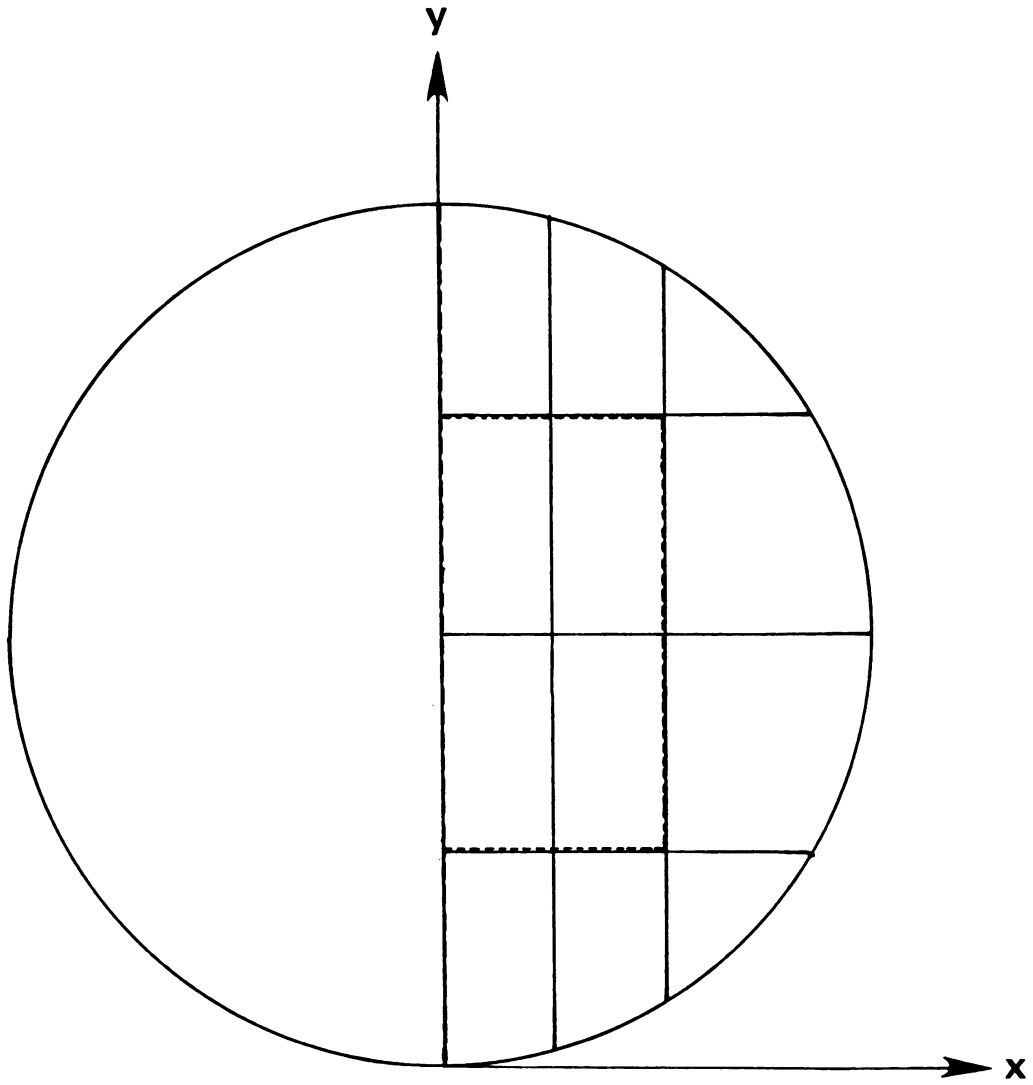


Figure 4-5. Cross-section of the elements in X-Y plane.

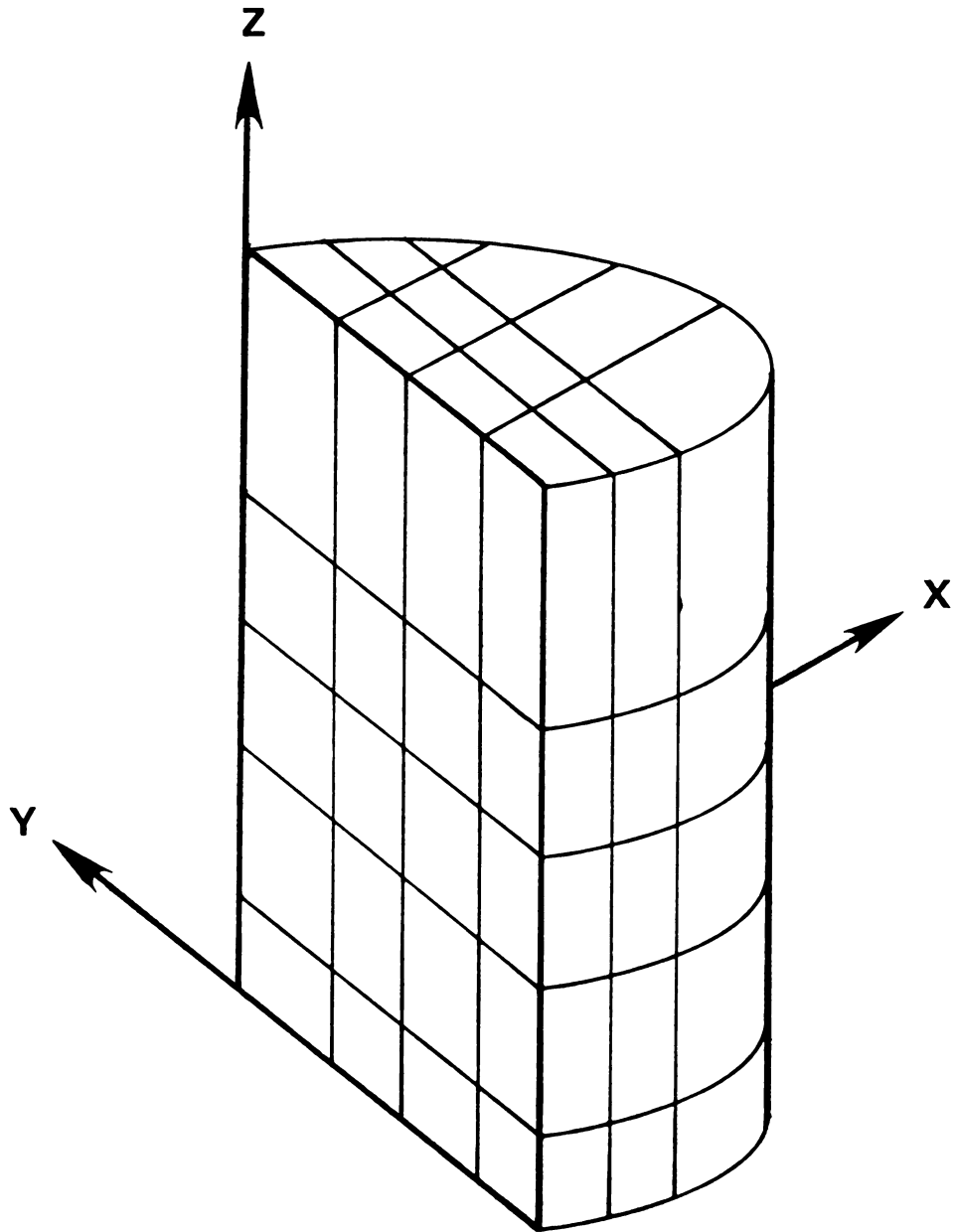


Figure 4-6. Division into the elements of a half cylindrical grain storage.

4.4-1 Boundary Conditions

In order to solve the nonlinear airflow equation (3-2), using an iterative procedure, the coefficient C in (3-3) was set to be one ($C=1$) on the first iteration. A subroutine was written to evaluate the element stiffness matrices using (3-5) and (3-8). The element stiffness matrices were assembled into a banded system of equations. The zero coefficients outside the bandwidth were not stored. Once the system of equation was assembled, the known boundary conditions (or specified pressure values) were incorporated and the system of equations was modified accordingly. The known pressure values at the perforated floor and at the free surface (the top of the grain surface) were considered to be specified nodal pressure values or boundary conditions. "The no flow or impermeable boundary condition, $\partial P/\partial n = 0$, is automatically enforced on the boundary when the pressure values were not specified." (Segerlind, 1982)

From the assembly of the system of equations along with the specified nodal pressure values, the system of equations was solved using the Gaussian elimination method. On the second and the following iterations, the nodal pressure values existed and the coefficient C in (3-3) was calculated. The iterative process was repeated until all nodal pressure values on the successive iteration was less than 0.25 pascals (0.001 in. of water). In this study, the pressure at the perforated floor was assumed to be 500 pascals (2.0 in. of water) for each type of grain storage.

storage.

4.4-2 Grain Coefficients

Shelled corn was selected as the grain media in this study. Recalling (2-1),

$$V_n = A \left(\frac{\partial P}{\partial n} \right)^B \quad (4-1)$$

Shedd stated that A and B were not constant over a wide variation in pressure gradients. Shedd's equation was a straight line on a log-log plot but most of the experimental data was not a straight line. Brooker (1969) introduced that idea of modeling the log-log plots of velocity versus pressure gradient by a series of straight line segments using (4-1) for each straight line. The several values of grain coefficient A and B for shelled corn were obtained from his work. These values were reproduced (and corrected) by Segerlind (1982) as given in Table 4-2. The values of A and B given in Table 4-2 were used in this analysis.

Table 4-2. Values of pressure gradient and grain coefficients A and B for Shelled Corn (Brooker, 1969 and Segerlind, 1982).

Range for the pressure gradient (in. of H ₂ O/ft)	Grain Coefficients	
	A	B
0.000 - 0.010	167.0	0.950
0.010 - 0.025	113.0	0.867
0.025 - 0.070	78.0	0.768
0.070 - 0.200	65.8	0.702
0.200 and above	59.0	0.628



CHAPTER V
THE RESULTS FOR CYLINDRICAL GRAIN STORAGES

5.1 THE CUTTING PLANE

As mentioned in Section 2.3, a plane was projected to cut the half section of the grain storage at a selected location in order to display the pressure and velocity distributions. The second computer program, (Section 4.1-2), was written in general form with many options to allow cuts perpendicular or parallel to the perforated floor. In this way, the pressure and velocity distributions within the grain storage at any locations could be displayed thereby saving a considerable amount of computing time.

There were many interesting locations to be studied for each type of the grain storage. It became convenient to use a name such as "Type I-J" to describe the type and location of the cutting plane.

The letter "I" represented the type of the grain storage:

I = 1 = Total perforated floor system.

I = 2 = Straight duct perforated floor system.

I = 3 = Square duct perforated floor system.

I = 4 = Y-duct perforated floor system.

The numerical value of "J" indicated the location of the cutting plane.

A plane cutting through the center of the grain storage perpendicular to X-Y plane and Y-Z plane as shown in Figure 5-1a through 5-1cC was denoted by J=1.

The case J equal to 1P is the special case of the Y-duct perforated floor system, where the plane cuts perpendicular to the sides of the perforated floor and perpendicular to the X-Y plane. Figure 5-1d shows this type of cutting plane.

Values of J equal to two and three, denote a plane which cuts across the half section of the grain storage parallel to the perforated floor at a height of 5% (J=2) and 50% (J=3) of the total height of the grain storage, respectively. These types of cutting planes are shown in Figure 5-2a and 5-2b.

The total perforated floor system is denoted by J=1F when the top of the grain storage is not flat as shown in Figure 5-3a; the cutting plane is the same as J=1 but the plane also passes the conical shape at the top of the grain storage as illustrated in Figure 5-3b.

A J equal to 3F represents a plane which cuts across the half of the grain storage type 1F in the same manner as J equal to three. Figure 5-3c shows this type of cutting plane.

The notation for the cutting planes "Type I-J" are used for convenience in referencing the type of cutting plane and the type of the grain storage.

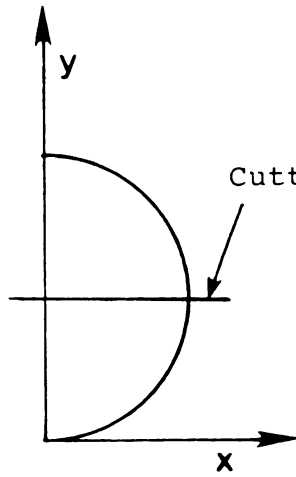


Figure 5-1a. Cutting plane:
Type 1-1.

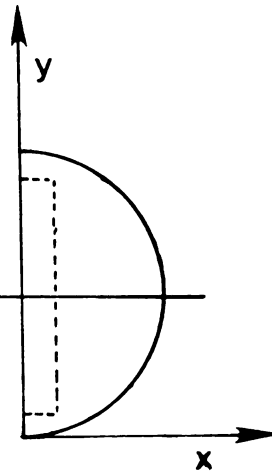


Figure 5-1b. Cutting plane:
Type 2-1.

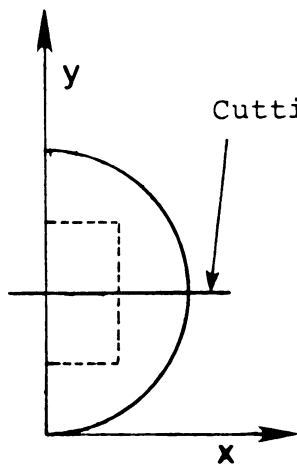


Figure 5-1c. Cutting plane:
Type 3-1.

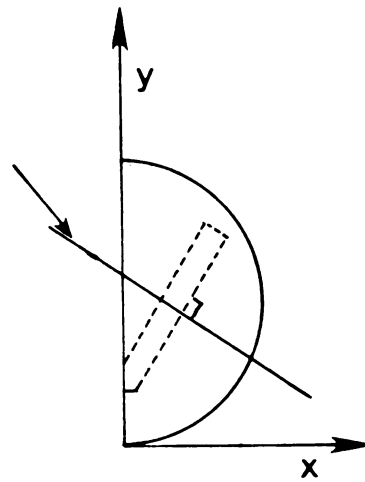


Figure 5-1d. Cutting plane:
Type 4-1P.

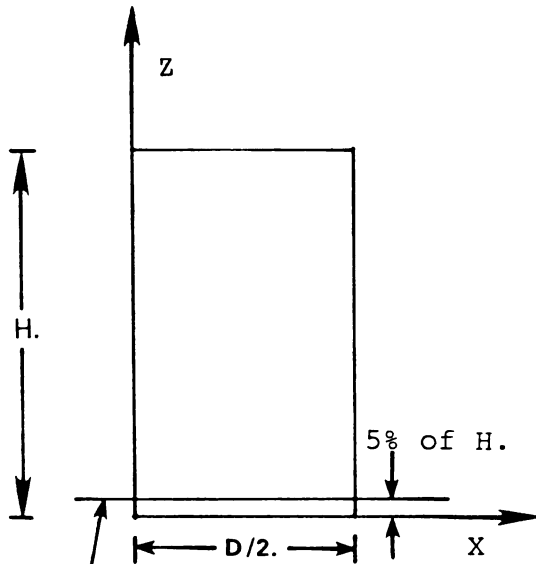


Figure 5-2a. Cutting plane:
 Type 1-2,
 Type 2-2,
 Type 3-2,
 and Type 4-2.

Cutting Plane

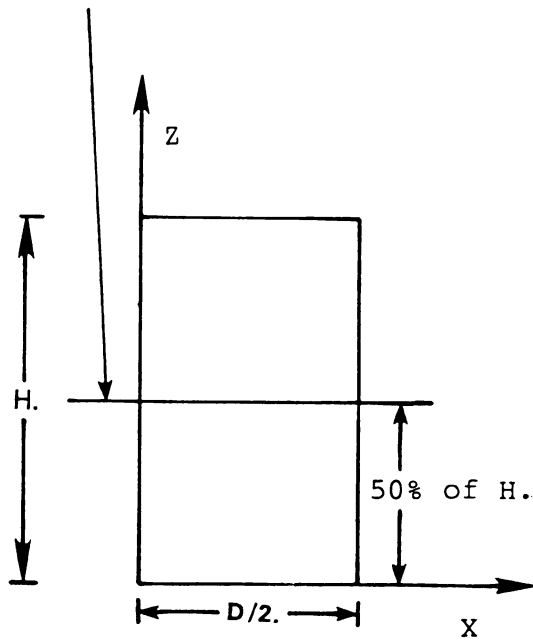


Figure 5-2b. Cutting plane:
 Type 1-3,
 Type 2-3,
 Type 3-3,
 and Type 4-3.

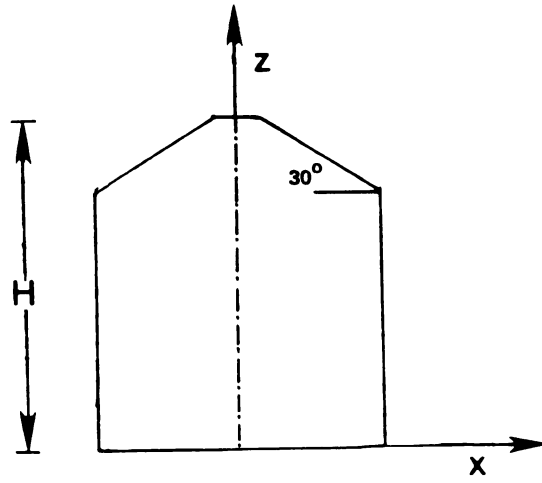


Figure 5-3a. Full top grain configuration (Type 1F) ($H=8.382$ m.).

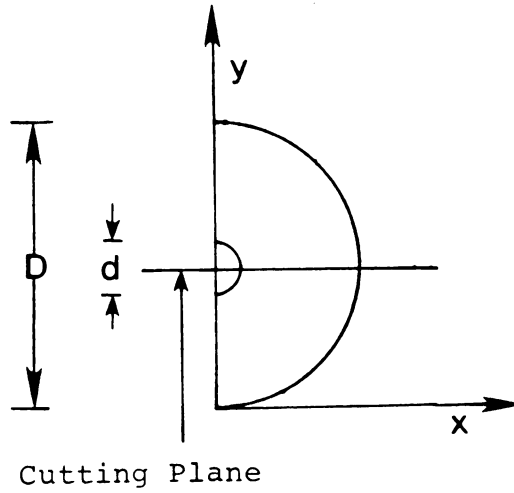


Figure 5-3b. Cutting plane: Type 1F-1F ($D=7.32$ m.) ($d=0.457$ m.).

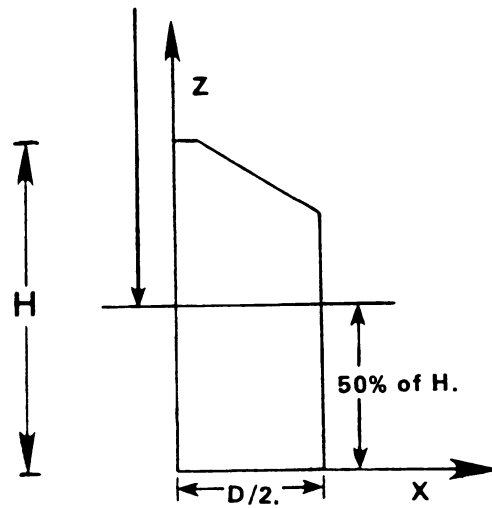


Figure 5-3c. Cutting plane: Type 1F-3F.

5.2 COMMENTS

There are many pressure and velocity distributions on the cutting planes that can be displayed for each type of cylindrical grain storage under study. Pressure and velocity distributions for the various bins are discussed in the following sections. Most of the displays are two-dimensional although several three-dimensional pressure and velocity displays are presented in Section 5.7.

It is and convenient to express the pressure distribution in terms of a percent of the perforated floor pressure. In this way the comparison between bins can be done effectively. It is also reasonable to use the resultant (or apparent) velocity (V_n) in meter per minute to represent the velocity distribution. The computer program results show that the velocity in the z direction plays a major role in the velocity distribution within cylindrical grain storages. The velocity components in x- and y- directions are very small when compared to the magnitude of velocity component in the z-direction.

5.3 PRESSURE AND VELOCITY DISTRIBUTIONS OF THE TOTAL PERFORATED FLOOR SYSTEM

The grid-elements on the cutting planes of the total perforated floor system are shown in Figures 5-4a and 5-4b. The pressure distribution patterns in the bin with a total perforated floor are presented in Figures 5-4c through 5-4e. The pressure increases uniformly with respect to the depth of grain. There is no pressure gradient in the x- and y- directions. The total pressure gradient depends on the

height in the z direction.

The velocity distribution of this type is also uniform (about 3.8 m/min.) at any location within the bin because of zero velocity in the x and y directions and constant total pressure gradient. Figures 5-4f and 5-4g show the velocity distributions for this type of perforated floor system.

Figures 5-5a through 5-5e show the grid-element, the pressure and velocity distributions for the special case of the total perforated floor system where the top of the grain storage is not flat. These figures show the effect of the top configuration on the pressure and velocity distributions, neither of which are uniform.

5.4 PRESSURE AND VELOCITY DISTRIBUTION OF THE STRAIGHT DUCT PERFORATED FLOOR SYSTEM

The grid elements on the cutting planes of the straight duct perforated floor system are shown in Figure 5-6a and 5-6b. The pressure distribution of this perforated floor system at different locations of the cutting plane are presented in Figures 5-6c through 5-6e. The pressure is very high in the area near the perforated floor. The pressure decreases below 40% of the perforated floor pressure at a depth of about 30% of the total height of the grain storage. The pressure distribution on any level above 50% of the height is uniform and less than 30% of the total perforated floor pressure. The resultant velocity is quite high in the area near the perforated floor. Figures 5-6f through 5-6h show the velocity distribution patterns of this straight duct

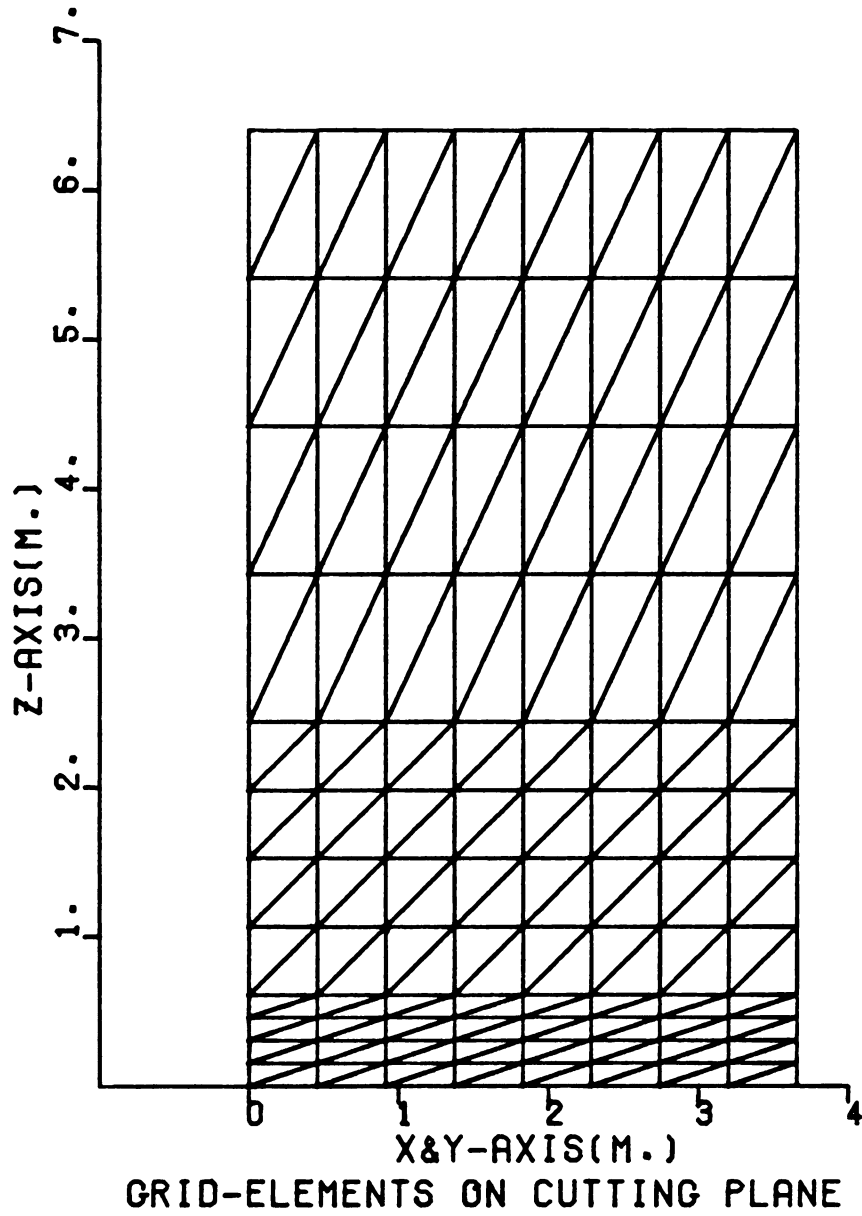
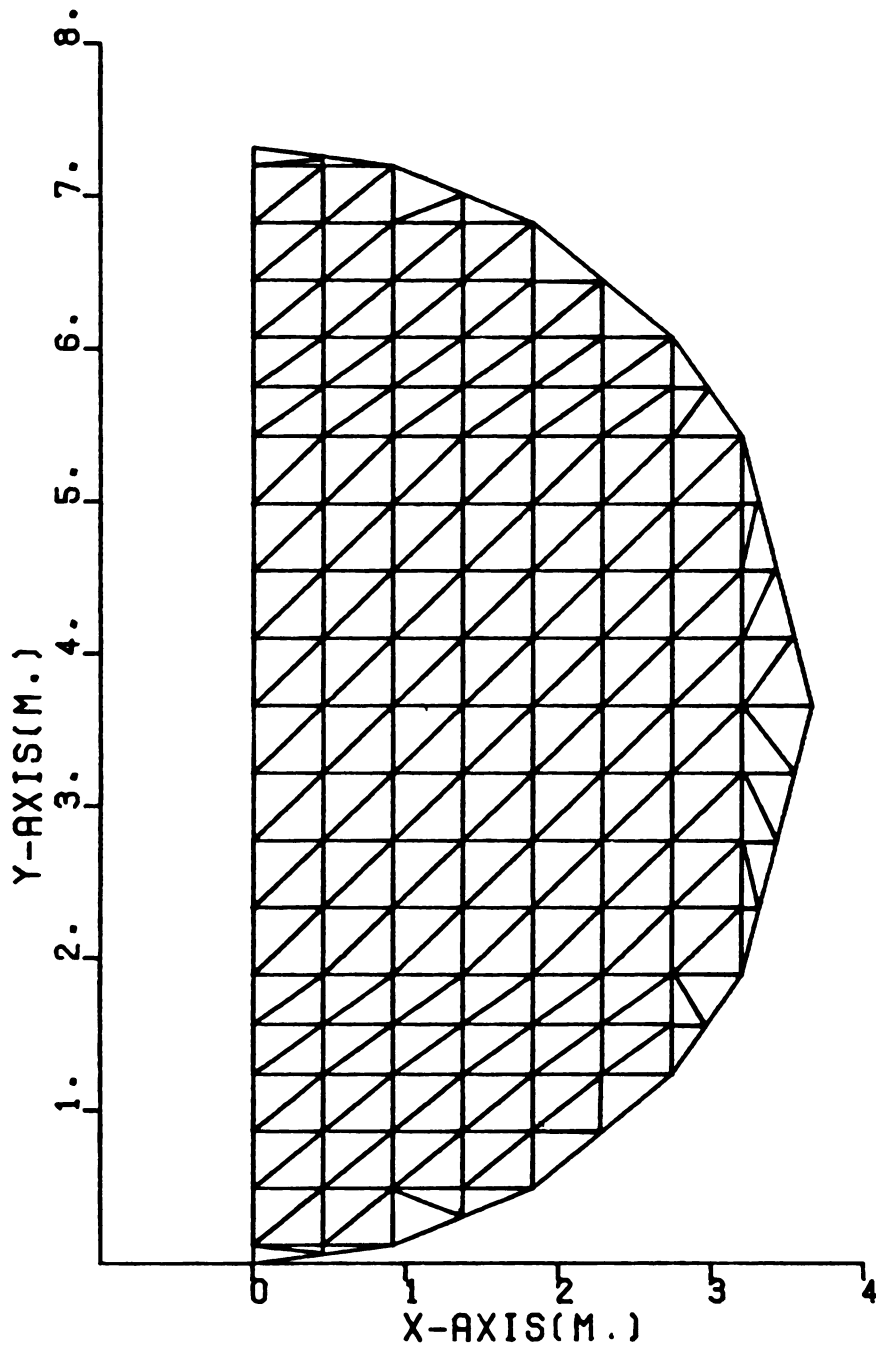


Figure 5-4a. Locations of the grid-elements on the cutting plane (Type 1-1).



GRID-ELEMENTS ON CUTTING PLANE

Figure 5-4b. Locations of the grid-elements on the cutting plane (Type 1-2, 1-3, and 1F-3F).

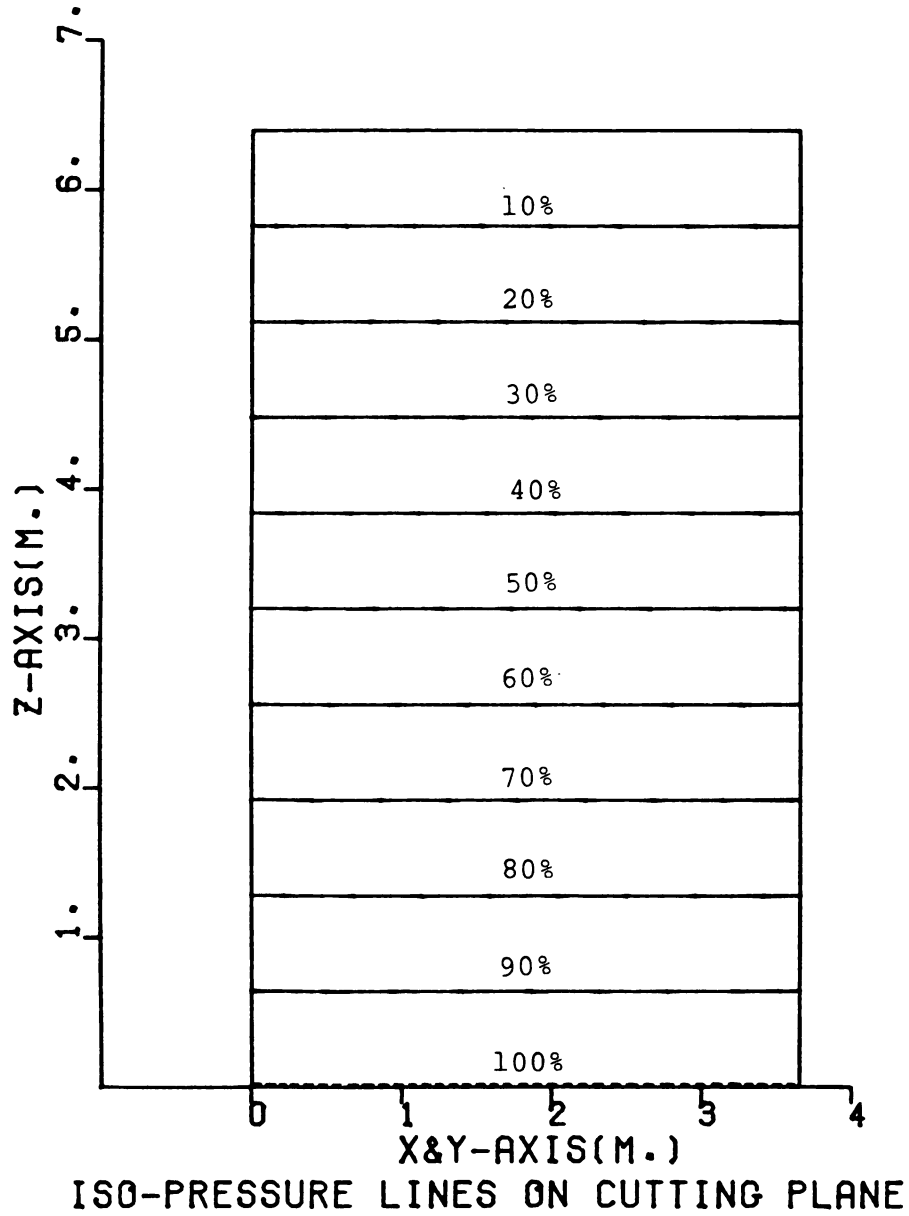
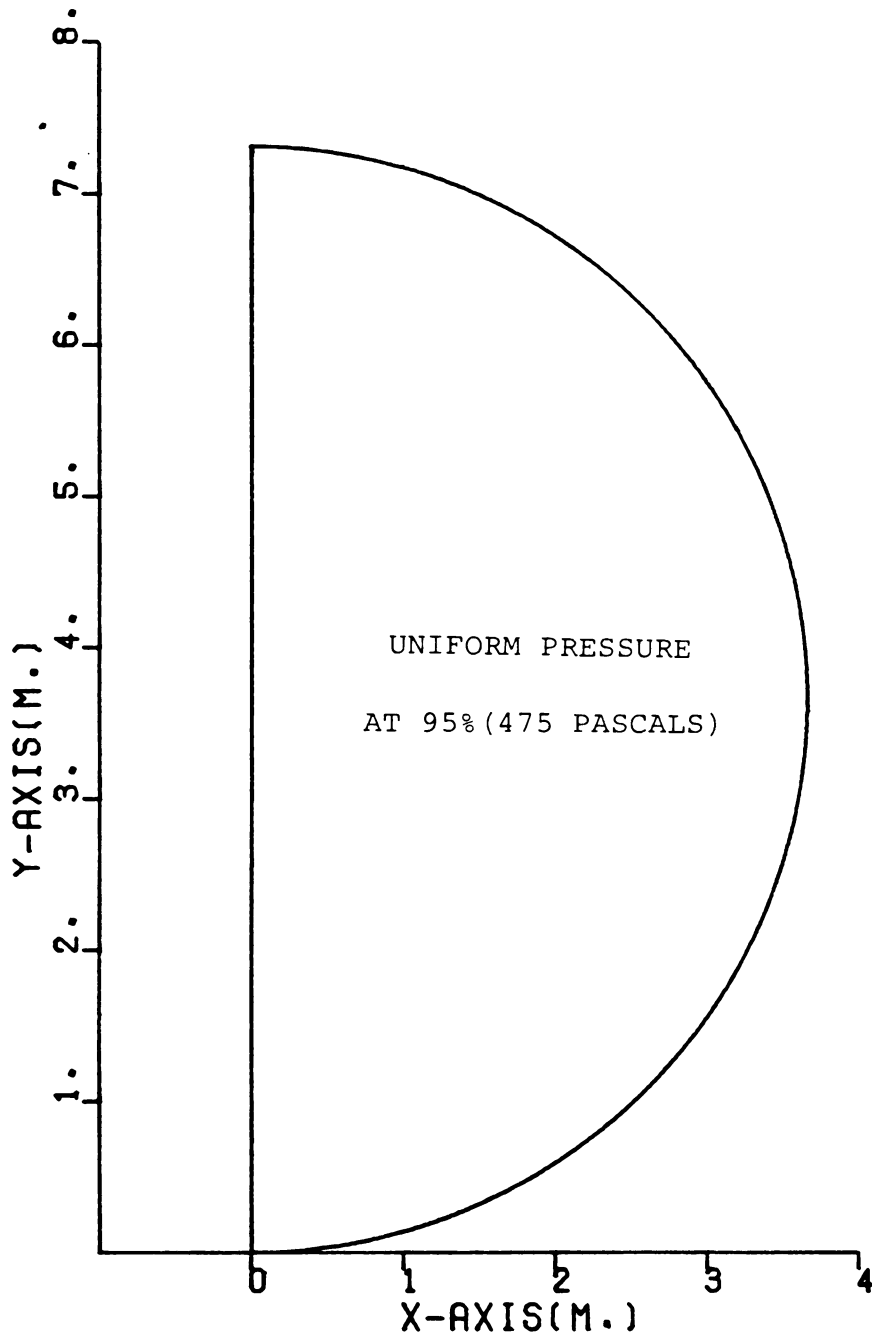
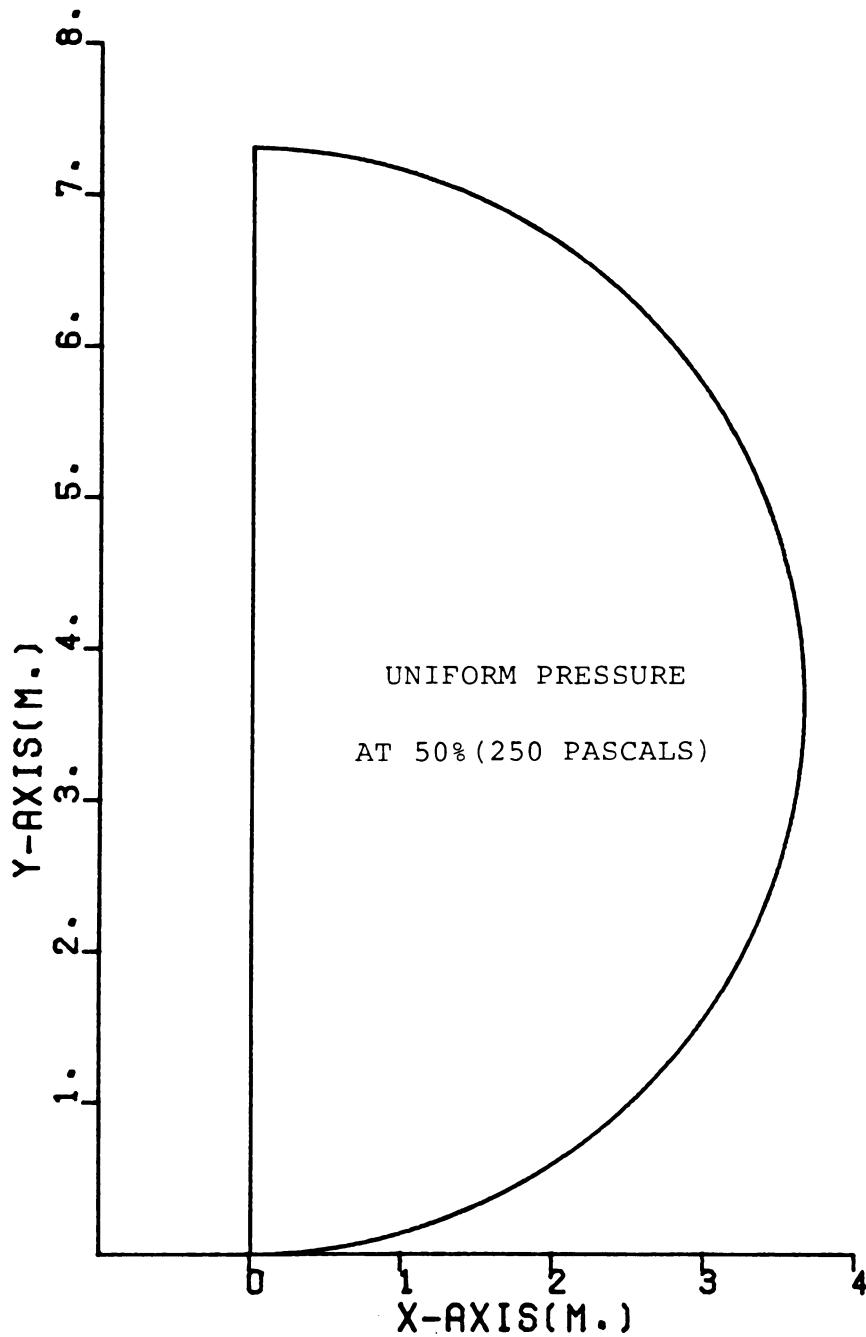


Figure 5-4c. Pressure distribution (Type 1-1) in percent of perforated floor pressure (perforated floor pressure = 500 pascals).



ISO-PRESSURE LINES ON CUTTING PLANE

Figure 5-4d. Pressure distribution (Type 1-2) in percent of perforated floor pressure (perforated floor pressure = 500 pascals).



ISO-PRESSURE LINES ON CUTTING PLANE

Figure 5-4e. Pressure distribution (Type 1-3) in percent of perforated floor pressure (perforated floor pressure = 500 pascals).

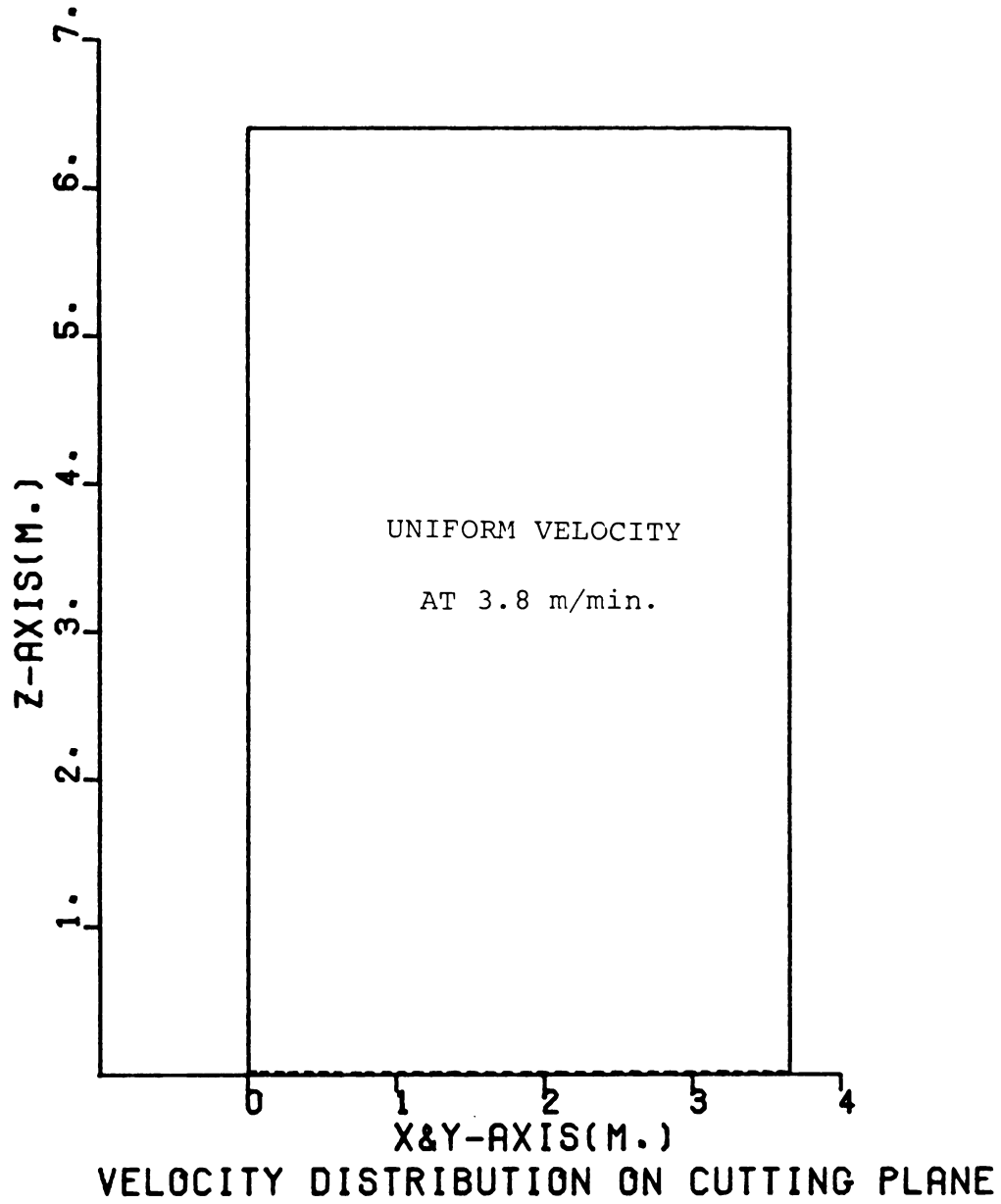
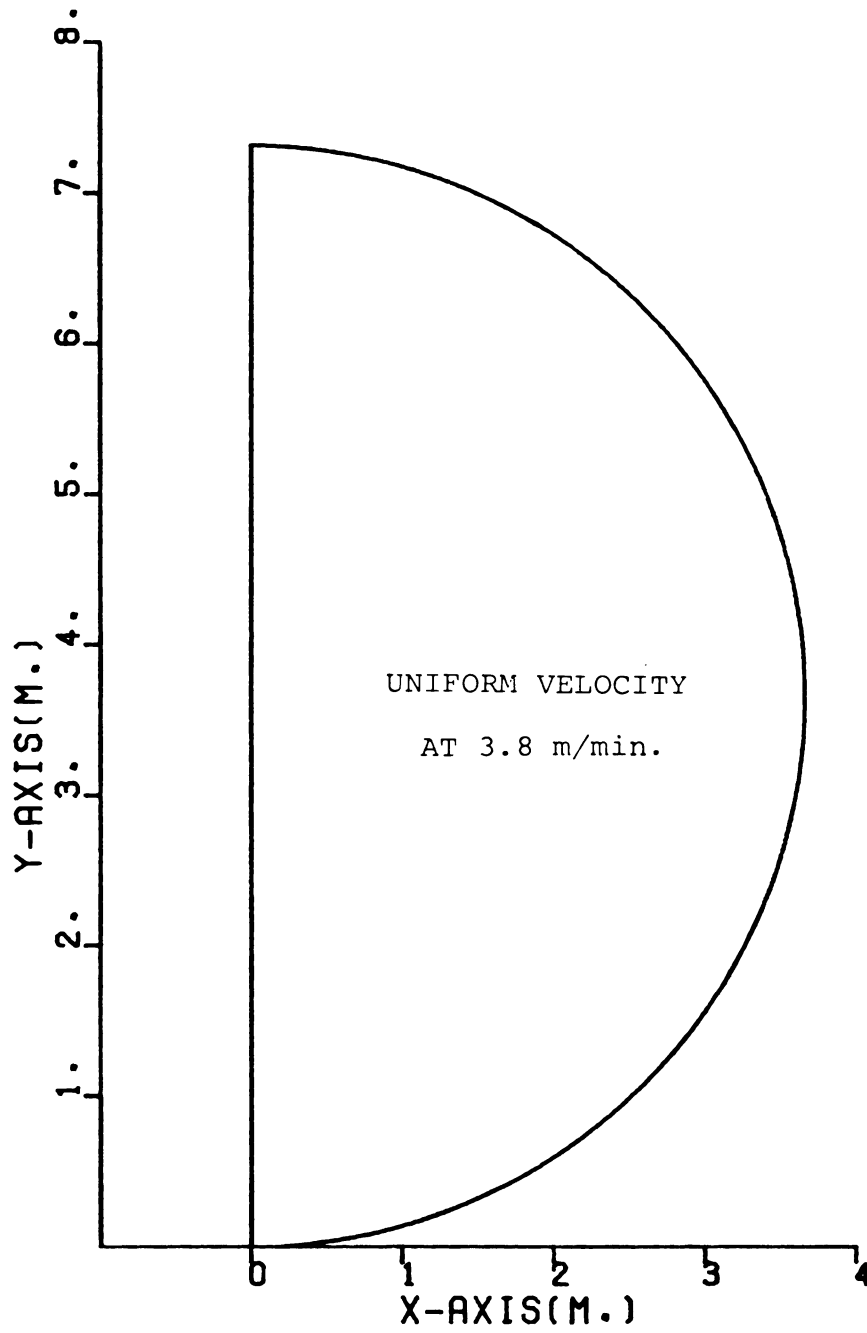


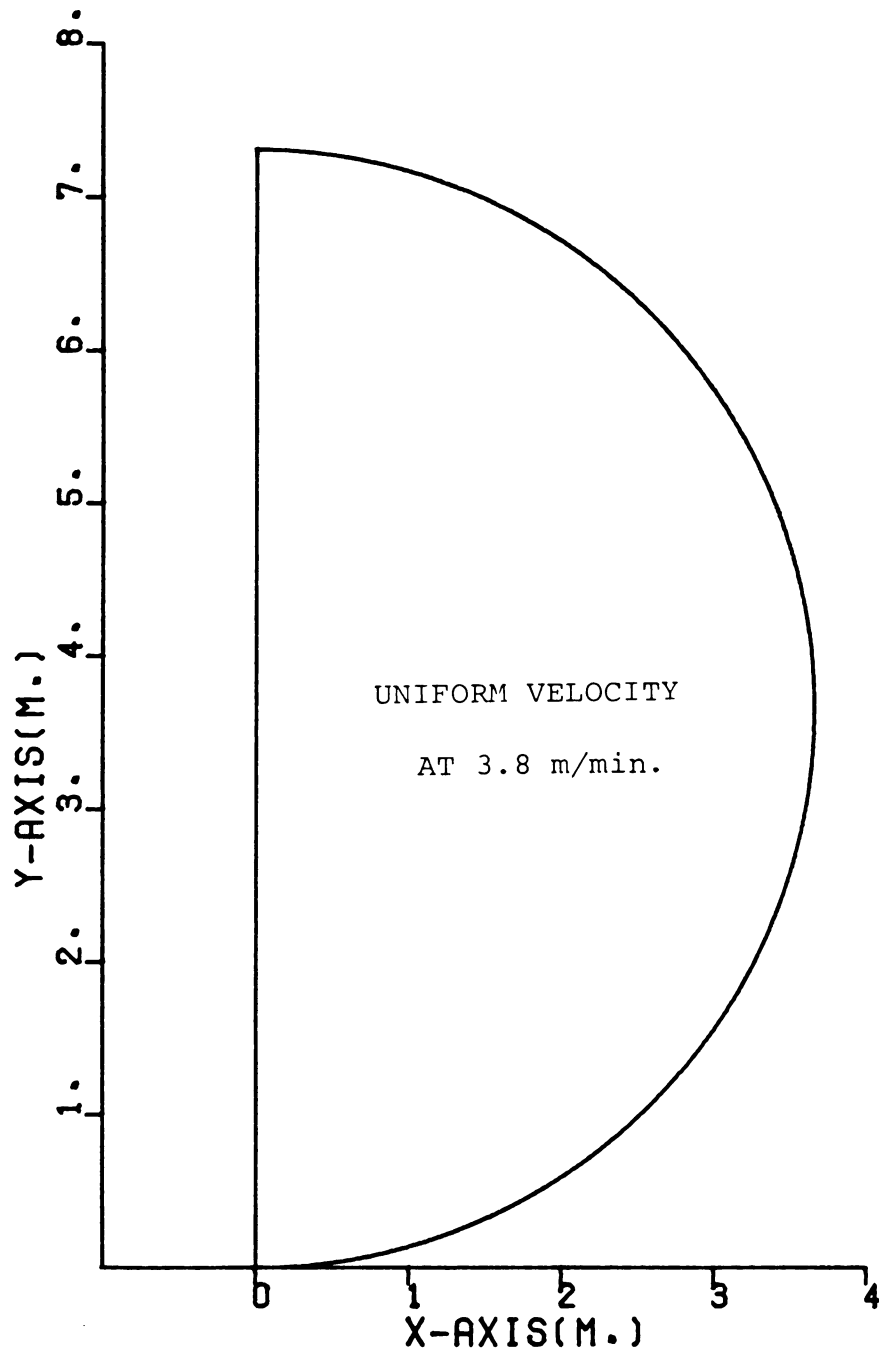
Figure 5-4f. Velocity distribution (Type 1-1) in m/min.





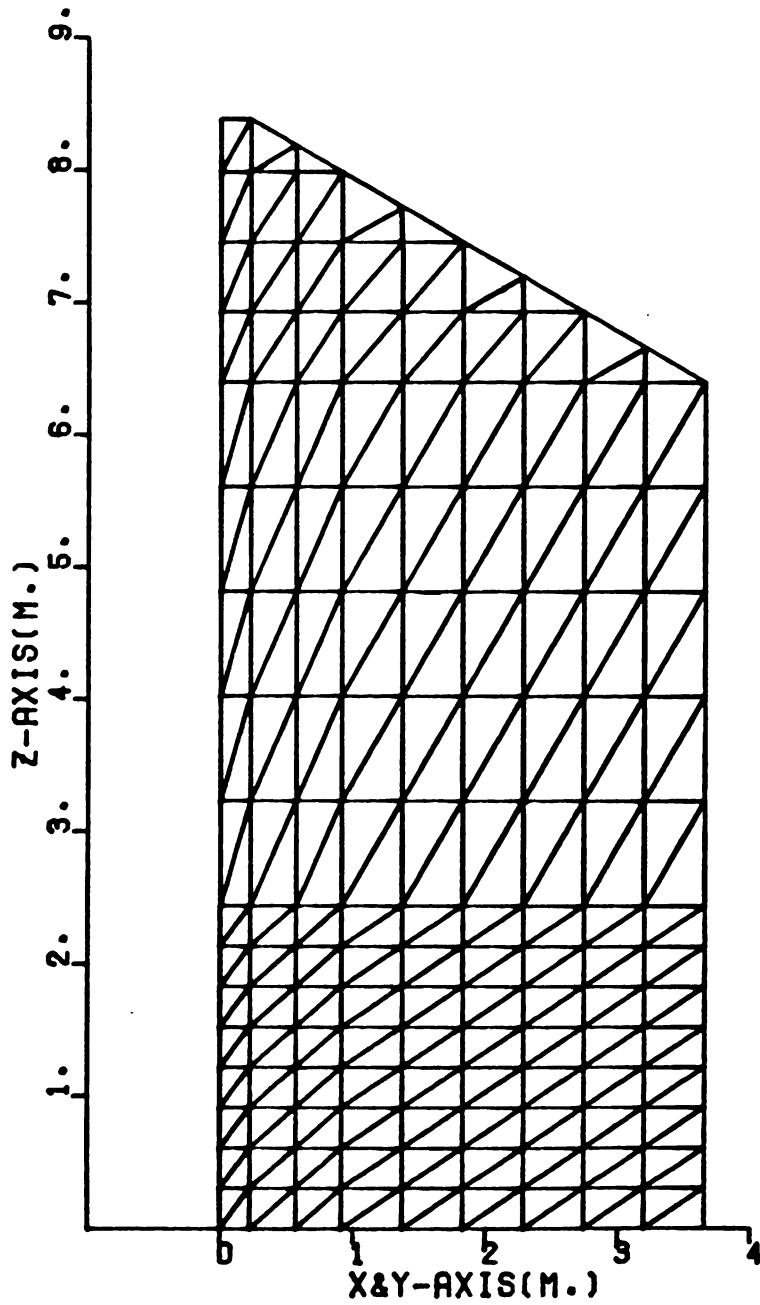
VELOCITY DISTRIBUTION ON CUTTING PLANE

Figure 5-4g. Velocity distribution (Type 1-2) in m/min.



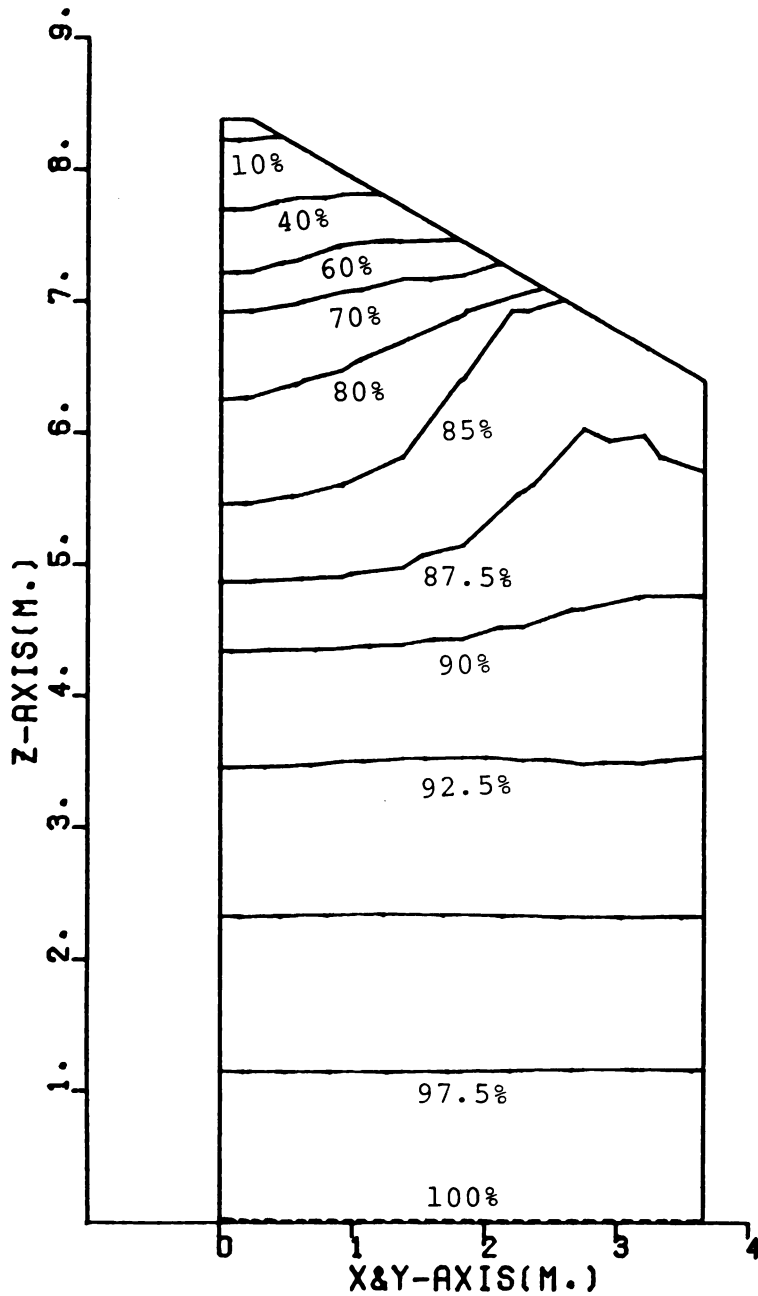
VELOCITY DISTRIBUTION ON CUTTING PLANE

Figure 5-4h. Velocity distribution (Type 1-3) in m/min.



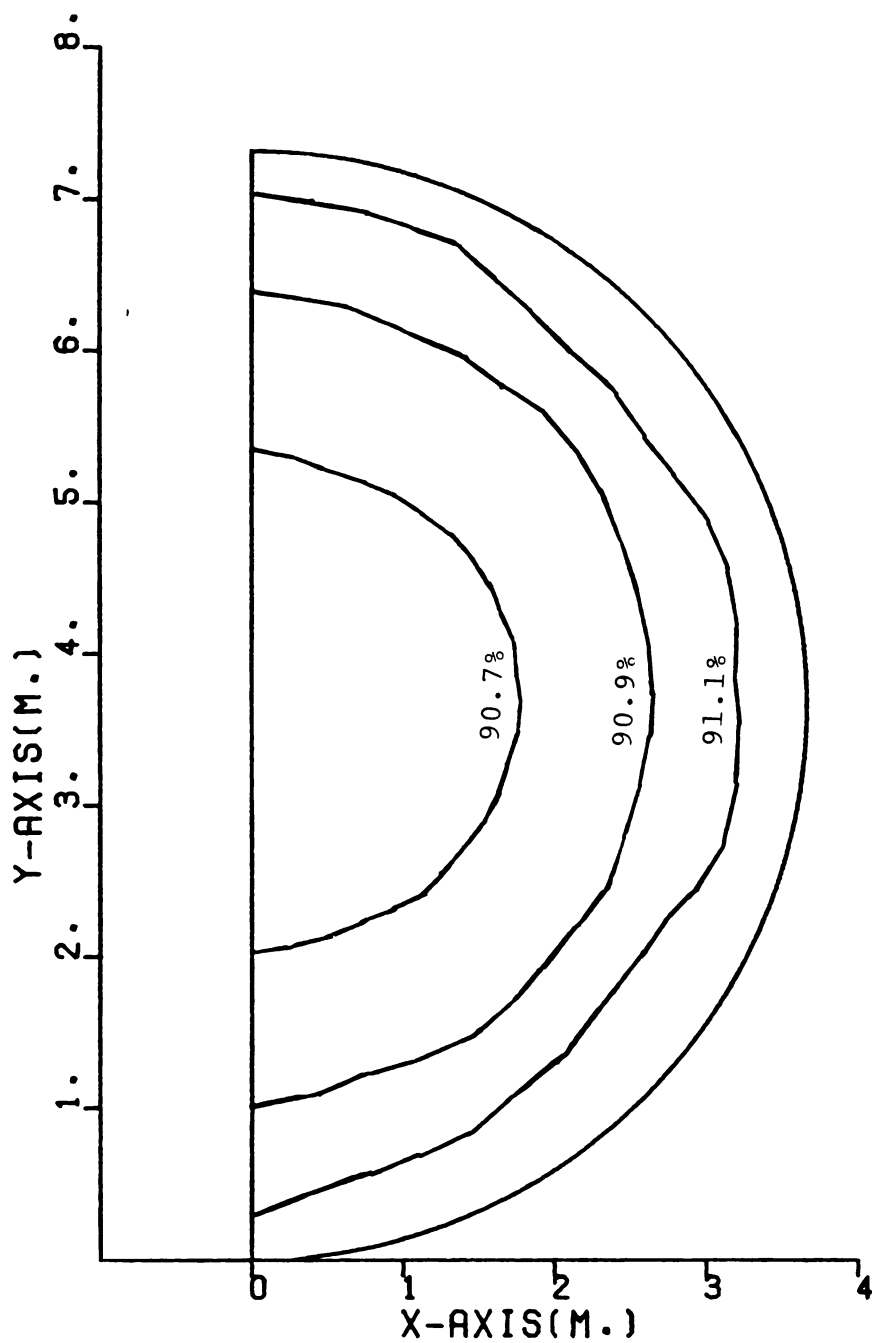
GRID-ELEMENTS ON CUTTING PLANE

Figure 5-5a. Locations of the grid-elements on the cutting plane (Type 1F-1F).



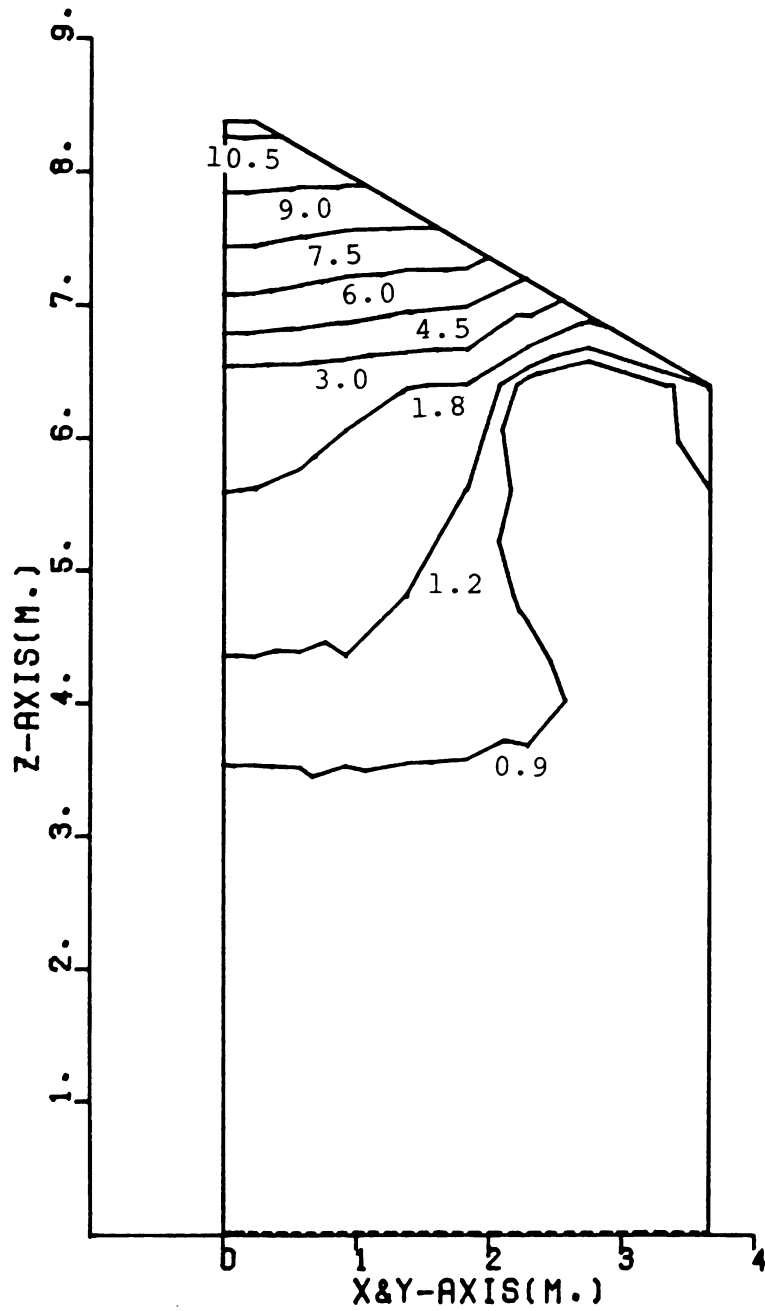
ISO-PRESSURE LINES ON CUTTING PLANE

Figure 5-5b. Pressure distribution (Type 1F-1F) in percent of perforated floor pressure (perforated floor pressure = 500 pascals).



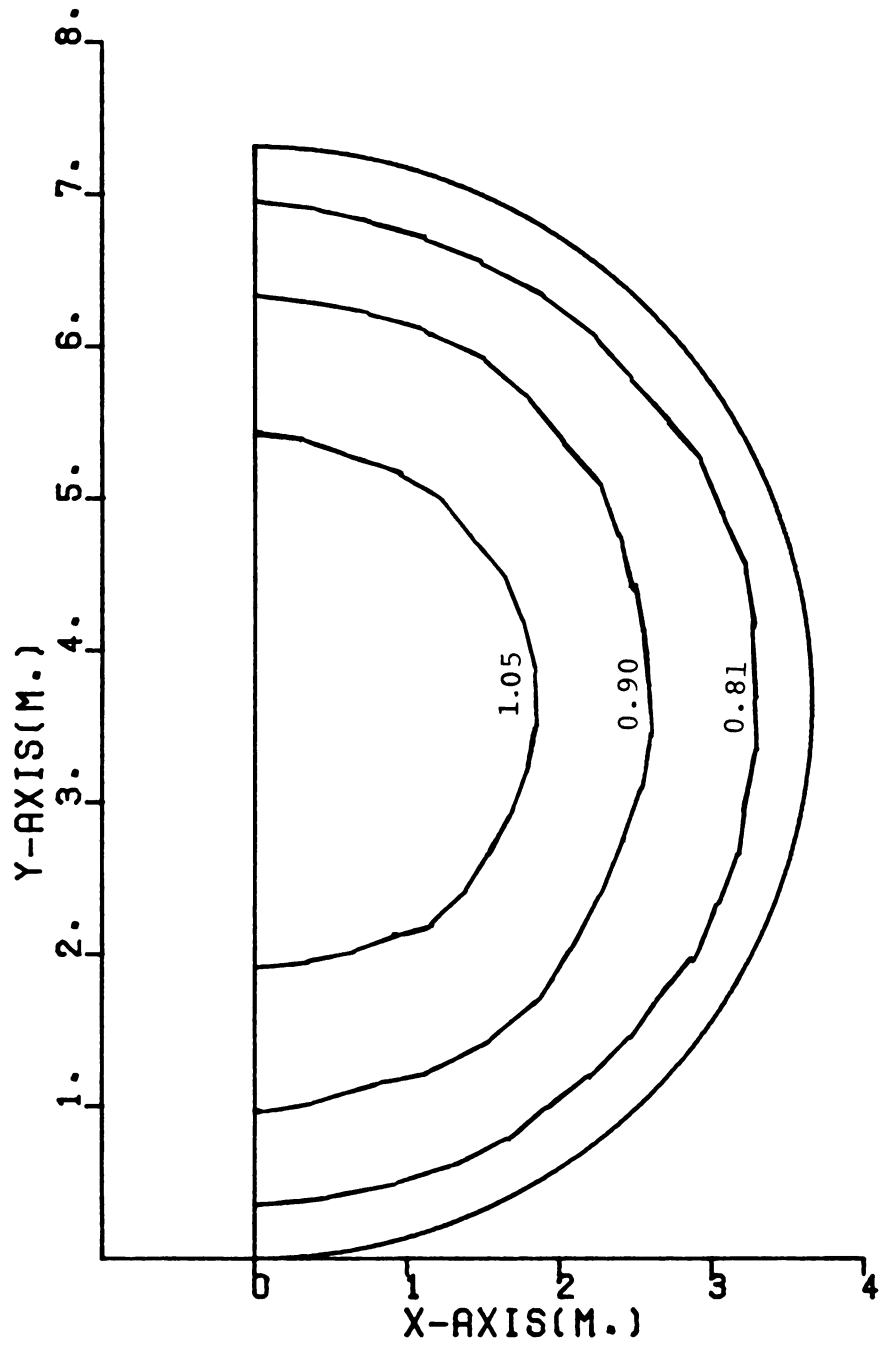
ISO-PRESSURE LINES ON CUTTING PLANE

Figure 5-5c. Pressure distribution (Type 1F-3F) in percent of perforated floor pressure (perforated floor pressure = 500 pascals).



VELOCITY DISTRIBUTION ON CUTTING PLANE

Figure 5-5d. Velocity distribution (Type 1F-1F) in m/min.



VELOCITY DISTRIBUTION ON CUTTING PLANE

Figure 5-5e. Velocity distribution (Type 1F-3F) in m/min.

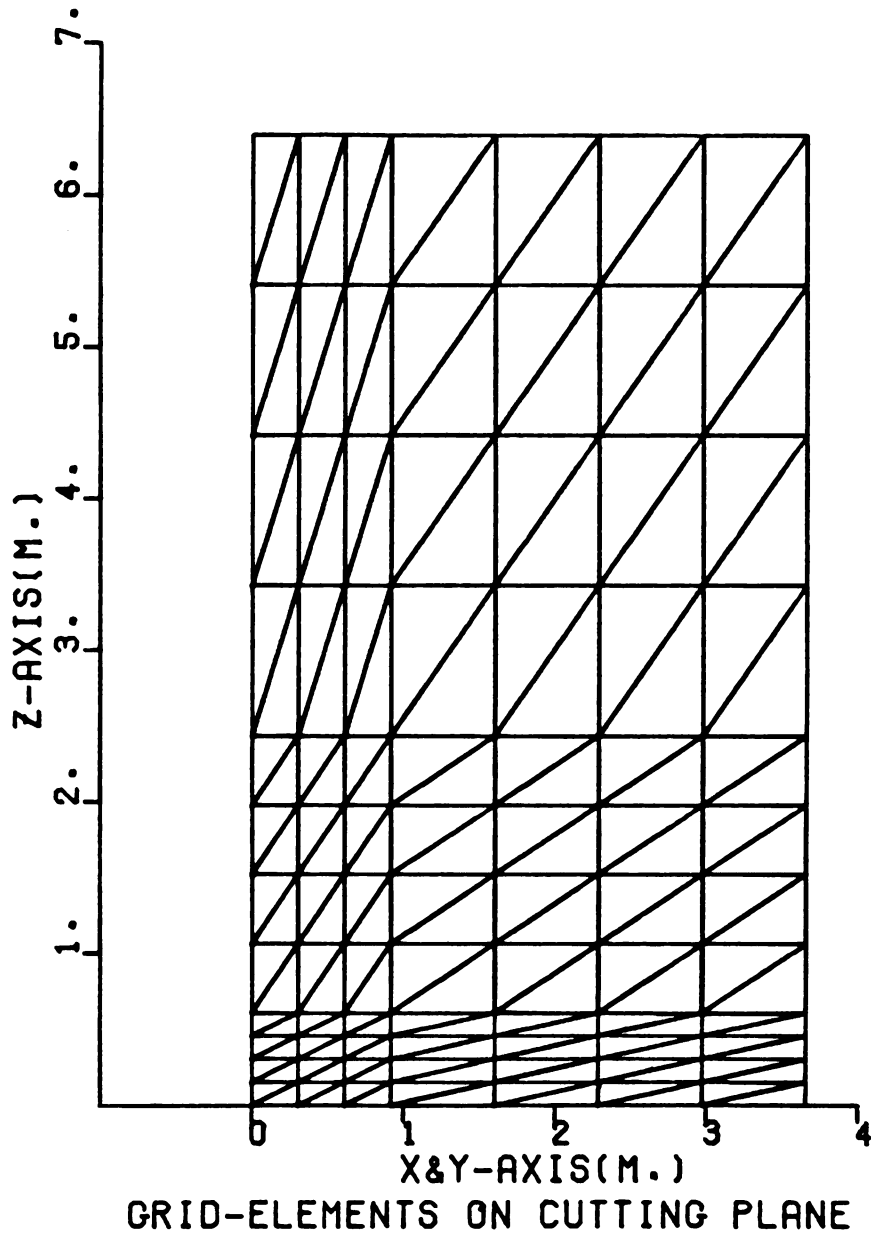
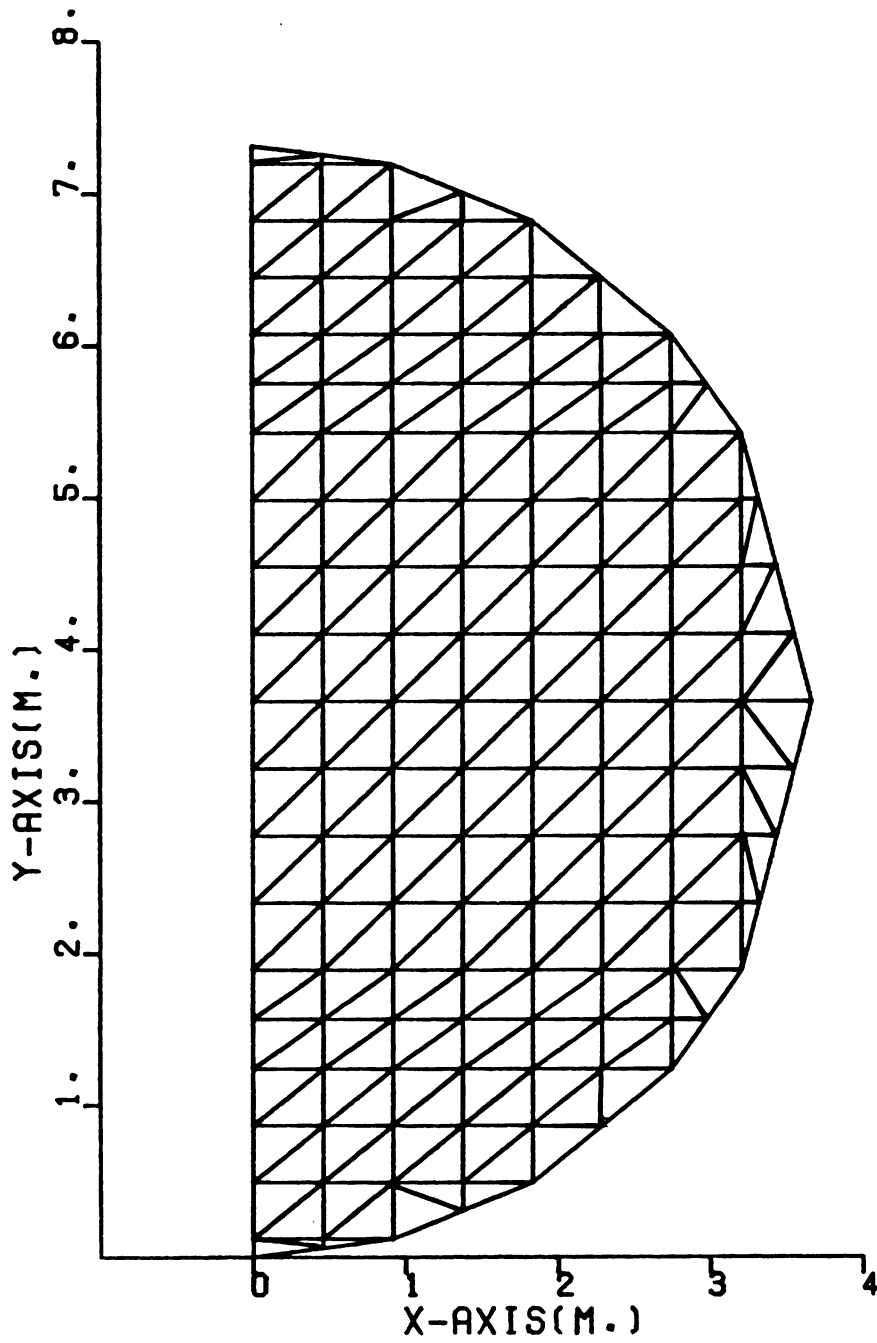
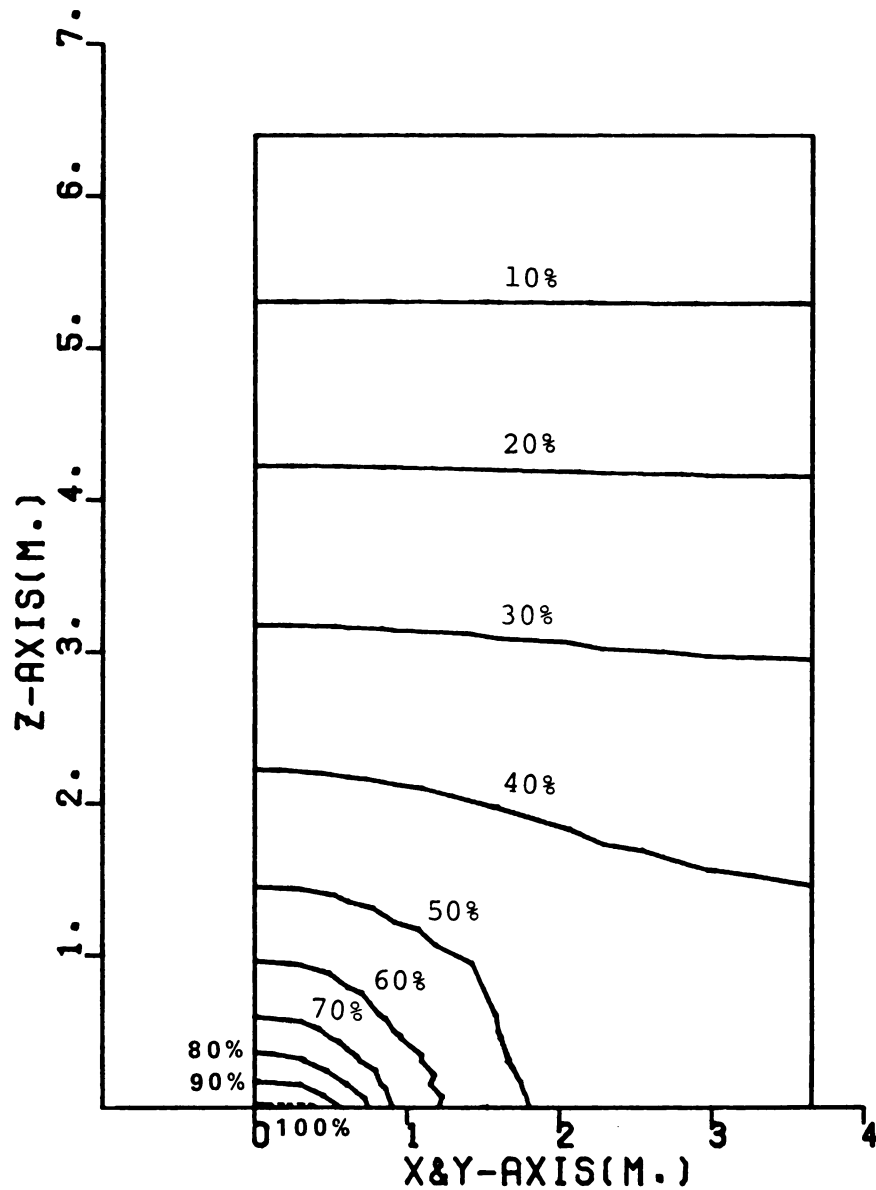


Figure 5-6a. Locations of the grid-elements on the cutting plane (Type 2-1).



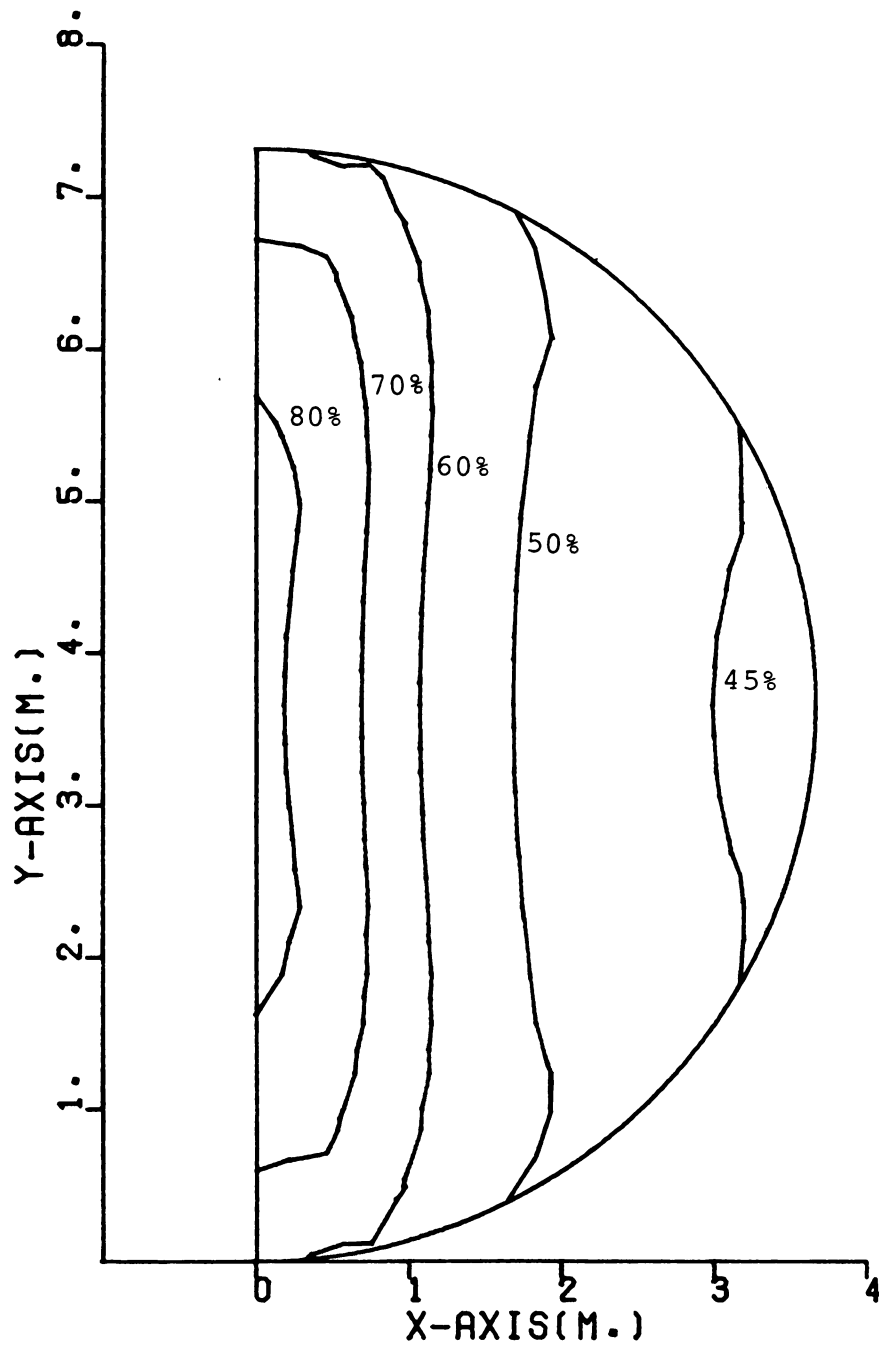
GRID-ELEMENTS ON CUTTING PLANE

Figure 5-6b. Locations of the grid-elements on the cutting plane (Type 2-2,2-3).



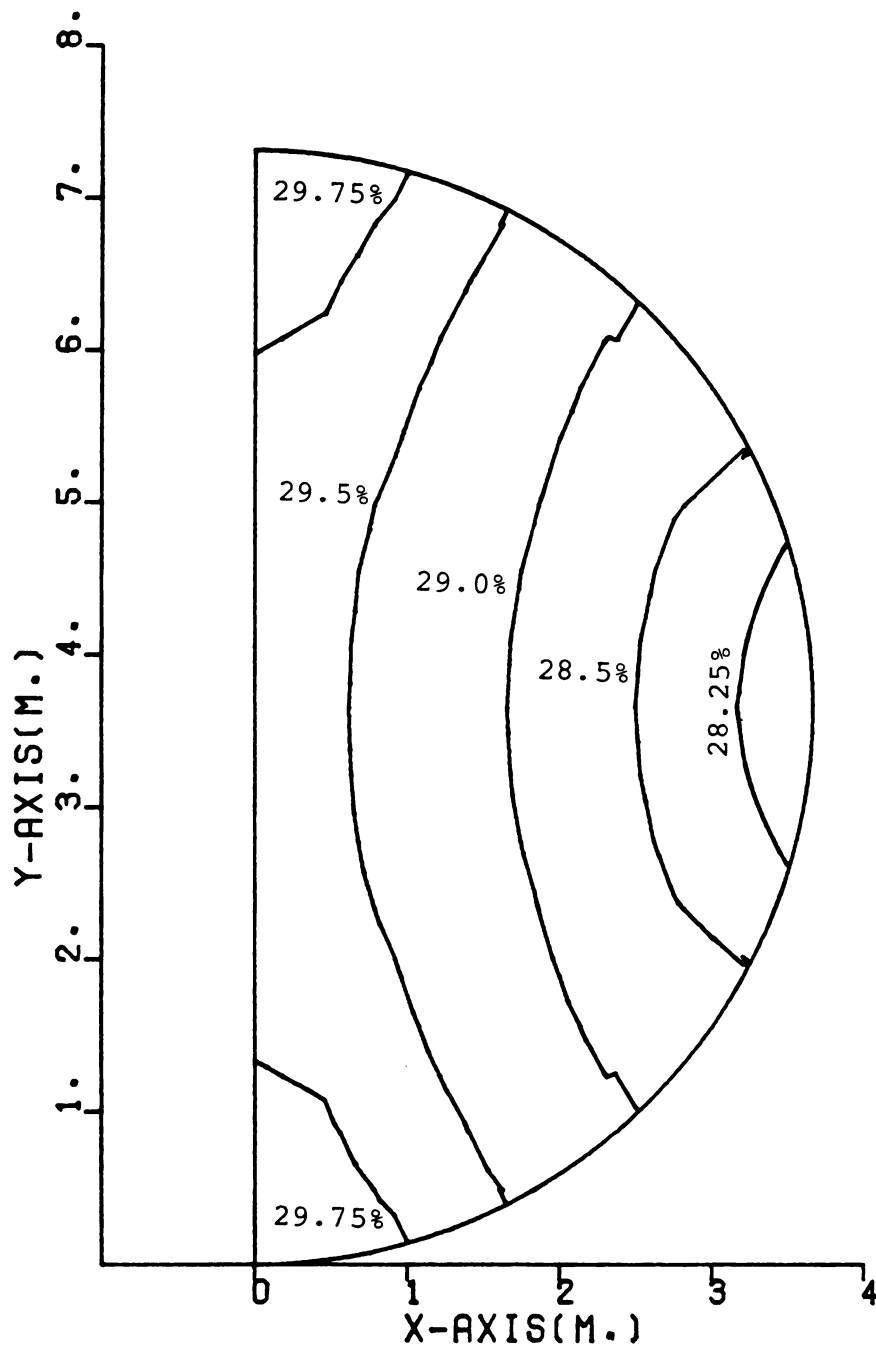
ISO-PRESSURE LINES ON CUTTING PLANE

Figure 5-6c. Pressure distribution (Type 2-1) in percent of perforated floor pressure (perforated floor pressure = 500 pascals).



ISO-PRESSURE LINES ON CUTTING PLANE

Figure 5-6d. Pressure distribution (Type 2-2) in percent of perforated floor pressure (perforated floor pressure = 500 pascals).



ISO-PRESSURE LINES ON CUTTING PLANE

Figure 5-6e. Pressure distribution (Type 2-3) in percent of perforated floor pressure (perforated floor pressure = 500 pascals).

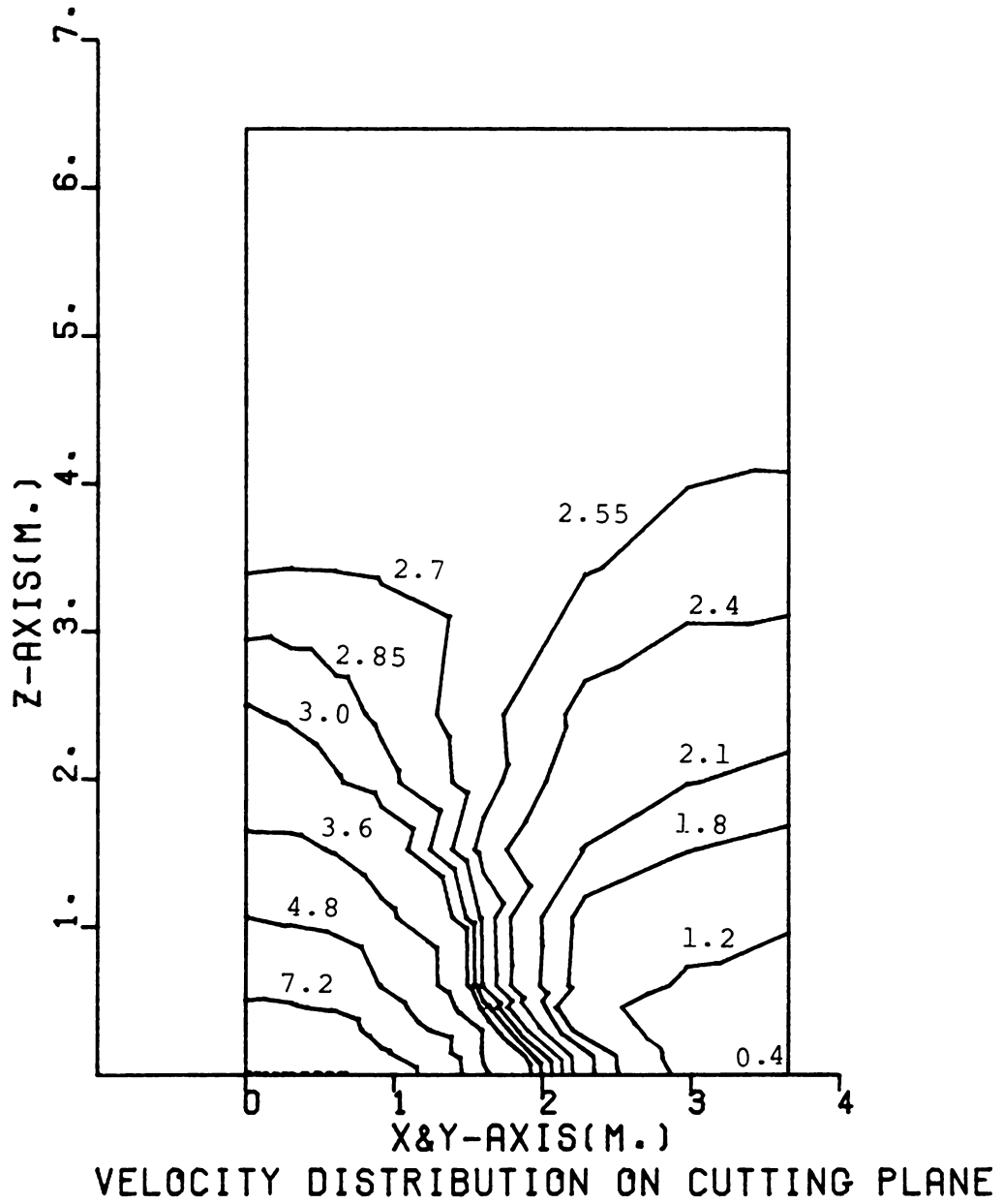
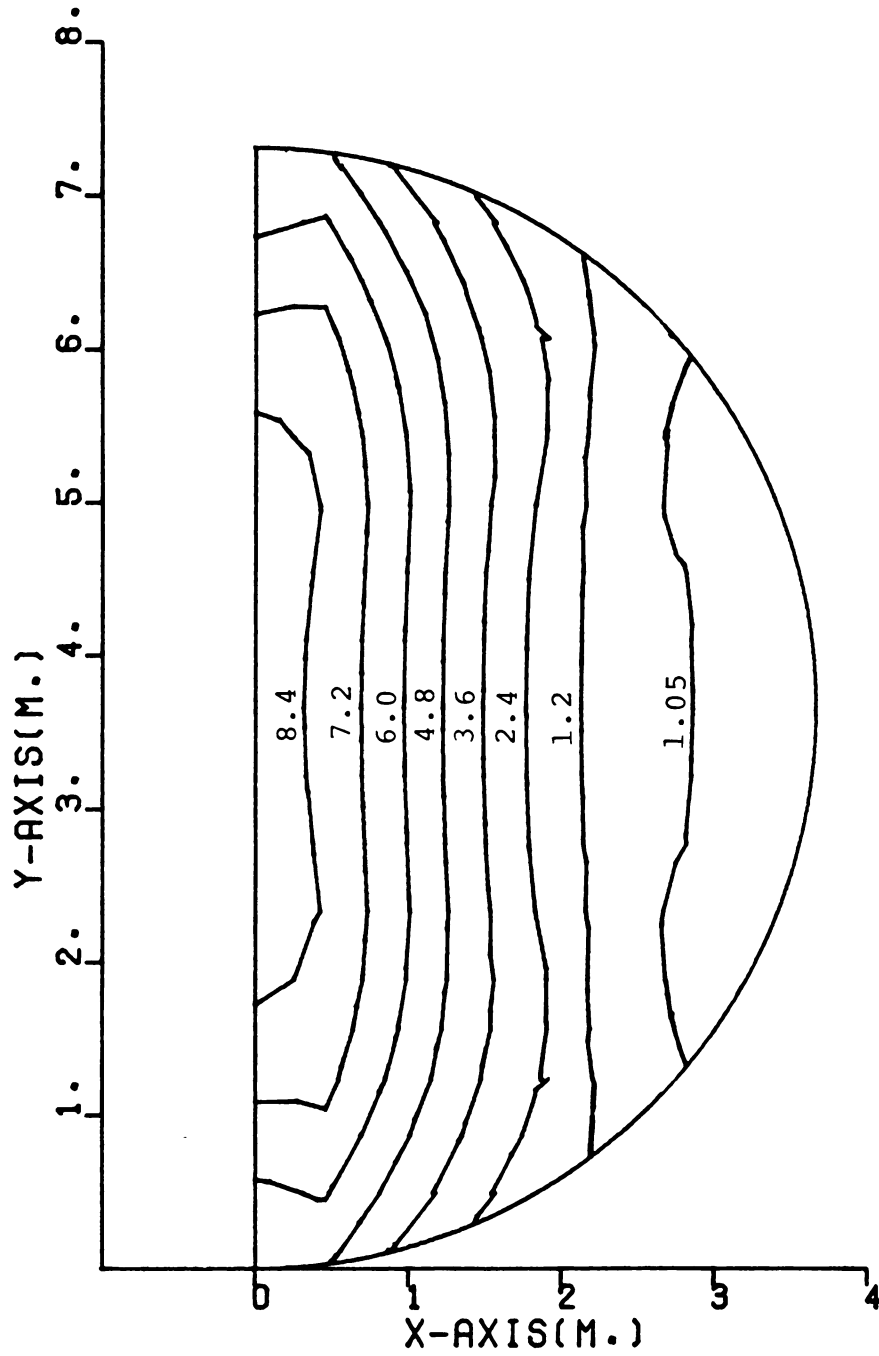


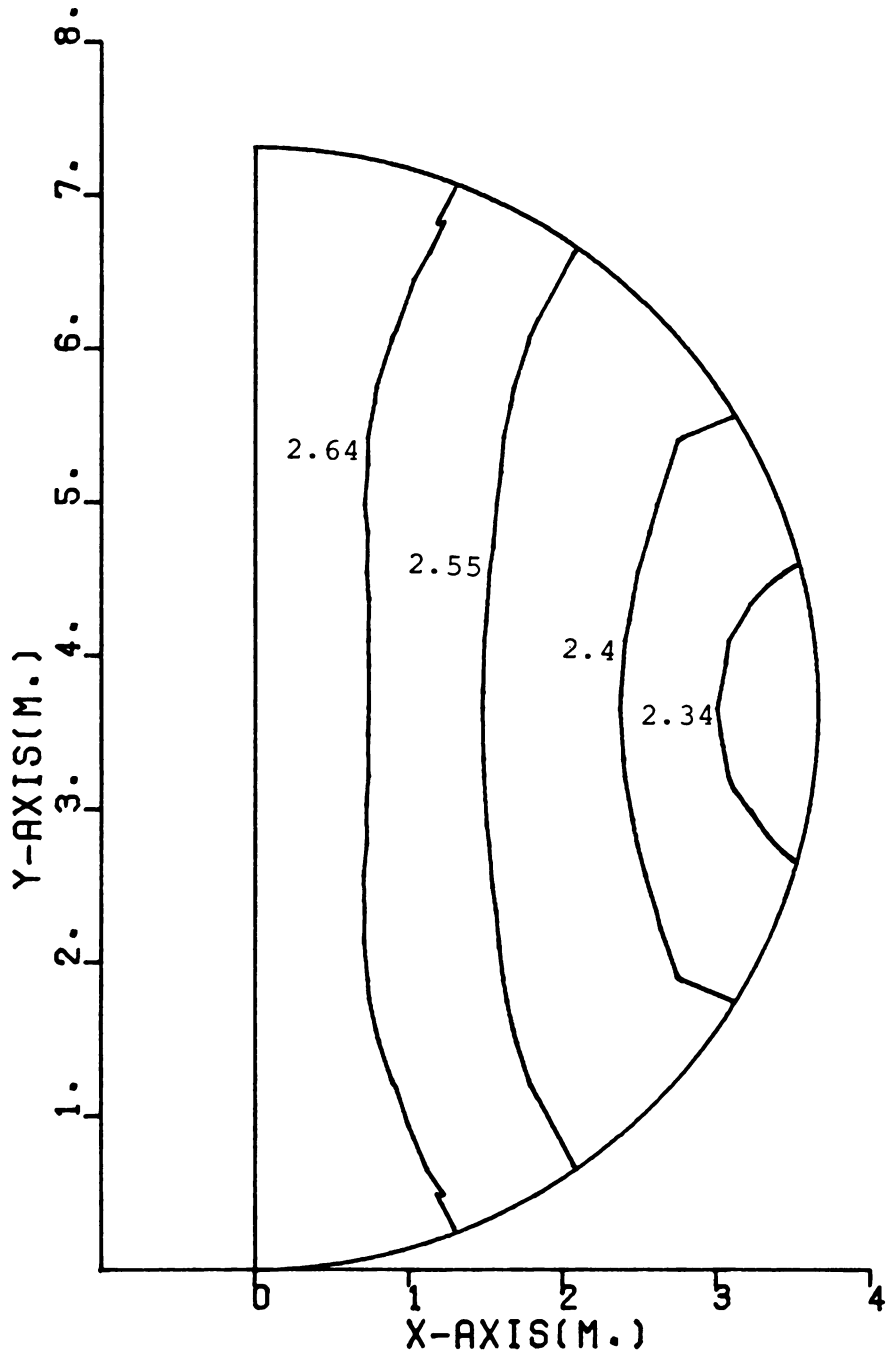
Figure 5-6f. Velocity distribution (Type 2-1) in m/min.





VELOCITY DISTRIBUTION ON CUTTING PLANE

Figure 5-6g. Velocity distribution (Type 2-2) in m/min.



VELOCITY DISTRIBUTION ON CUTTING PLANE

Figure 5-6h. Velocity distribution (Type 2-3) in m/min.

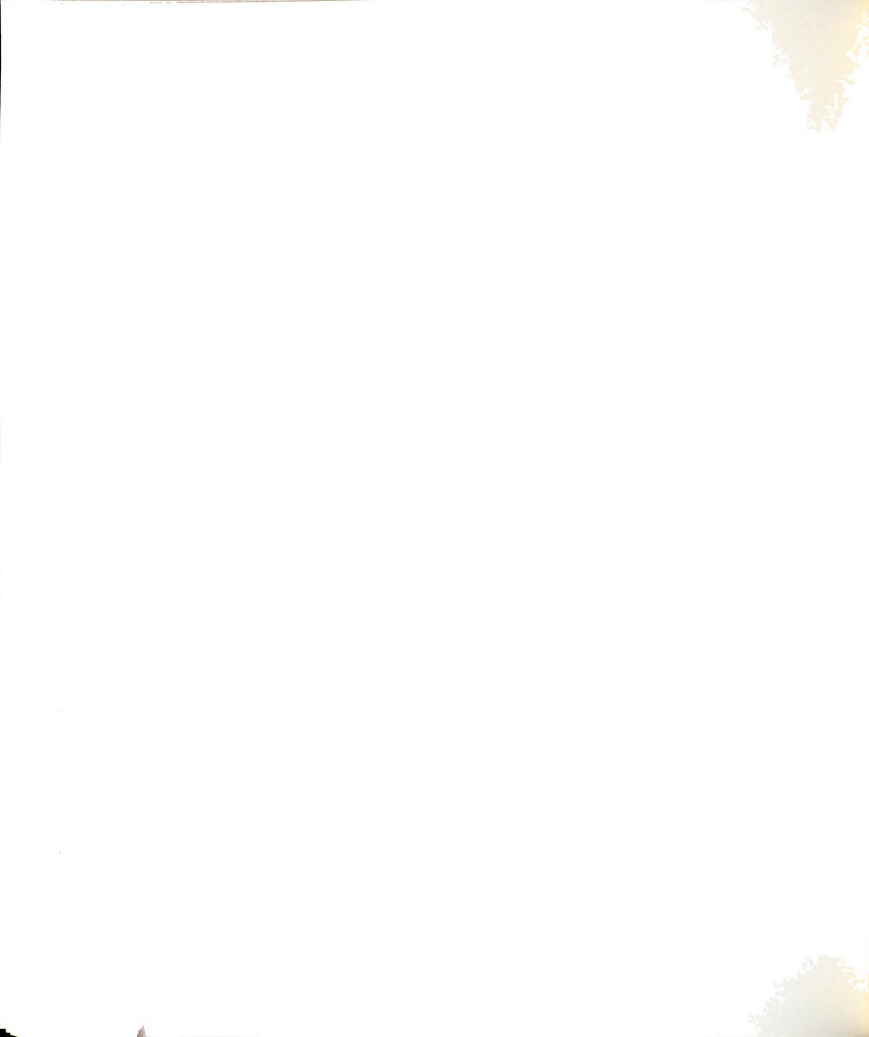


perforated floor system. The velocity decreases as the distance from the center of perforated floor increases. The velocity is nearly uniform for a depth exceeding 60% of the total height with values between 2.6 m/min. and 2.7 m/min. Figure 5-6f shows the minimum velocity between the bin wall and the floor to be about 0.4 m/min. This is the minimum velocity within the bin. There are two minimum velocity regions in the straight duct perforated floor system shown in Figure 5-6i.

5.5 PRESSURE AND VELOCITY DISTRIBUTIONS OF THE SQUARE DUCT PERFORATED FLOOR SYSTEM

The grid-elements on the cutting planes of the square duct perforated floor system are shown in Figures 5-7a and 5-7b. The pressure distributions for the square duct perforated floor system are presented in Figures 5-7c through 5-7e. The pressure changes in a relatively uniform manner with respect to the z-direction. The pressure is less than 40% of perforated floor pressure when the depth is over 50% of the total height of the grain storage. The pressure gradients (at high pressure values) are not as high as the pressure gradients observed for the straight duct perforated floor system (in Figure 5-6c). The pressure at the intersection of the bin wall and the floor is about 63% of the perforated floor pressure. At a level above 50% of the height the pressure decreases uniformly to less than 40% of the perforated floor pressure.

Figures 5-7f through 5-7h represent the velocity distributions for the square duct perforated floor system.



The maximum velocity location (about 5.3 m/min.) is located near the outer edge of the perforated floor (Figure 5-7) where the highest pressure gradient occurs. The velocity decreases rapidly up to the depth of 15% of the height. The velocity at a depth above 50% of the height is relatively uniform ranging between 1.80 and 1.95 m/min. The locations between the bin wall and the floor at the greatest distance perpendicular to the perforated floor have the lowest velocity values (about 0.7 m/min.). Figure 5-7i shows the four regions of the minimum velocity for the square duct perforated floor system. The regions are located on the bin floor.

5.6 PRESSURE AND VELOCITY DISTRIBUTIONS OF THE Y-DUCT PERFORATED FLOOR SYSTEM

Figures 5-8a and 5-8b show the grid elements on the cutting planes of the Y-duct perforated floor system. The pressure distributions for this perforated floor system at different locations are shown in Figures 5-8c through 5-8e. Figure 5-8c shows the pressure distribution on the cutting plane (Type 4-1P). The plane cuts perpendicular to the perforated floor (see Figure 4-1d) and has the greatest possible length, about 6.1 m. The pressure is very high near the perforated floor. The pressure decreases to less than 35% of the perforated floor pressure when the grain depth is greater than 50% of the total height. The pressure becomes more uniform as the height is increased. Figures 5-8d



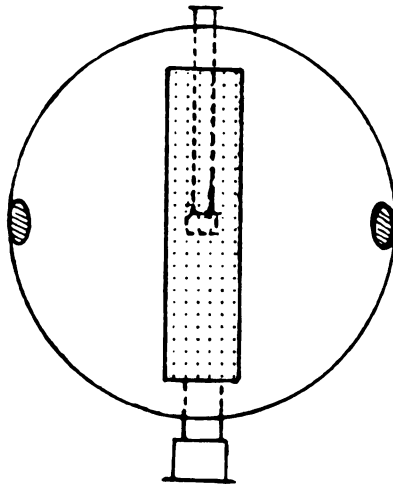
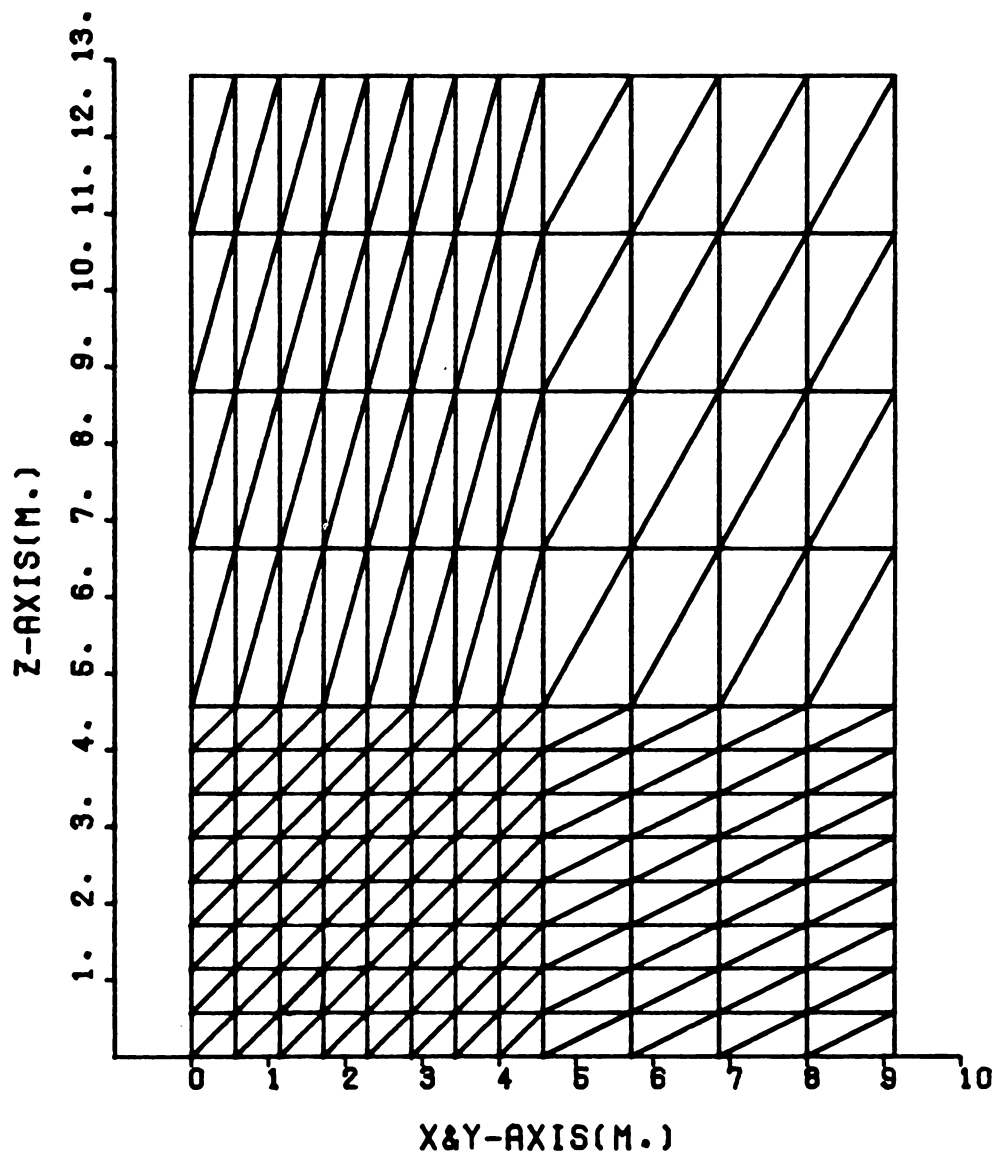


Figure 5-6i. The minimum velocity regions of the straight duct perforated floor system.

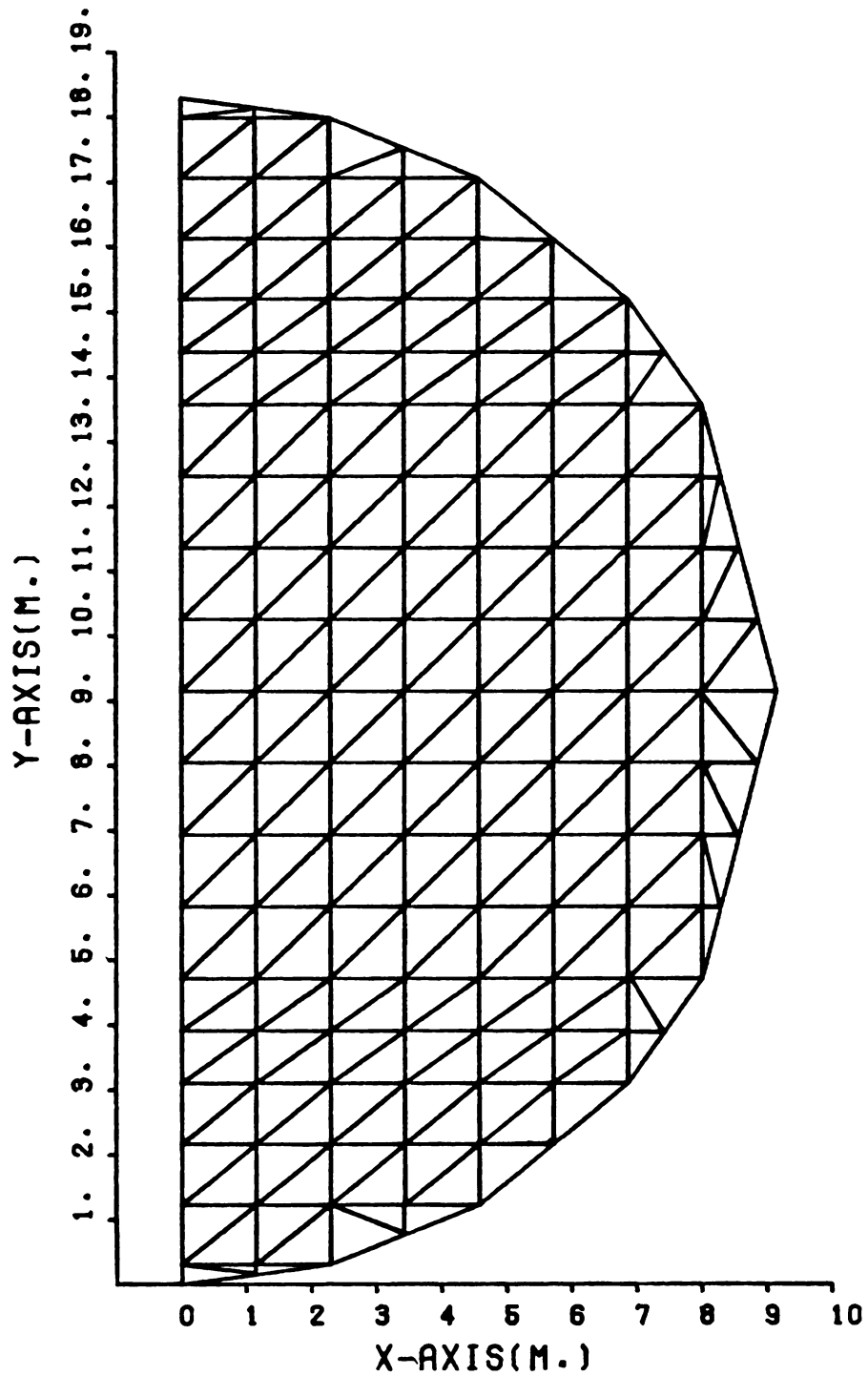




GRID-ELEMENTS ON CUTTING PLANE

Figure 5-7a. Locations of the grid-elements on the cutting plane (Type 3-1).

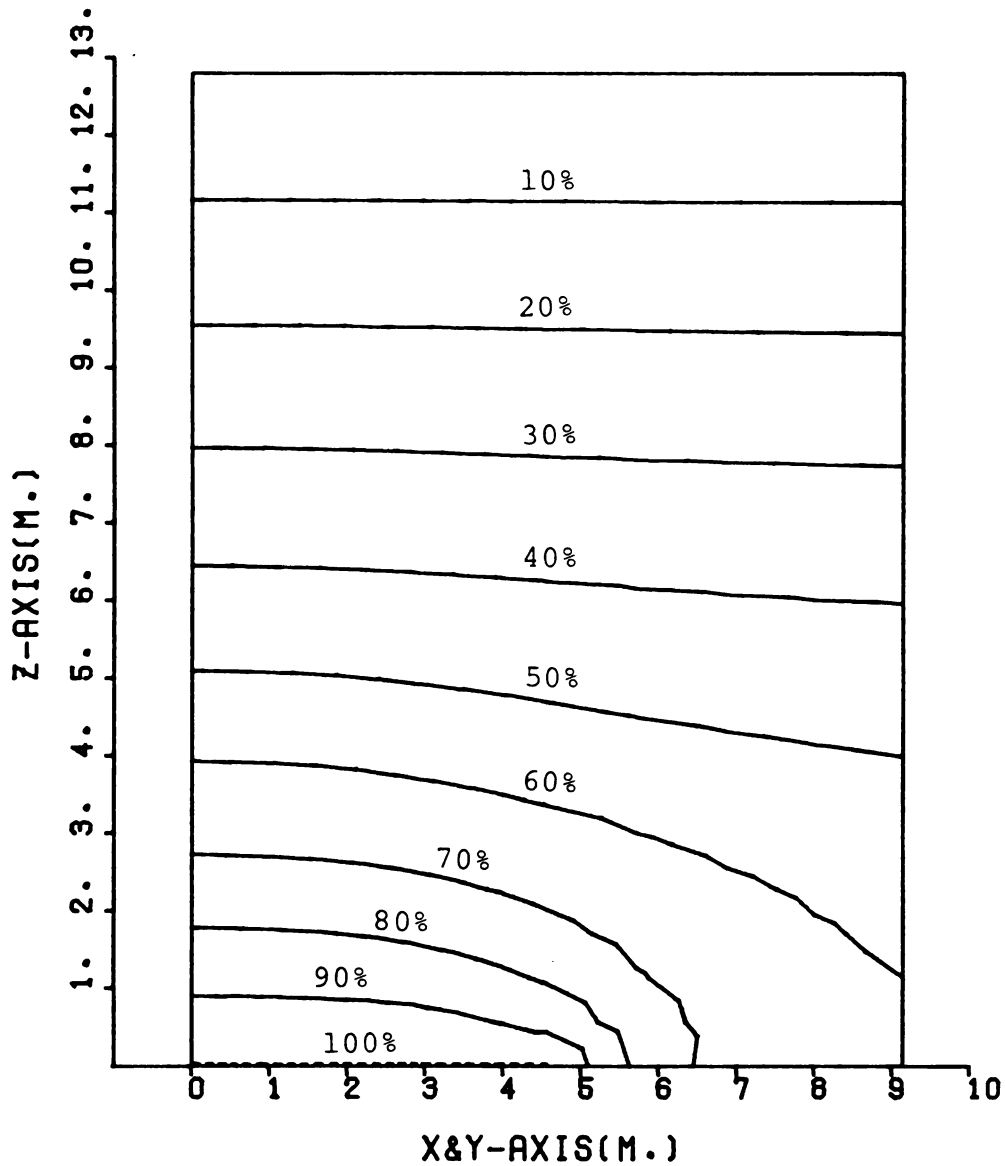




GRID-ELEMENTS ON CUTTING PLANE

Figure 5-7b. Locations of the grid-elements on the cutting plane (Type 3-2, 3-3).

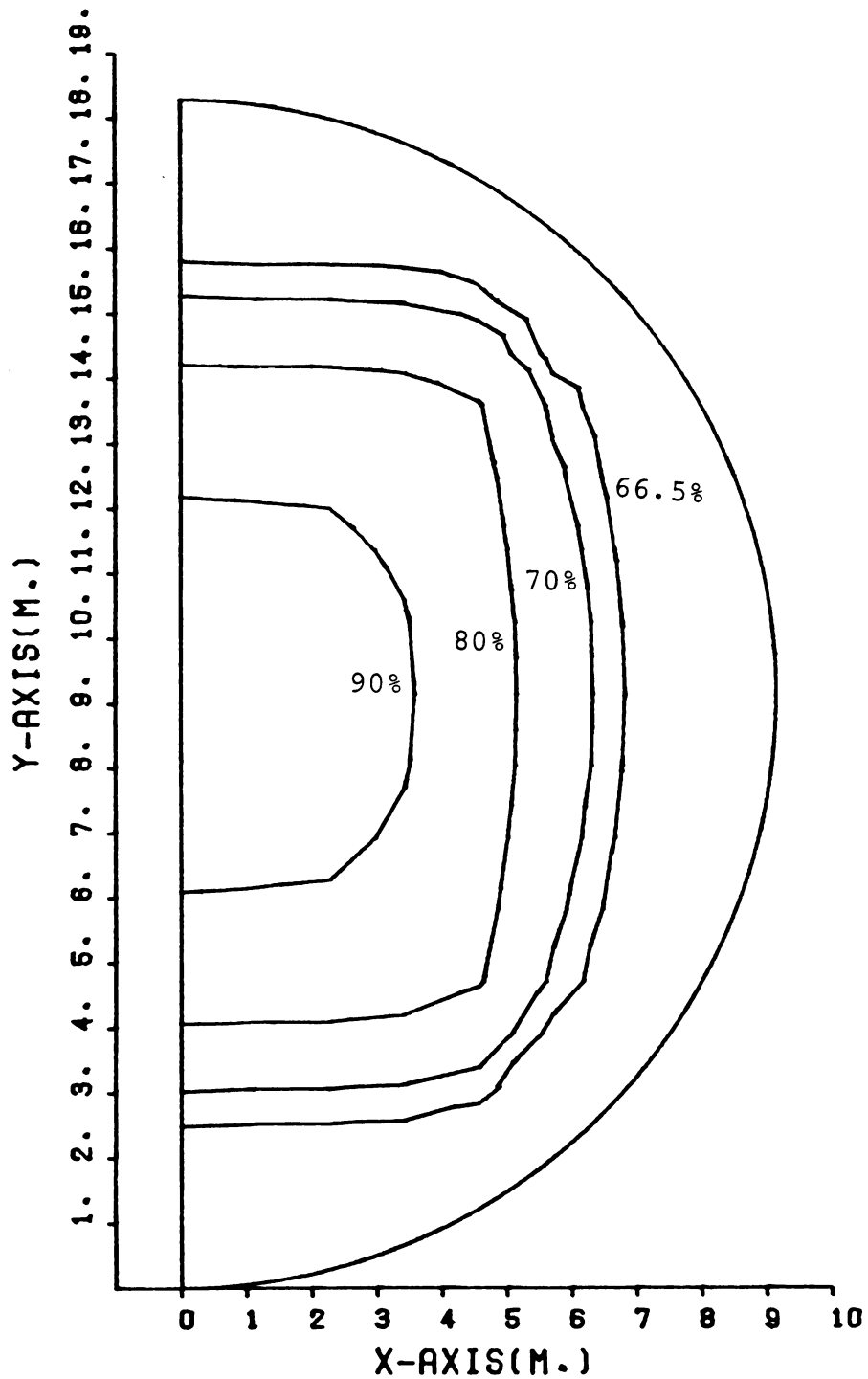




ISO-PRESSURE LINES ON CUTTING PLANE

Figure 5-7c. Pressure distribution (Type 3-1) in percent of perforated floor pressure (perforated floor pressure = 500 pascals).

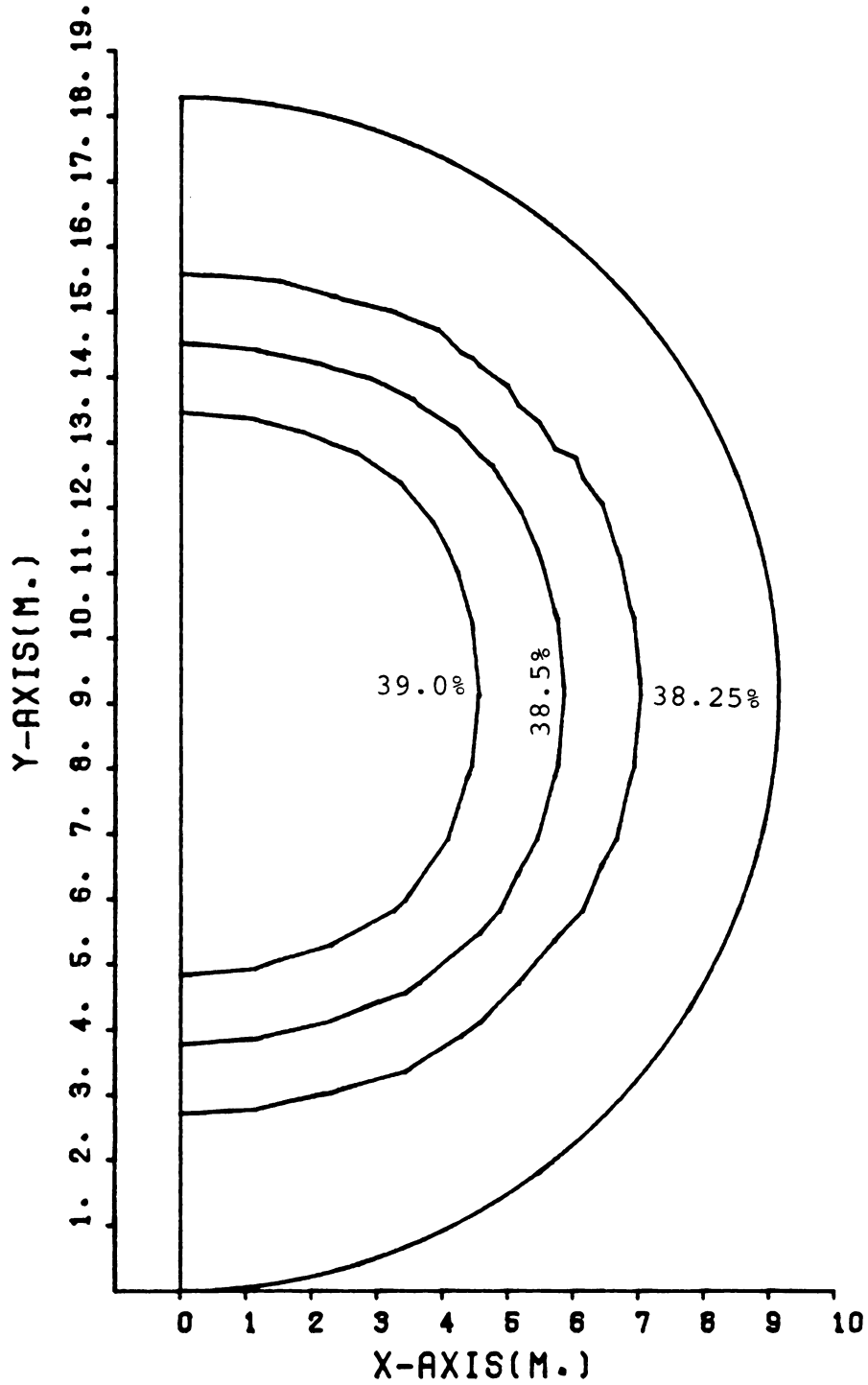




ISO-PRESSURE LINES ON CUTTING PLANE

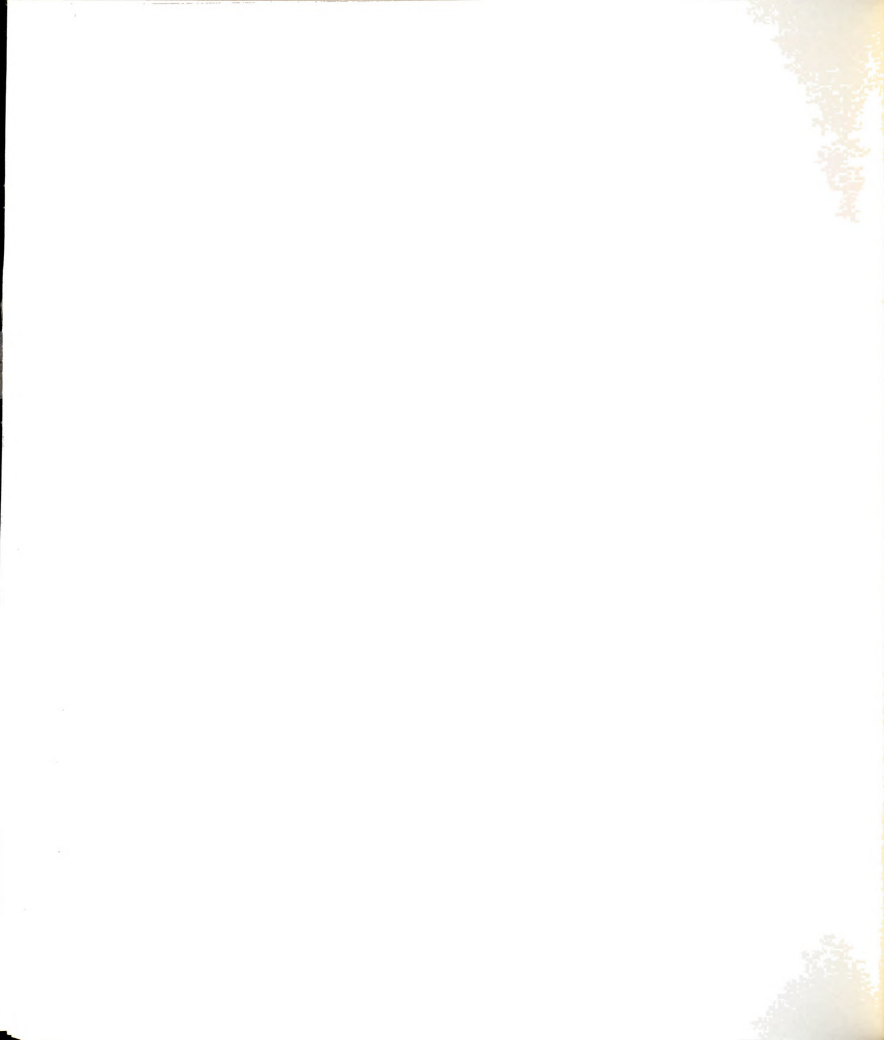
Figure 5-7d. Pressure distribution (Type 3-2) in percent of perforated floor pressure (perforated floor pressure = 500 pascals).

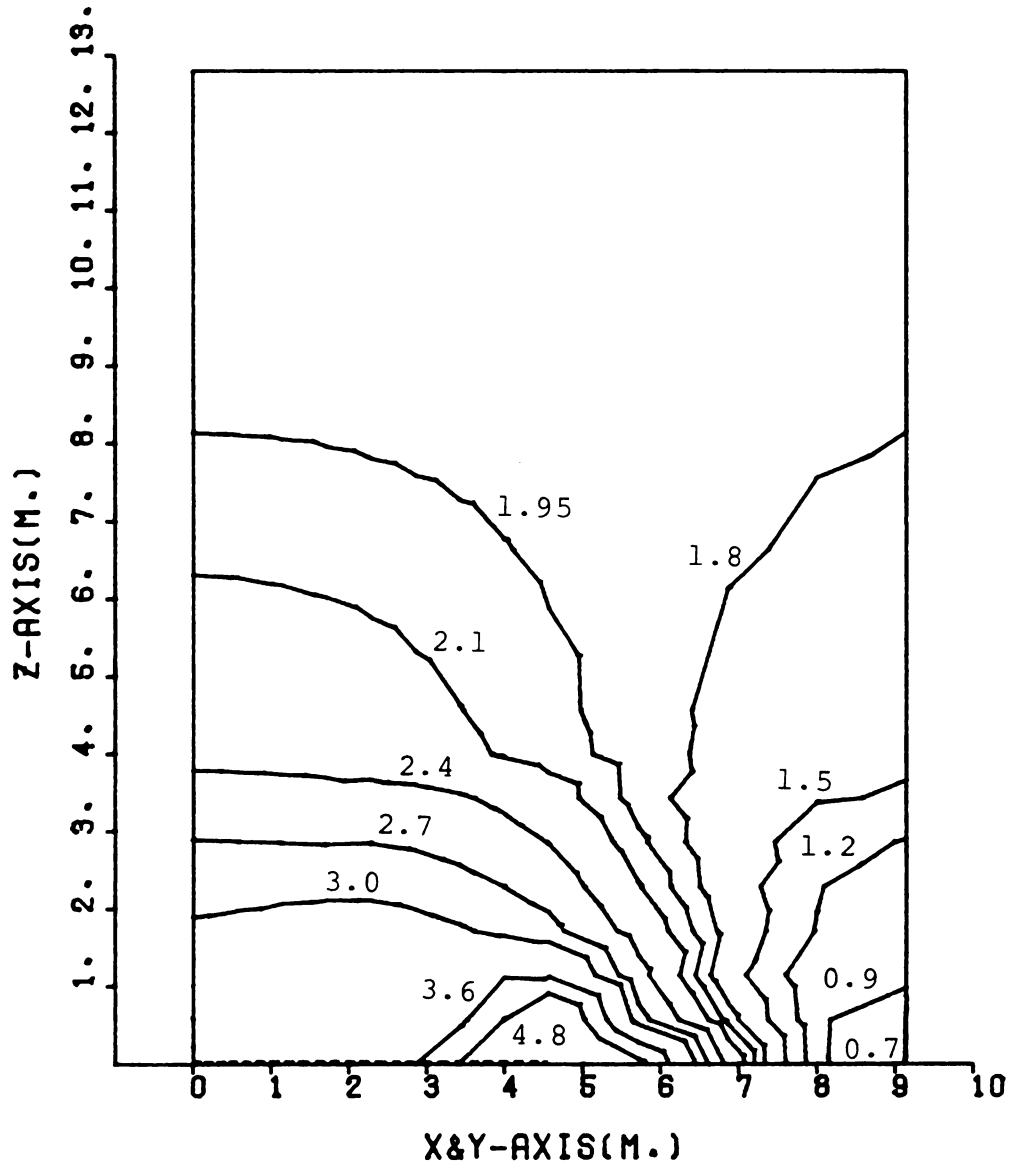




ISO-PRESSURE LINES ON CUTTING PLANE

Figure 5-7e. Pressure distribution (Type 3-3) in percent of perforated floor pressure (perforated floor pressure = 500 pascals).

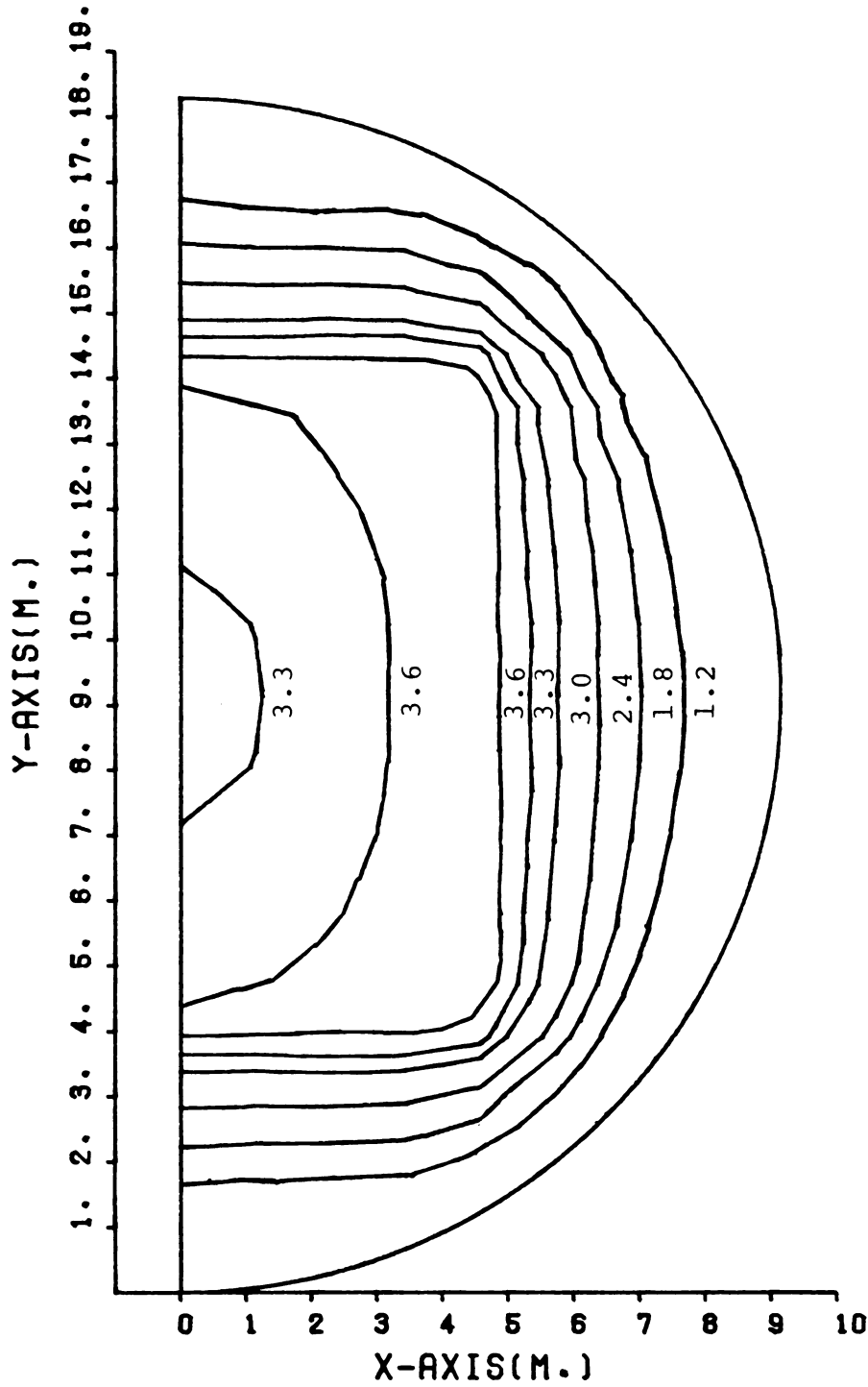




VELOCITY DISTRIBUTION ON CUTTING PLANE

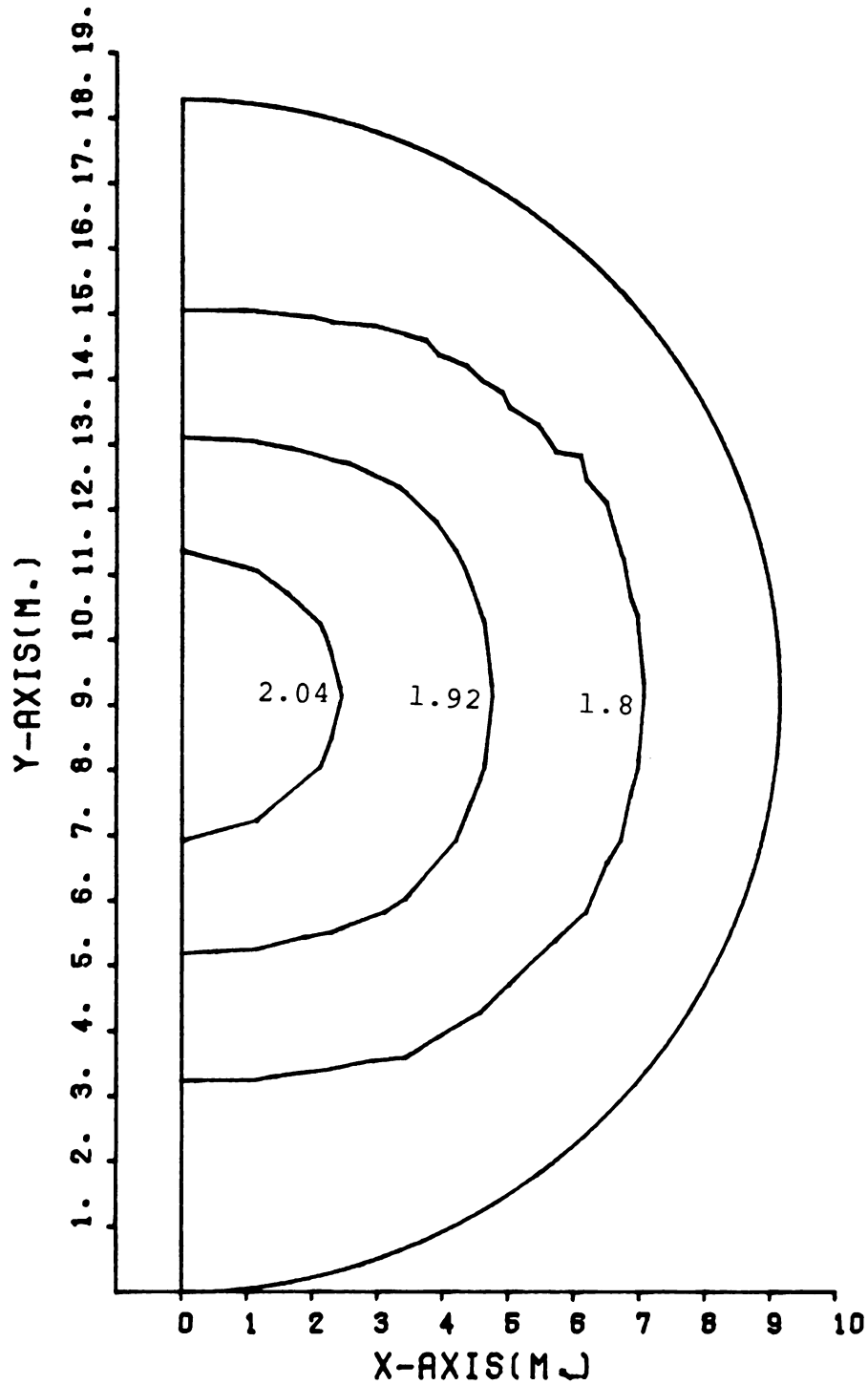
Figure 5-7f. Velocity distribution (Type 3-1) in m/min.





VELOCITY DISTRIBUTION ON CUTTING PLANE

Figure 5-7g. Velocity distribution (Type 3-2) in m/min.



VELOCITY DISTRIBUTION ON CUTTING PLANE

Figure 5-7h. Velocity distribution (Type 3-3) in m/min.

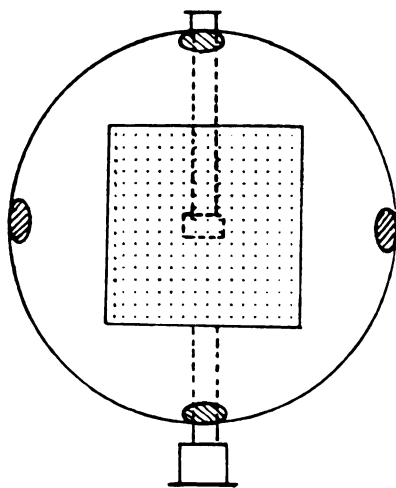
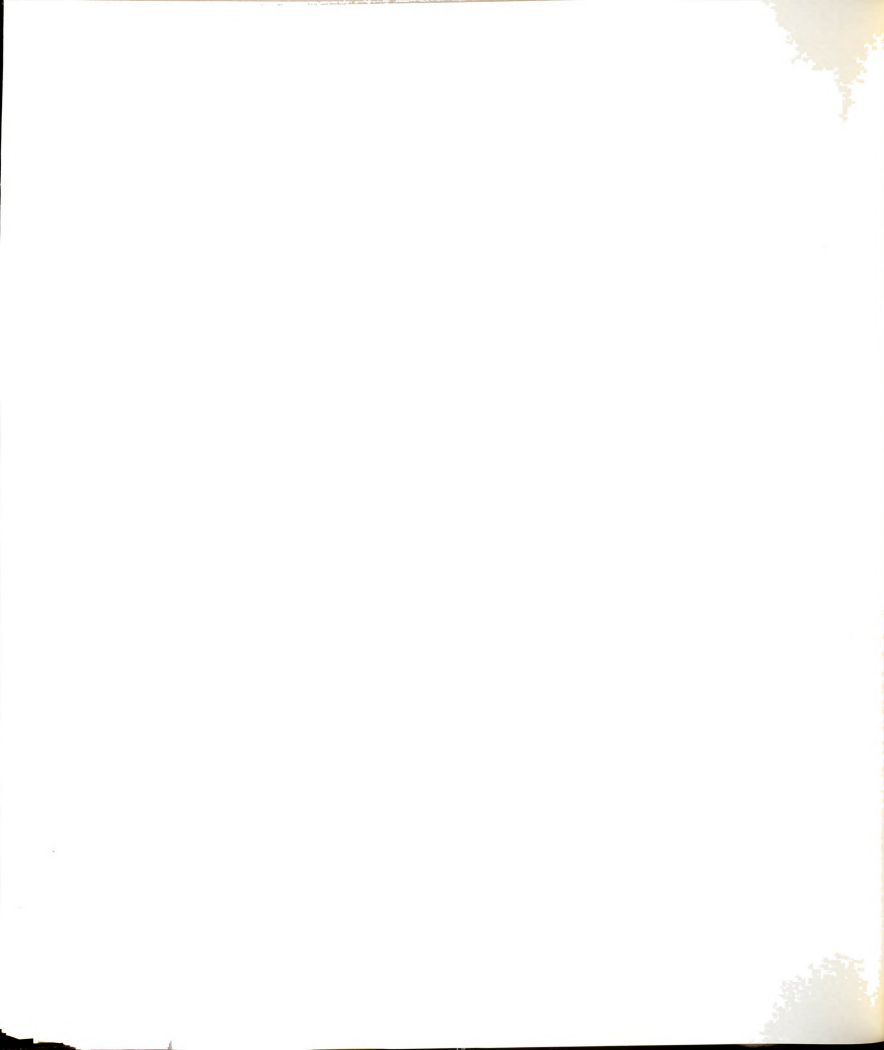
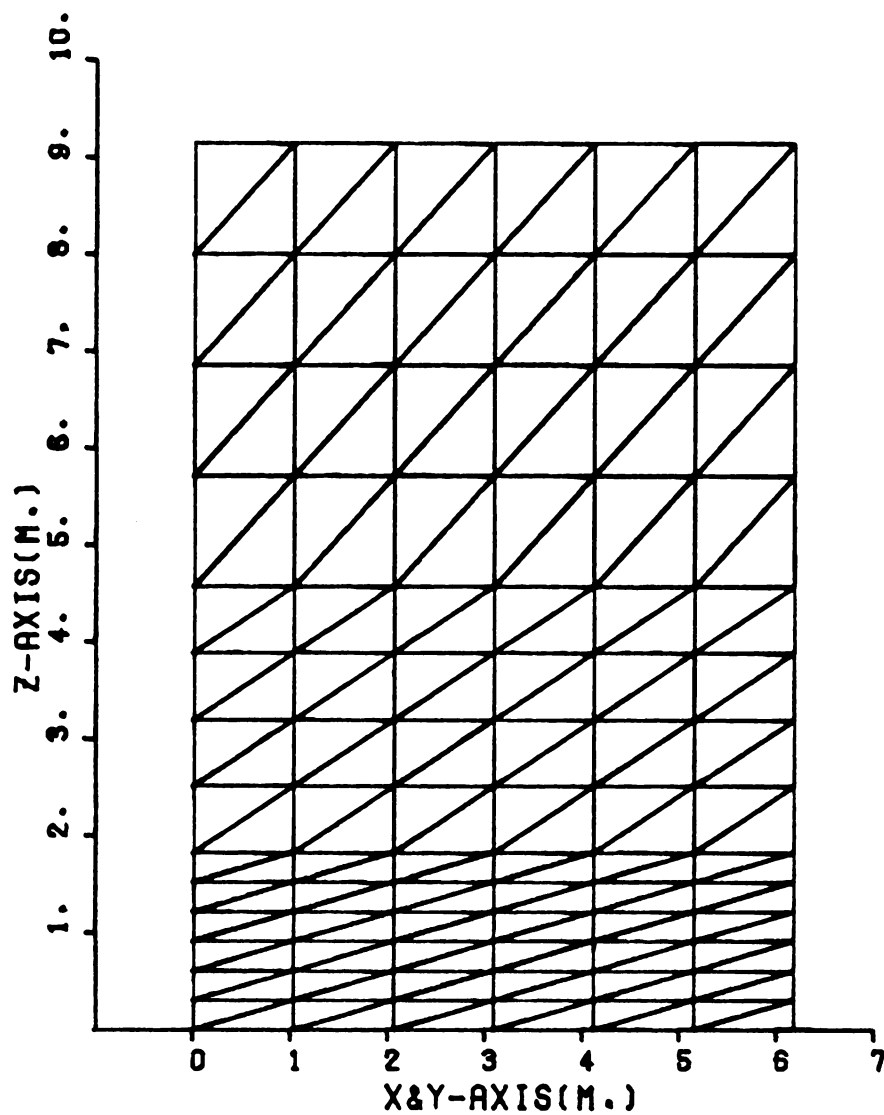


Figure 5-7i. The minimum velocity regions of the square duct perforated floor system.





GRID-ELEMENTS ON CUTTING PLANE

Figure 5-8a. Locations of the grid-elements on the cutting plane (Type 4-1P).



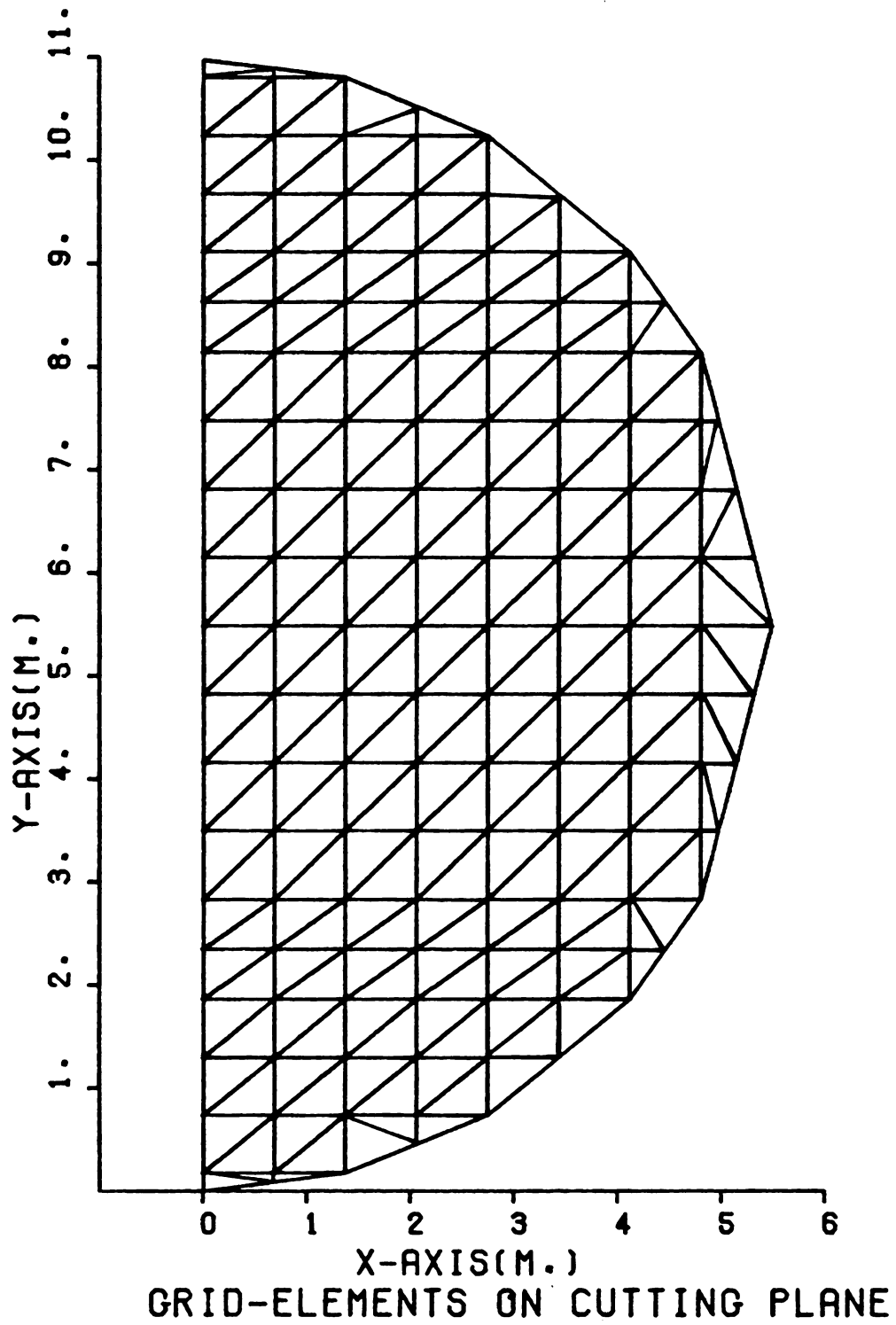
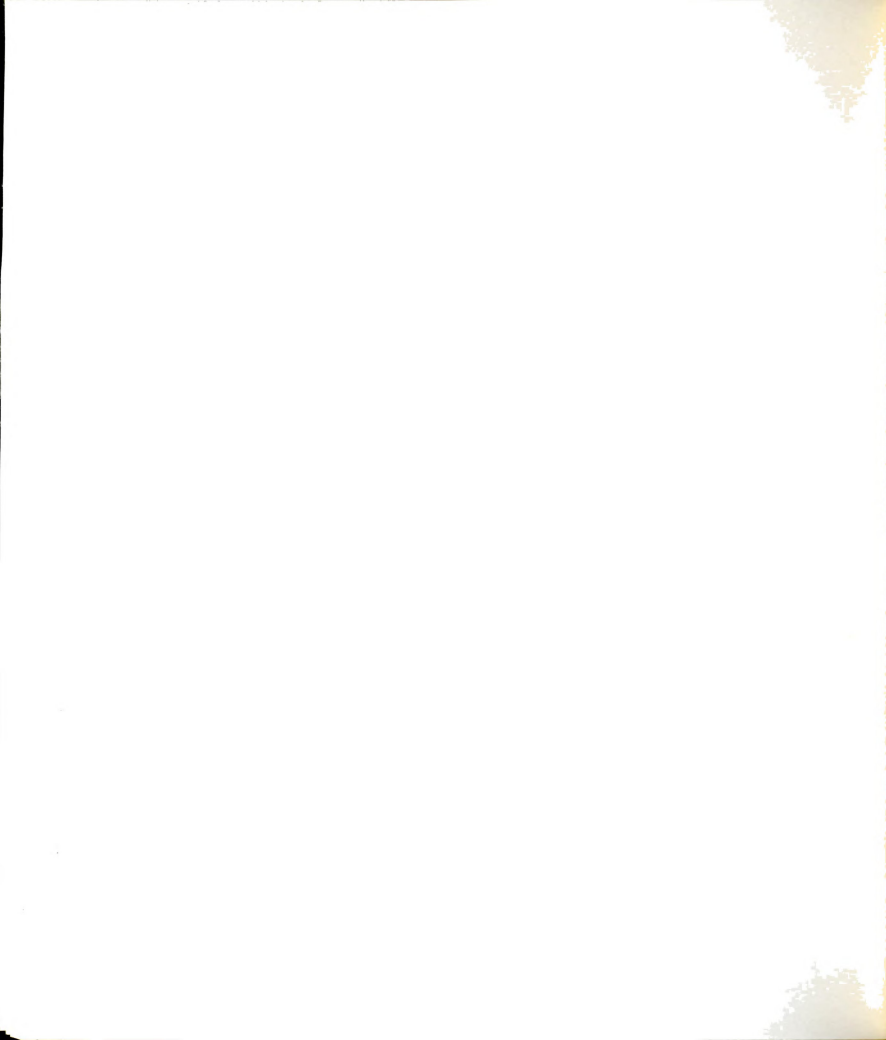
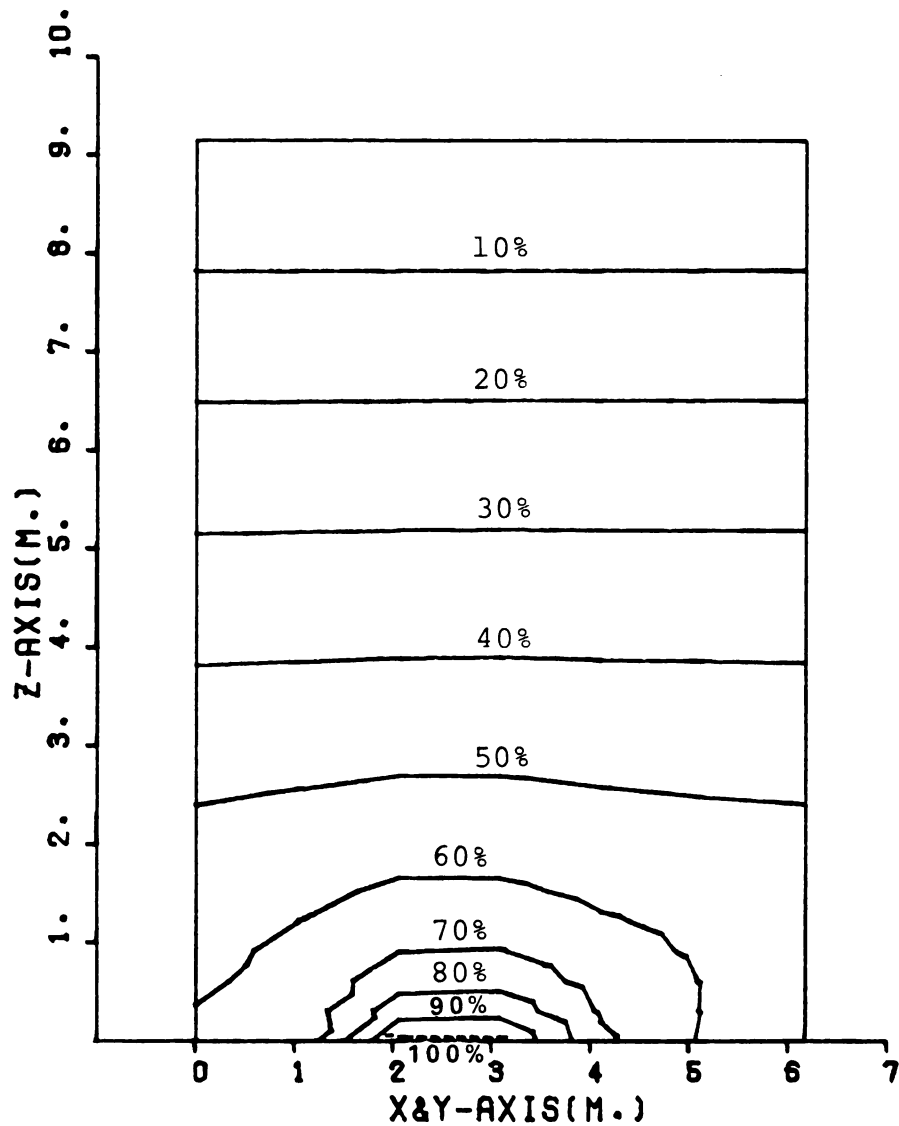


Figure 5-8b. Locations of the grid-elements on the cutting plane (Type 4-2, 4-3).





ISO-PRESSURE LINES ON CUTTING PLANE

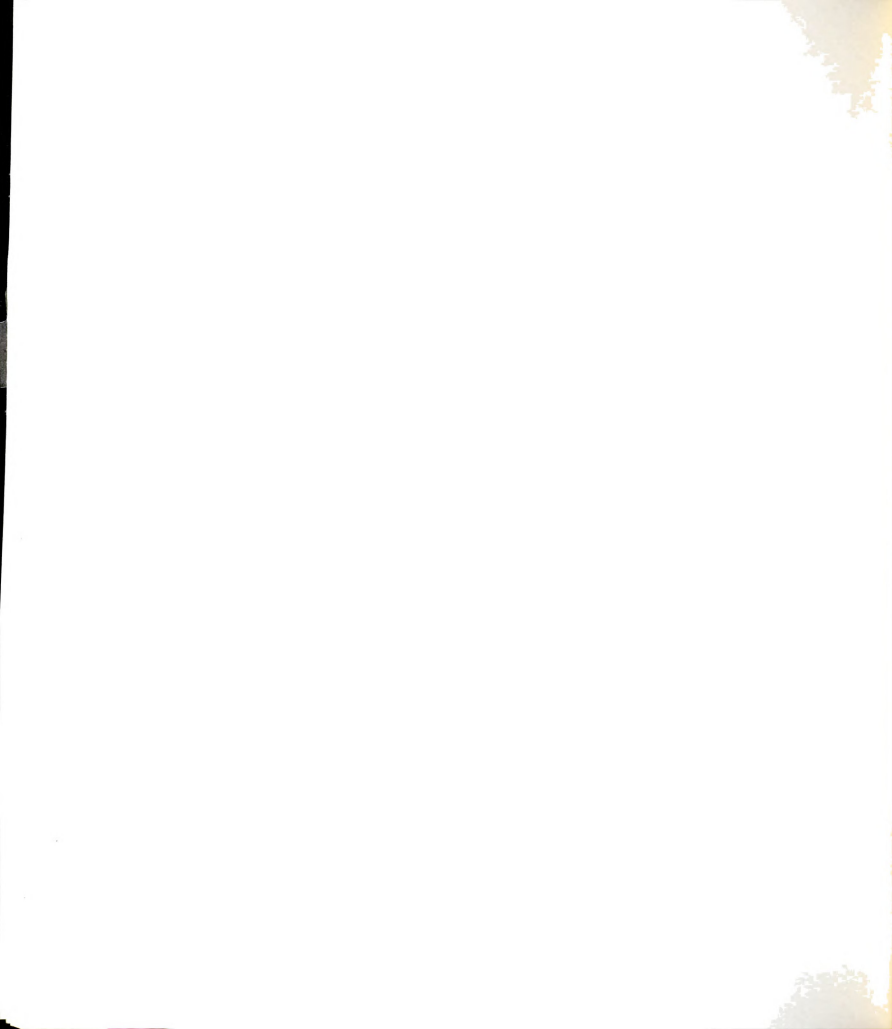
Figure 5-8c. Pressure distribution (Type4-1P) in percent of perforated floor pressure (perforated floor pressure = 500 pascals).



and 5-8e show the pressure distributions at 5% and 50% of the total height. The pressure in Figure 5-8d varies between 80% and 57% of the perforated floor pressure while the pressure in Figure 5-8e only varies between 35% and 33.5% of the perforated floor pressure.

Figures 5-8f through 5-8h represent the velocity distributions of the Y-duct perforated floor system. The velocity distributions are not easily understood because of the complicated duct configuration. Three-dimensional displays are needed in order to increase the visibility of its behavior. Some three-dimensional pressure and velocity displays are presented in the next section.

The two-dimensional results, however, indicated that the velocity near the perforated floor is quite high. The maximum velocity along the centerline of the perforated floor is about 8.8 m/min. The minimum velocity, about 0.8 m/min., is at the intersection of the bin wall and the floor, as shown in Figure 5-8f. There is another location where the velocity is very close to the minimum velocity at the intersection of the bin wall and the floor for the maximum value of y . The three minimum velocity regions are located in the Y-duct perforated floor system as shown in Figure 5-8i.



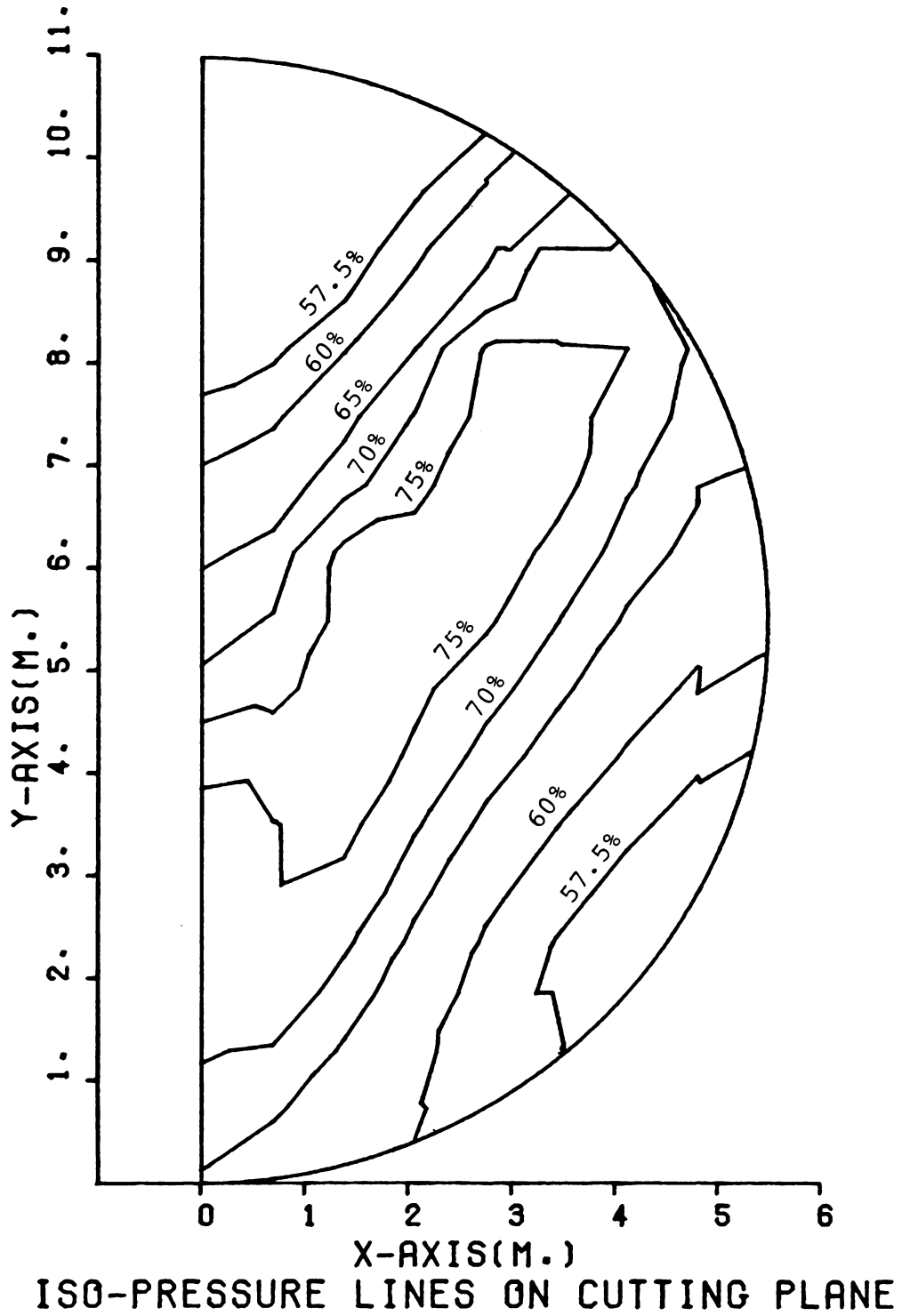
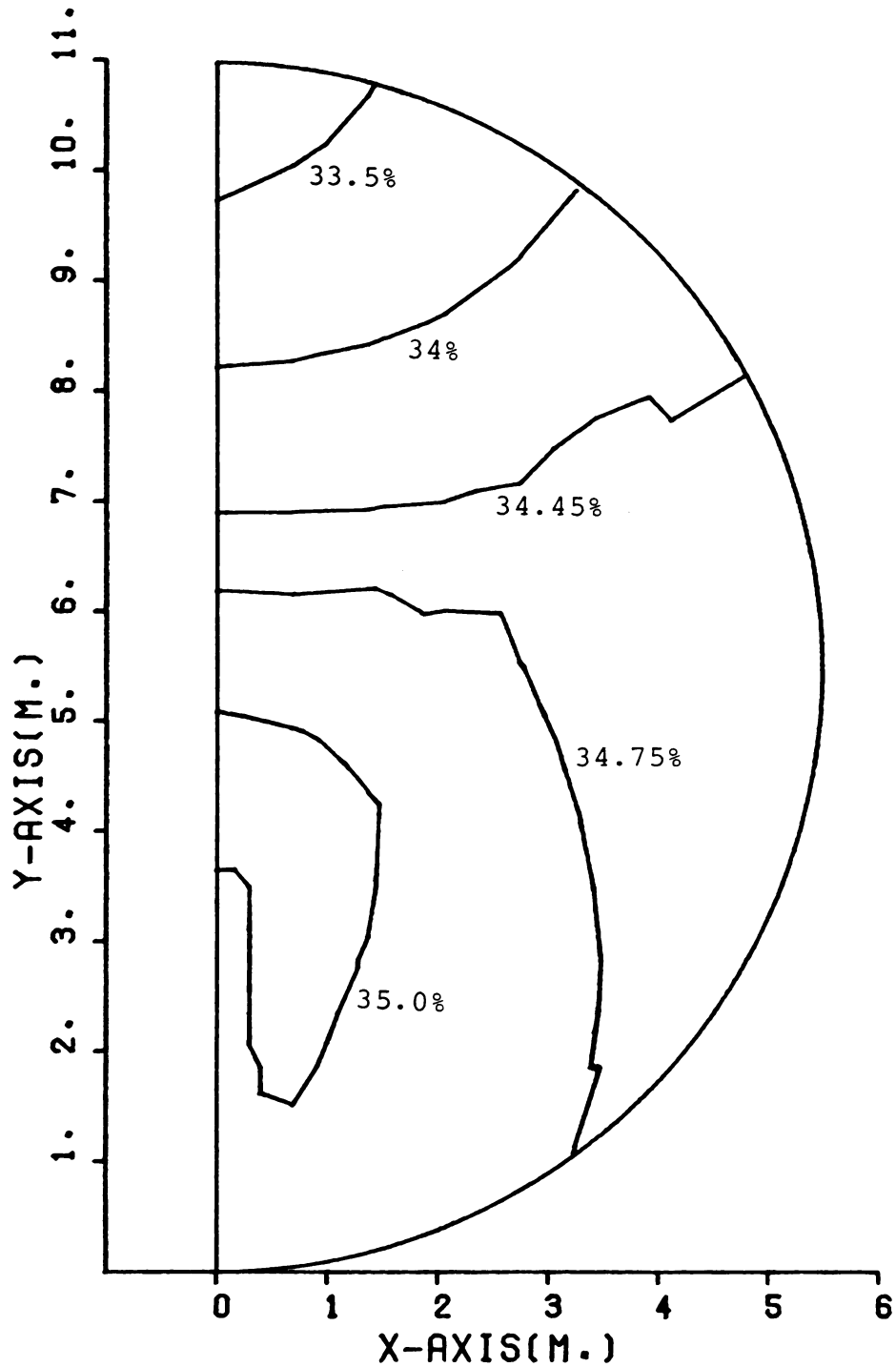
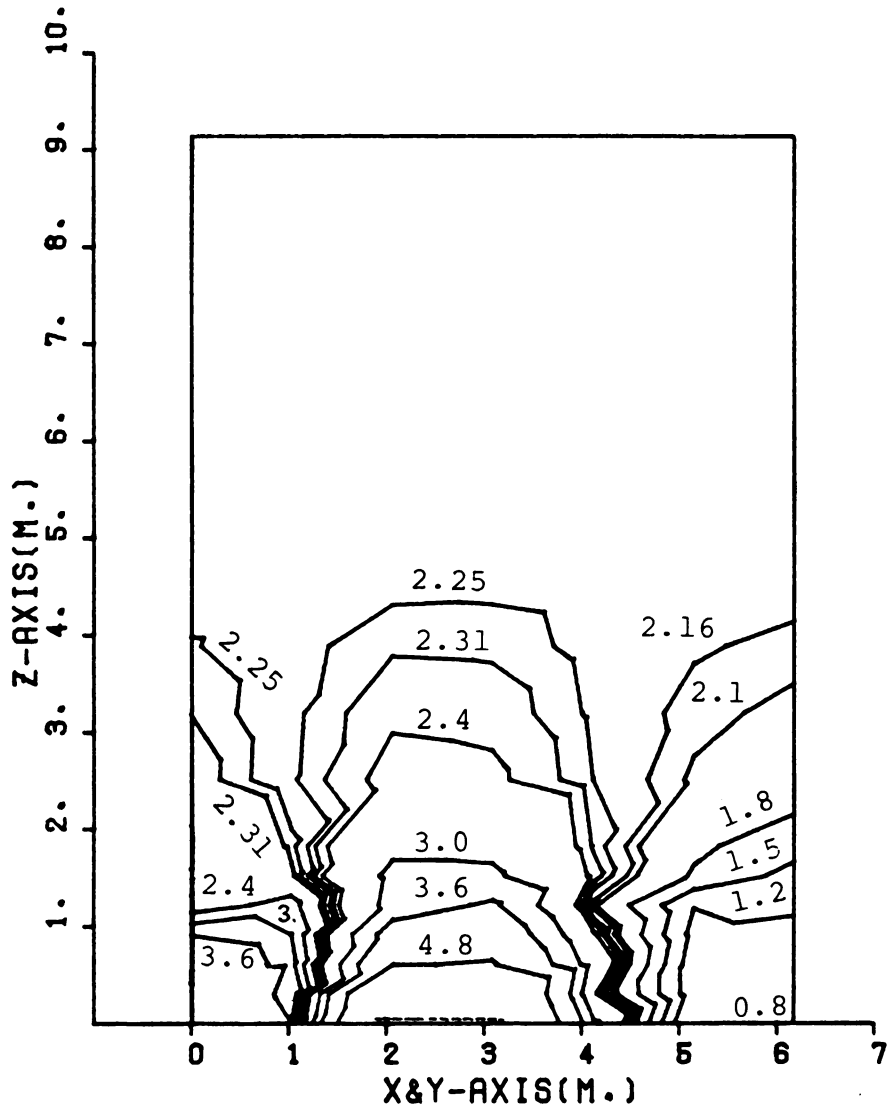


Figure 5-8d. Pressure distribution (Type 4-2) in percent of perforated floor pressure (perforated floor pressure = 500 pascals).



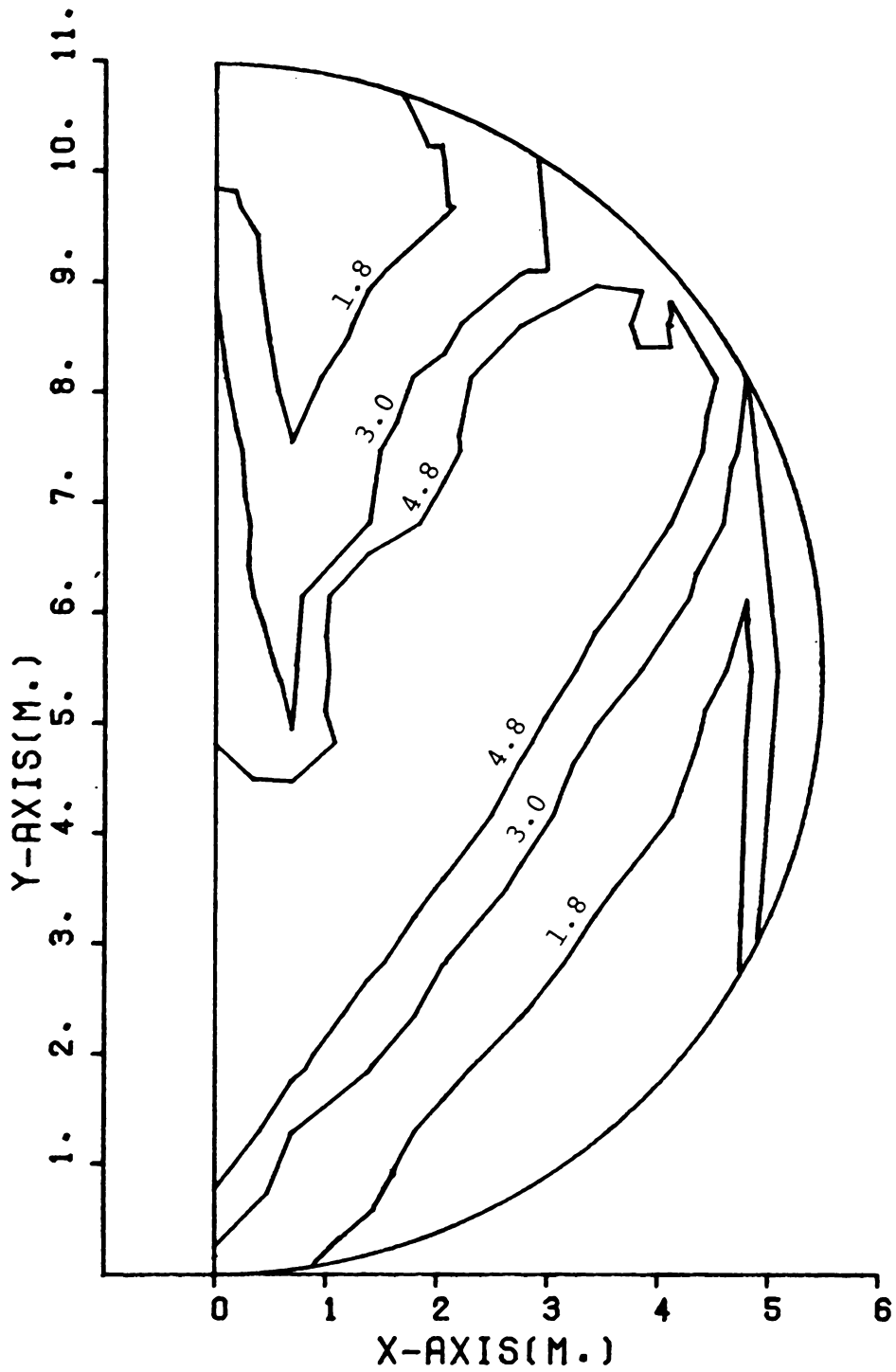
ISO-PRESSURE LINES ON CUTTING PLANE

Figure 5-8e. Pressure distribution (Type 4-3) in percent of perforated floor pressure (perforated floor pressure = 500 pascals).



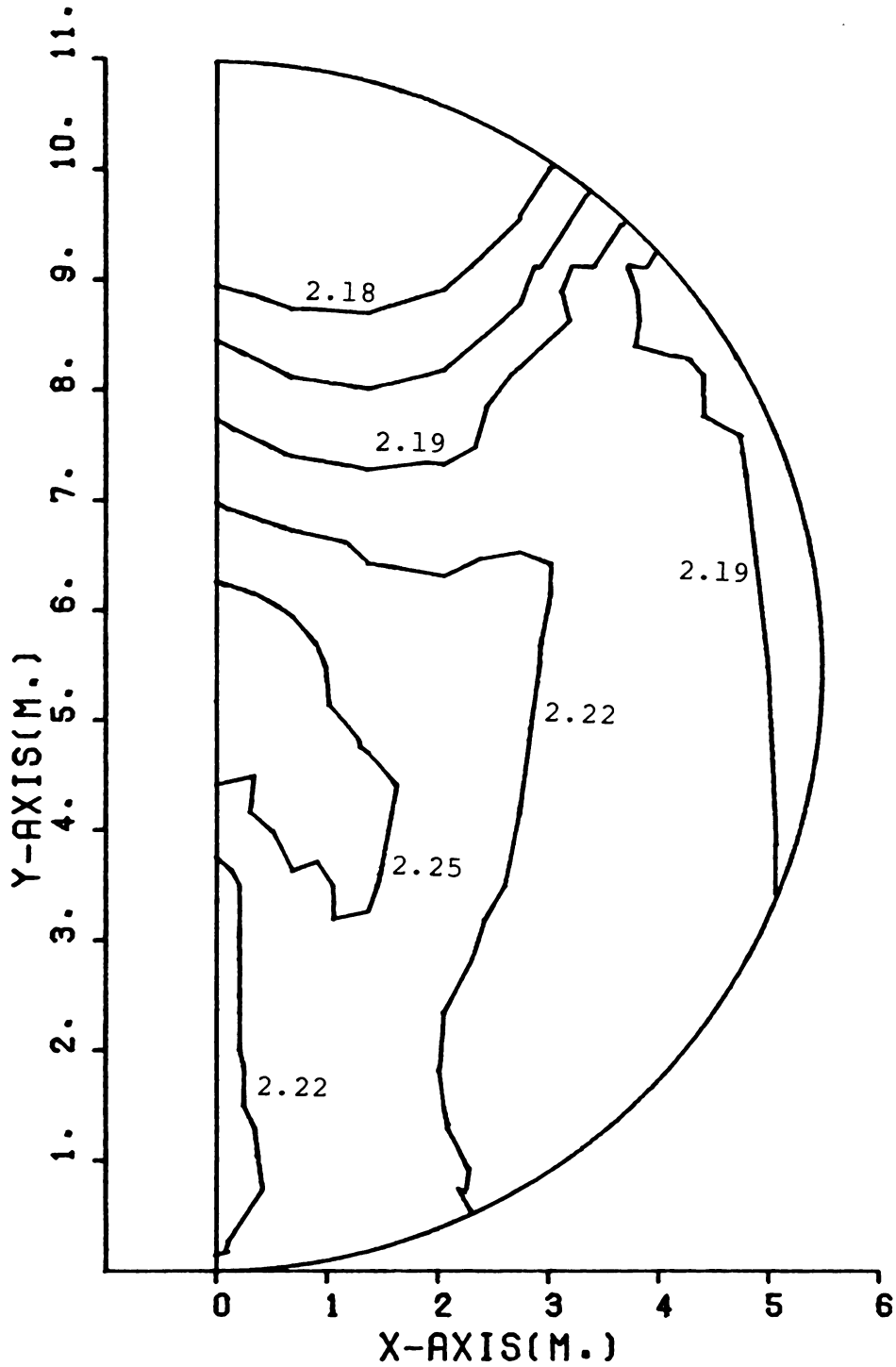
VELOCITY DISTRIBUTION ON CUTTING PLANE

Figure 5-8f. Velocity distribution (Type 4-1P) in m/min.



VELOCITY DISTRIBUTION ON CUTTING PLANE

Figure 5-8g. Velocity distribution (Type 4-2) in m/min.



VELOCITY DISTRIBUTION ON CUTTING PLANE

Figure 5-8h. Velocity distribution (Type 4-3) in m/min.

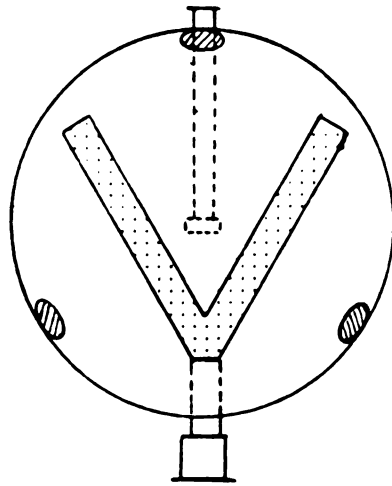


Figure 5-8i. The minimum velocity regions of the Y-duct perforated floor system.



5.7 THREE-DIMENSIONAL PRESSURE AND VELOCITY DISTRIBUTION DISPLAYS

The main purpose of this section is to use the results from the cutting planes to generate three-dimensional displays which support the two-dimensional graphic results.

SURFACE II GRAPHICS SYSTEM at the Computer Center (Michigan State University) was used to modify this three-dimensional display as detailed in Section 4.1-3. The data input were collected from spatial coordinate data points (x,y,z) at specified pressure and velocity values on the cutting planes. Vertical cutting planes parallel to the cutting plane type 2-1, 3-1, and 4-1P were used. There was no need to display the pressure and velocity distribution in three-dimensions for the total perforated floor system since the pressure and velocity are uniform and easily understood in the two-dimensional display.

The data points from eight up to twenty cutting planes were used, depending on the size of the grain storage. The larger storages need more data points and cutting planes. The degree of accuracy and smoothness of the surface displayed depend upon the number of input data points. A large number of data points gave a higher degree of accuracy and smoothness but it also required a lot of computing time to generate the grid matrix.

The three-dimensional graphic program allows the display to be viewed for any angle, any elevation, and any distance. The descriptive statement at the top of the three-dimensional displays, Figures 5-9a through 5-14c, gives

* 3-D PRESSURE DISTRIBUTION (.5 OF DUCT PRESSURE), STRAIGHT DUCT
PLOT NO. 1 DATE 03/14/83 TIME 18.49.28
AZIM = 30.0 ELEV = 40.0 DIST = 100

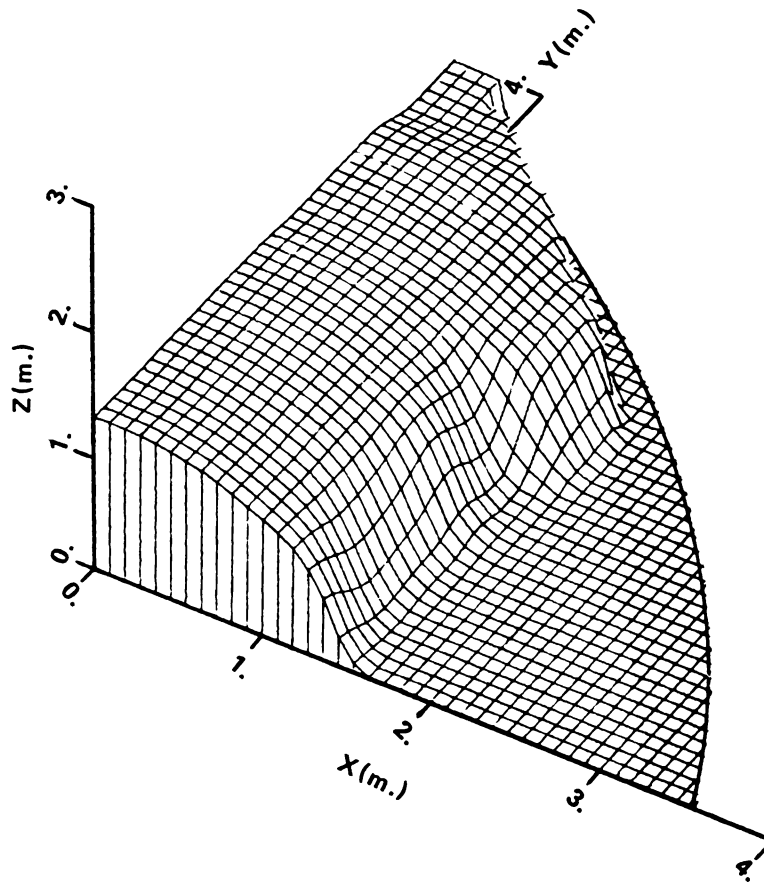


Figure 5-9a. Constant pressure surface for the straight duct perforated floor system (at azimuth = 30).

✱ 3-D PRESSURE DISTRIBUTION(.5 OF DUCT PRESSURE), STRAIGHT DUCT
PLOT NO. 2 DATE 03/14/83 TIME 18.49.49
AZIM = 115.0 ELEV = 40.0 DIST = 100

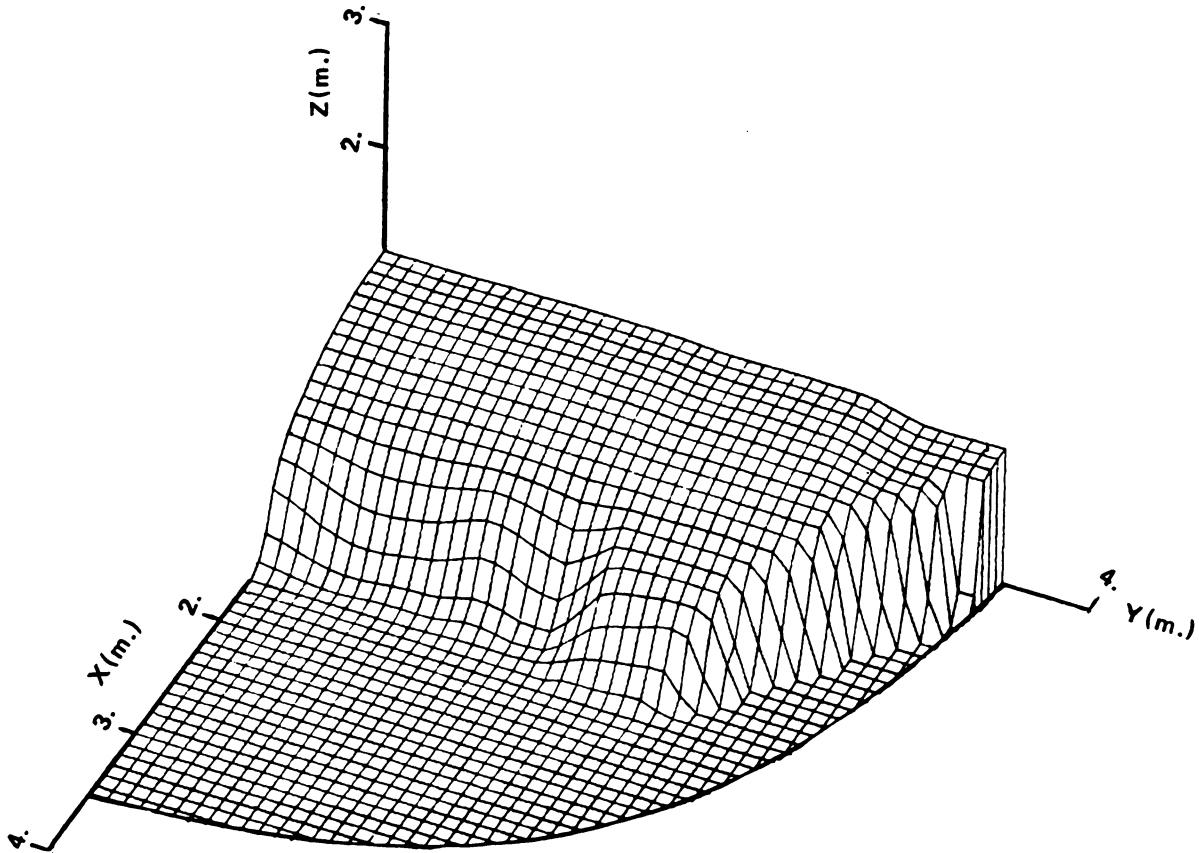


Figure 5-9b. Constant pressure surface for the straight duct perforated floor system (at azimuth = 115).

3-D PRESSURE DISTRIBUTION (.5 OF DUCT PRESSURE), STRAIGHT DUCT
PLOT NO. 3 DATE 03/14/83 TIME 18.50.09
AZIM = -30.0 ELEV = 40.0 DIST = 100

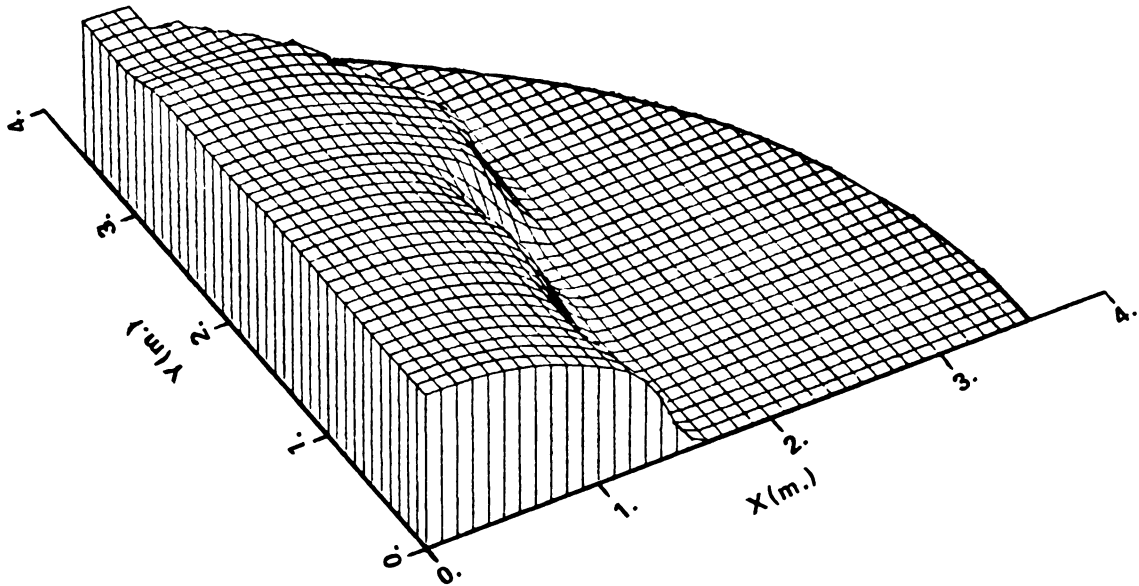


Figure 5-9c. Constant pressure surface for the straight duct perforated floor system (at azimuth = -30).



*** 3-D VELOCITY DISTRIBUTION (AT 3.6 M/MIN), STRAIGHT DUCT ***
PLOT NO. 1 DATE 03/12/83 TIME 01.26.27
AZIM = 30.0 ELEV = 40.0 DIST = 100

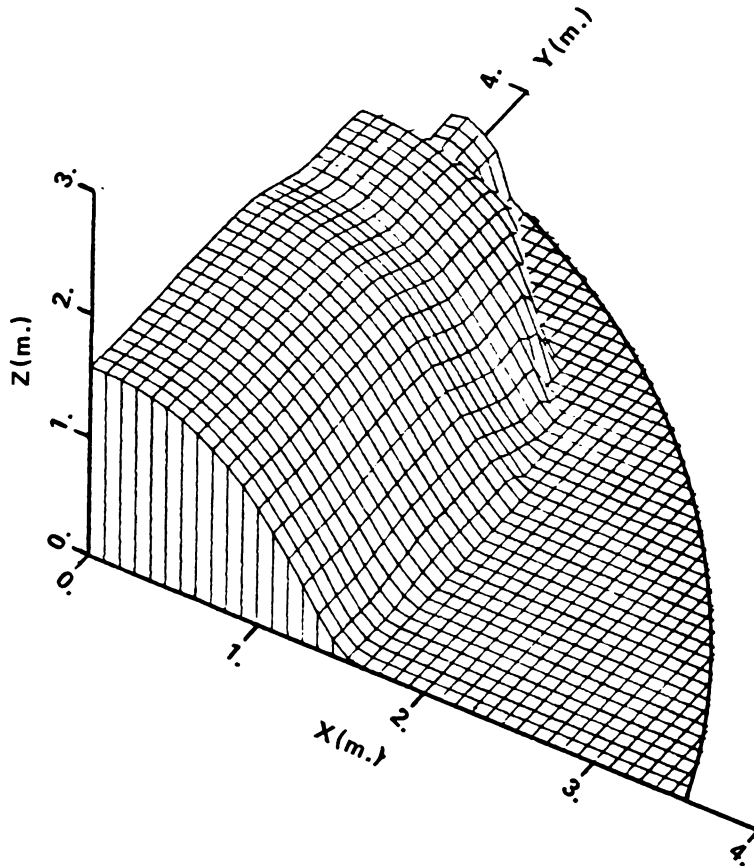


Figure 5-10a. Constant velocity surface for the straight duct perforated floor system (at azimuth = 30).

*** 3-D VELOCITY DISTRIBUTION (AT 3.6 M/MIN). STRAIGHT DUCT ***
PLOT NO. 2 DATE 03/12/83 TIME 01.26.15
AZIM = 115.0 ELEV = 40.0 DIST = 100

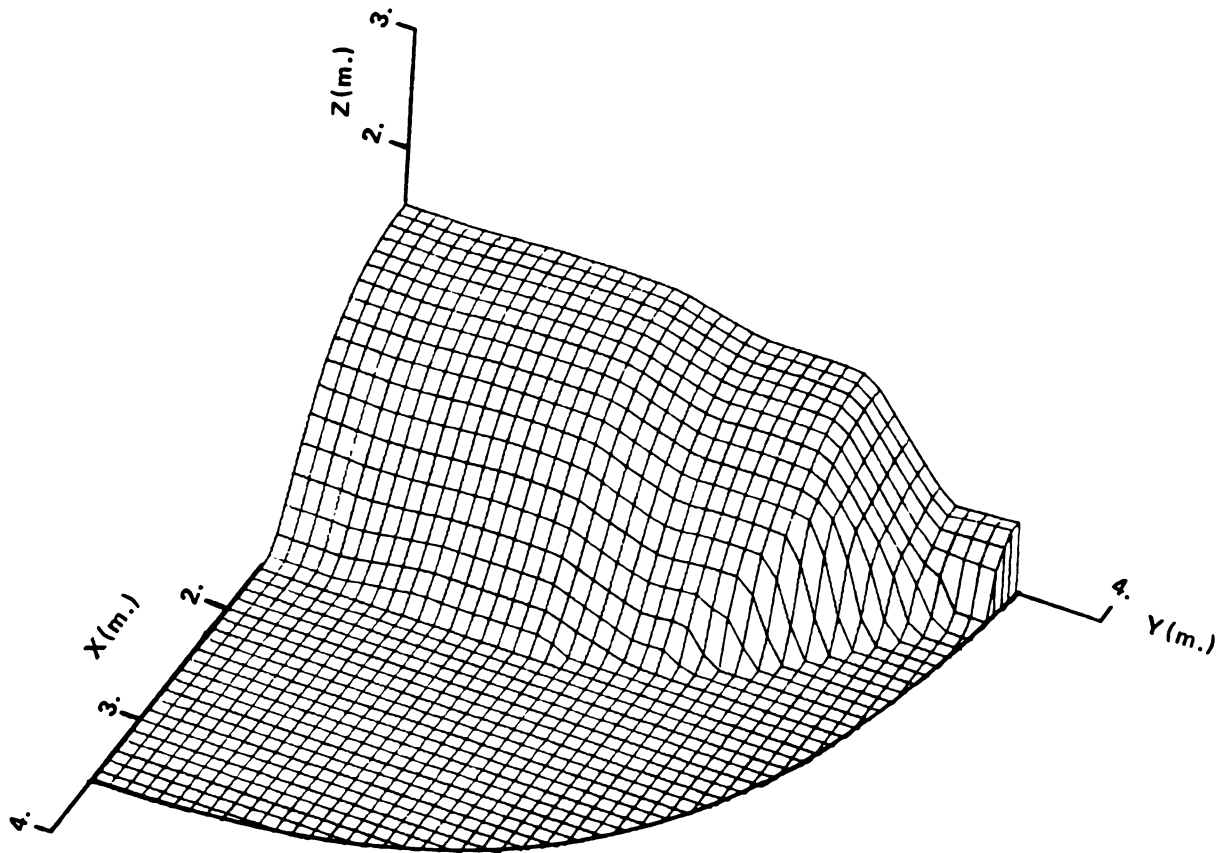


Figure 5-10b. Constant velocity surface for the straight duct perforated floor system (at azimuth = 115).



* * * 3-D VELOCITY DISTRIBUTION (AT 3.6 M/MIN). STRAIGHT DUCT * * *
PLOT NO. 3 DATE 03/12/83 TIME 01.26.03
AZIM = -30.0 ELEV = 40.0 DIST = 100

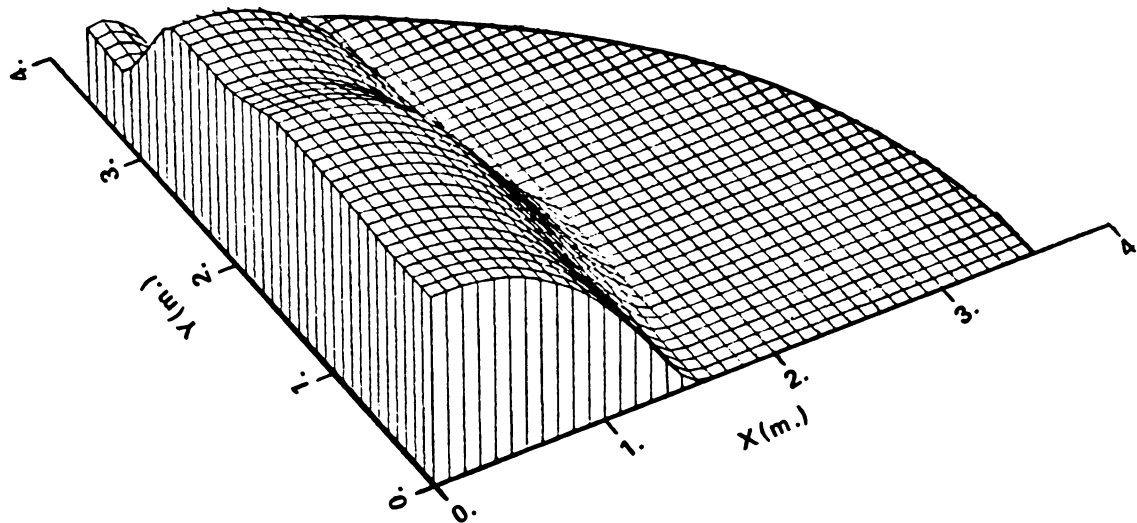


Figure 5-10c. Constant velocity surface for the straight duct perforated floor system (at azimuth = -30).



* 3-D PRESSURE DISTRIBUTION(0.70 OF DUCT PRESSURE).SQUARE DUCT
PLOT NO. 1 DATE 03/12/83 TIME 17.45.12
AZIM = 30.0 ELEV = 40.0 DIST = 100

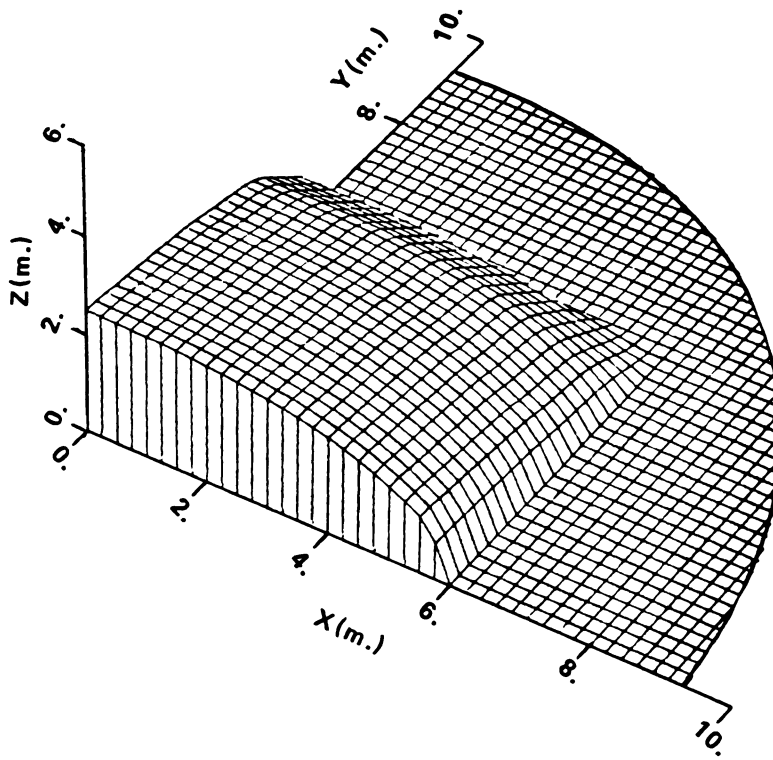


Figure 5-11a. Constant pressure surface for the square duct perforated floor system (at azimuth = 30).

✱ 3-D PRESSURE DISTRIBUTION (0.70 OF DUCT PRESSURE), SQUARE DUCT
PLOT NO. 2 DATE 03/12/83 TIME 17.45.33
AZIM = 115.0 ELEV = 40.0 DIST = 100

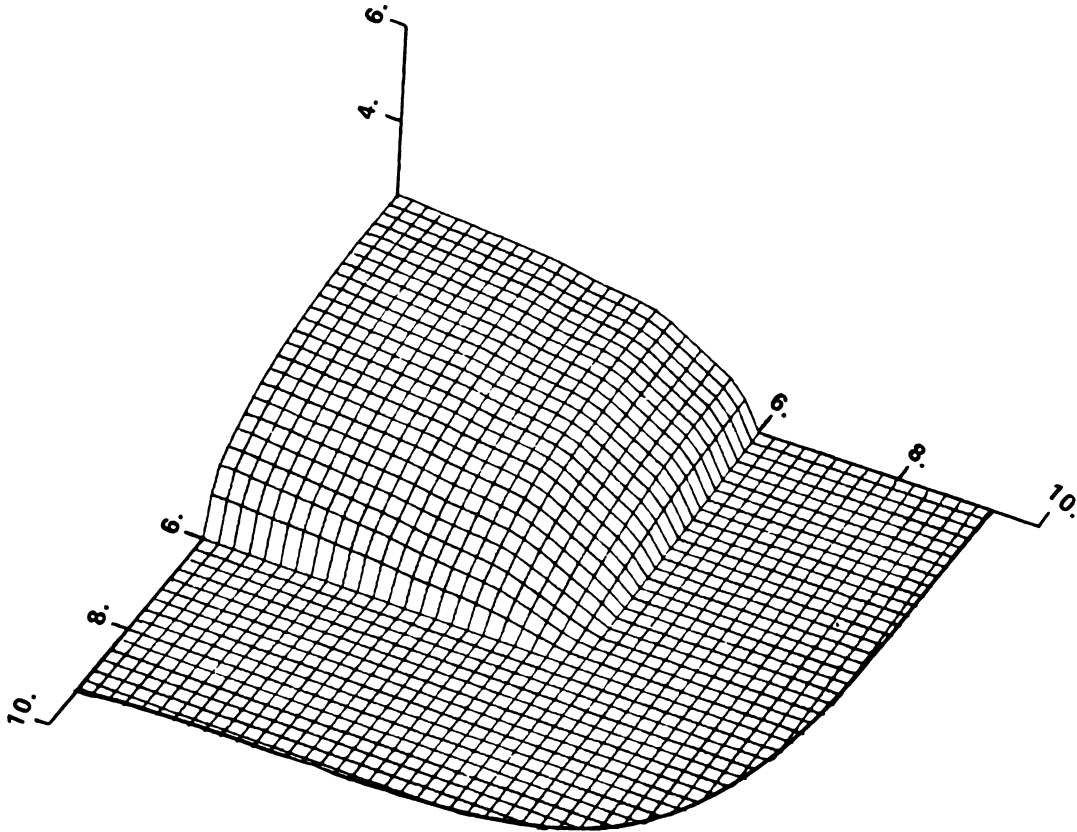


Figure 5-11b. Constant pressure surface for the square duct perforated floor system (at azimuth = 115).

* 3-D PRESSURE DISTRIBUTION(0.70 OF DUCT PRESSURE), SQUARE DUCT
PLOT NO. 3 DATE 03/12/83 TIME 17.45.53
AZIM = -30.0 ELEV = 40.0 DIST = 100

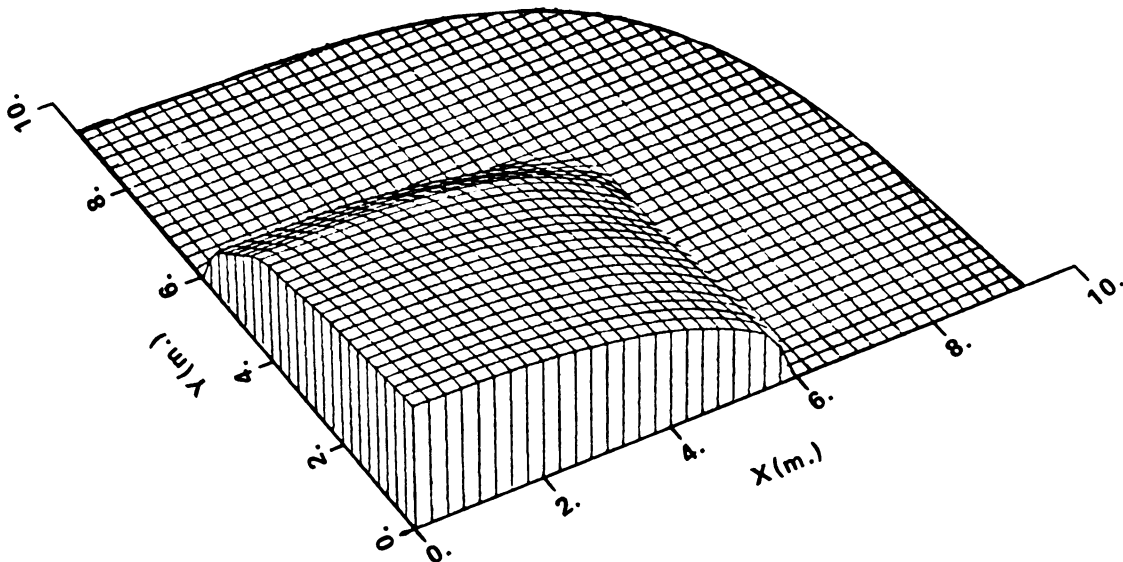


Figure 5-11c. Constant pressure surface for the square duct perforated floor system (at azimuth = -30).

* * * 3-D VELOCITY DISTRIBUTION (AT 2.4 M/MIN), SQUARE DUCT * * * *
PLOT NO. 1 DATE 03/14/83 TIME 12.38.44
AZIM = 30.0 ELEV = 40.0 DIST = 100

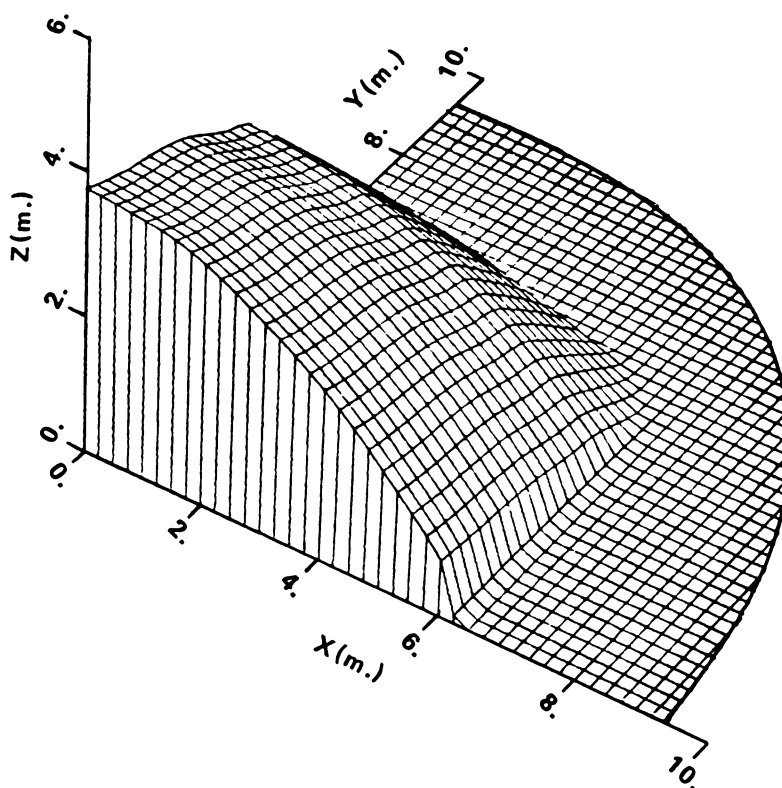


Figure 5-12a. Constant velocity surface for the square duct perforated floor system (at azimuth = 30).



*** 3-D VELOCITY DISTRIBUTION (AT 2.4 M/MIN). SQUARE DUCT ***
PLOT NO. 2 DATE 03/14/83 TIME 12.39.05
AZIM = 115.0 ELEV = 40.0 DIST = 100

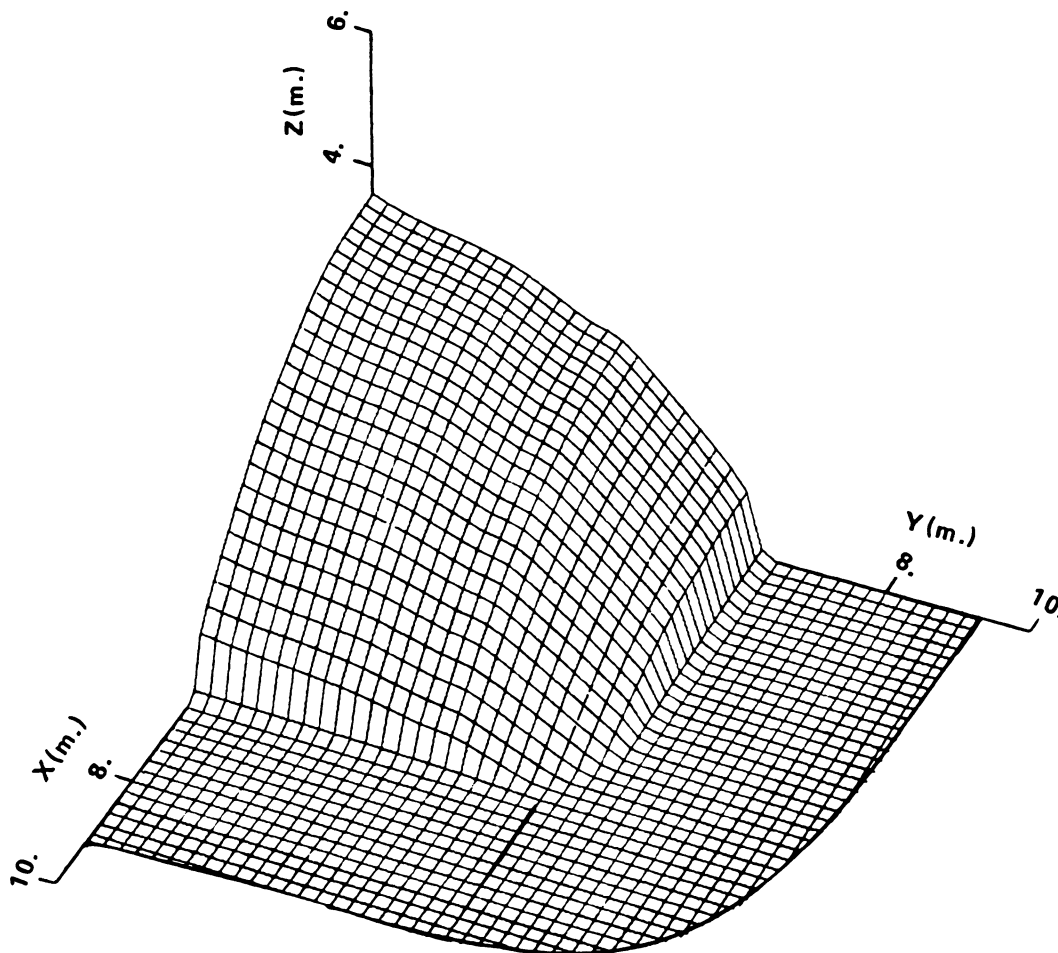


Figure 5-12b. Constant velocity surface for the square duct perforated floor system (at azimuth = 115).

*** 3-D VELOCITY DISTRIBUTION (AT 2.4 M/MIN), SQUARE DUCT ***
* * * * *
PLOT NO. 3 DATE 03/14/83 TIME 12.39.22
AZIM = -30.0 ELEV = 40.0 DIST = 100

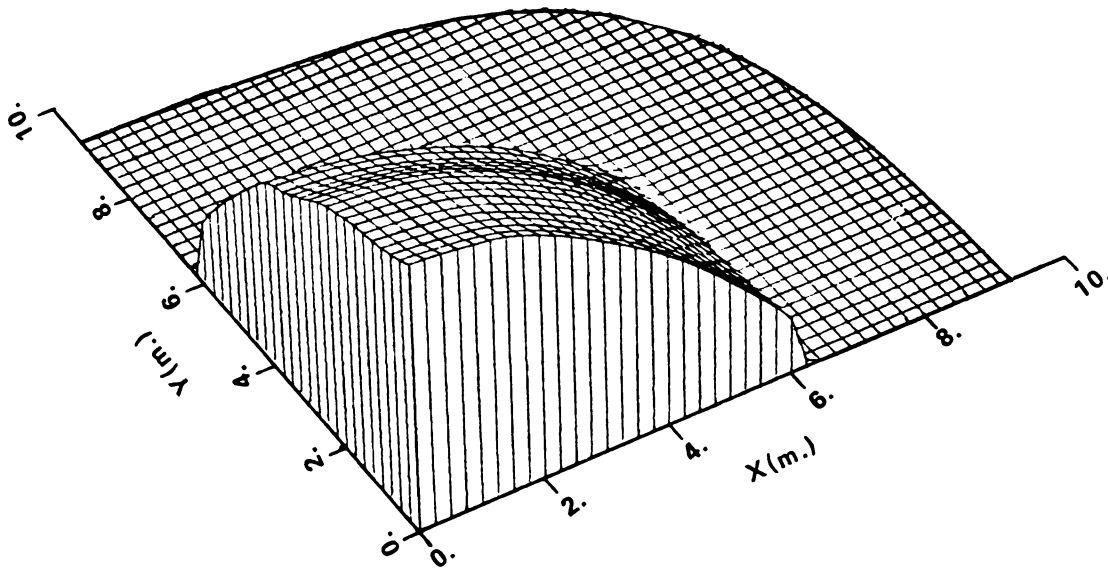


Figure 5-12c. Constant velocity surface for the square duct perforated floor system (at azimuth = -30).

3-D PRESSURE DISTRIBUTION (0.70 OF DUCT PRESSURE).Y-DUCT
PLOT NO. 1 DATE 03/14/83 TIME 12.41.38
AZIM = 30.0 ELEV = 40.0 DIST = 100

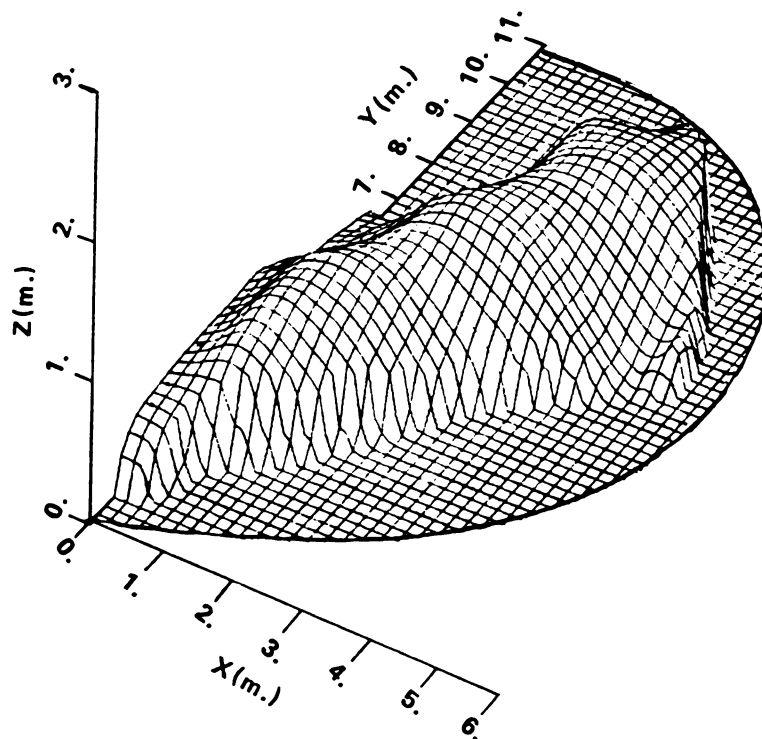


Figure 5-13a. Constant pressure surface for the Y-duct perforated floor system (at azimuth = 30).

3-D PRESSURE DISTRIBUTION (0.70 OF DUCT PRESSURE).Y-DUCT.
PLOT NO. 2 DATE 03/14/83 TIME 12.42.01
AZIM = 115.0 ELEV = 40.0 DIST = 100

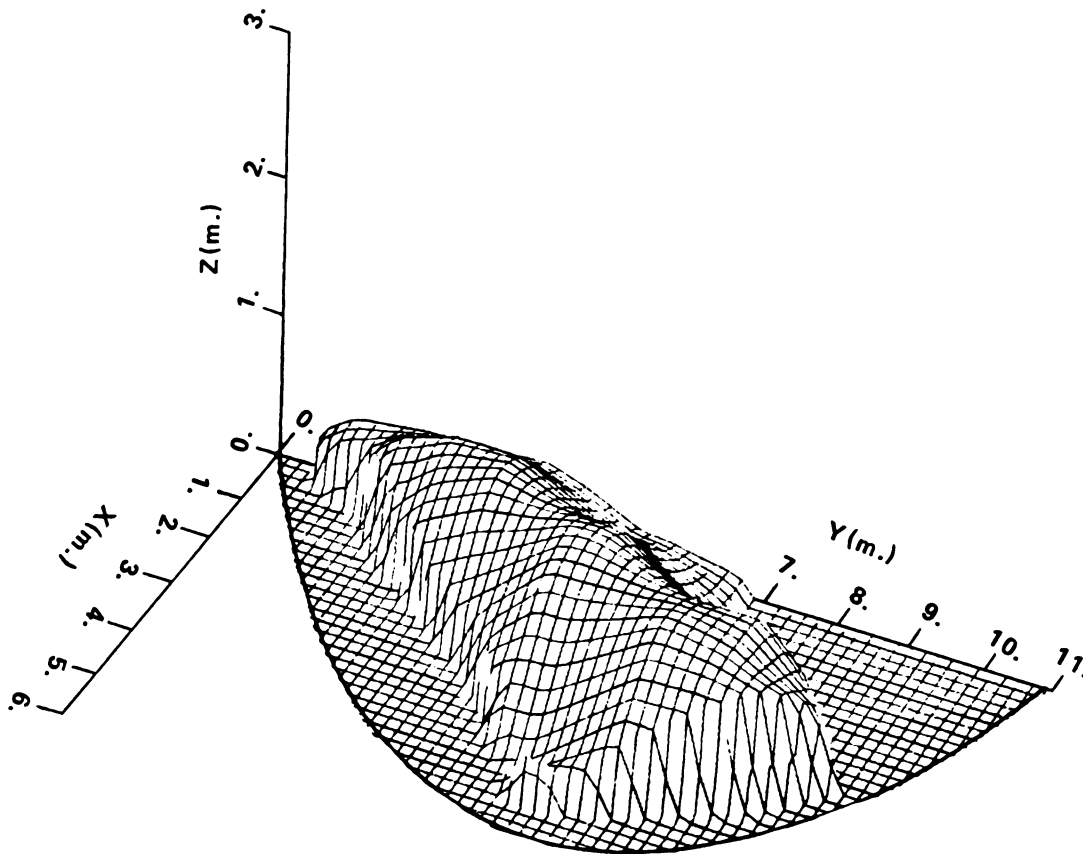


Figure 5-13b. Constant pressure surface for the Y-duct perforated floor system (at azimuth = 115).

3-D PRESSURE DISTRIBUTION (0.70 OF DUCT PRESSURE), Y-DUCT
PLOT NO. 3 DATE 03/14/83 TIME 12.42.29
AZIM = -30.0 ELEV = 40.0 DIST = 100

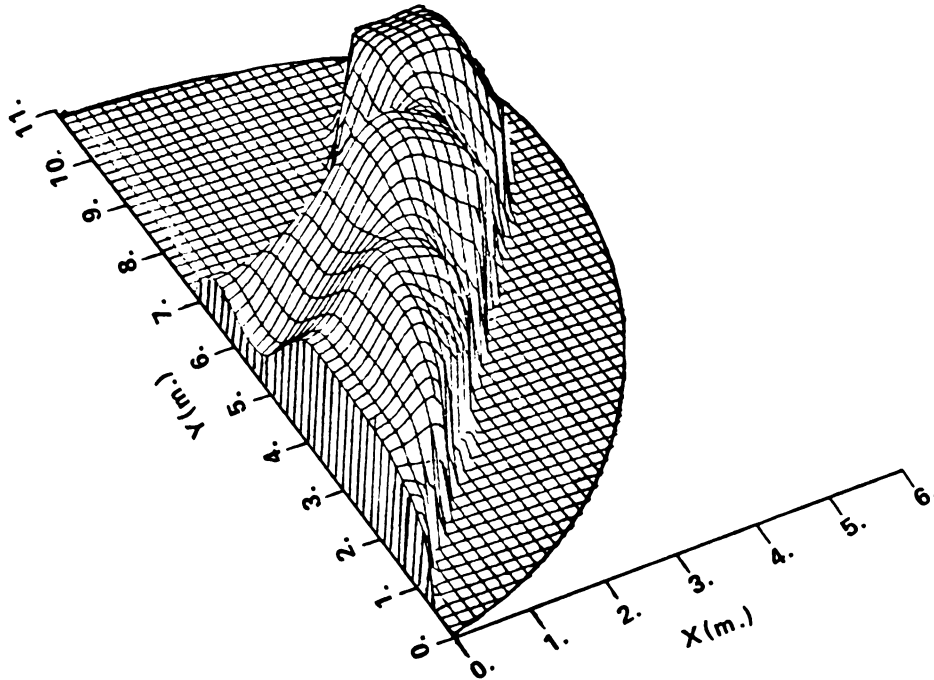


Figure 5-13c. Constant pressure surface for the Y-duct perforated floor system (at azimuth = -30).

*** 3-D VELOCITY DISTRIBUTION(AT 3.0 M/MIN.) Y-DUCT ***
* * * * *
PLOT NO. 1 DATE 03/11/83 TIME 17.13.17
AZIM = 30.0 ELEV = 40.0 DIST = 100

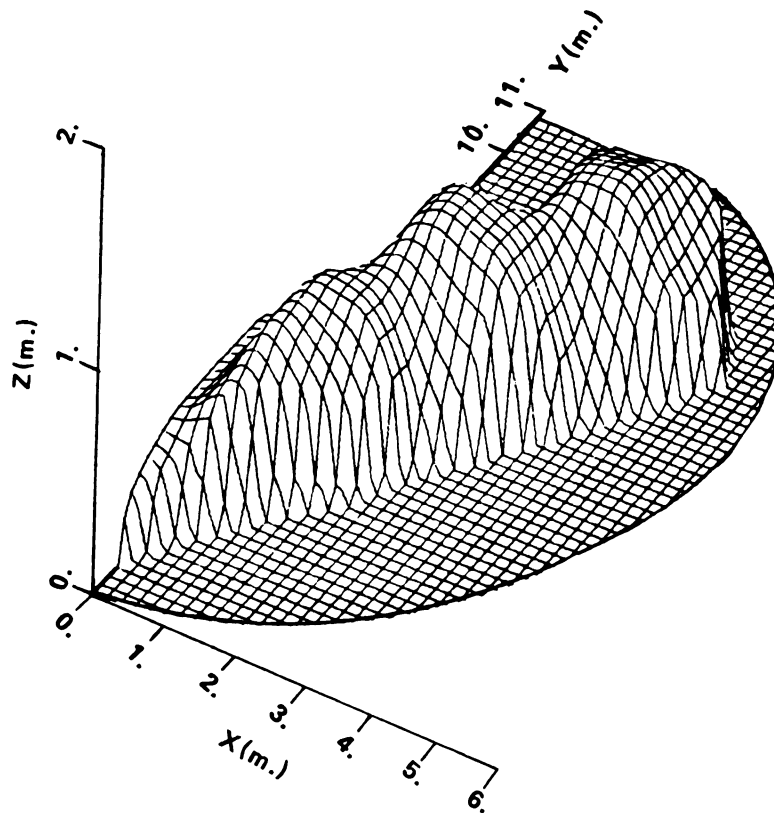


Figure 5-14a. Constant velocity surface for the Y-duct perforated floor system (at azimuth = 30).

*** 3-D VELOCITY DISTRIBUTION (AT 3.0 M/MIN.) Y-DUCT ***
* PLOT NO. 2 DATE 03/11/83 TIME 17.14.22
AZIM = 115.0 ELEV = 40.0 DIST = 100

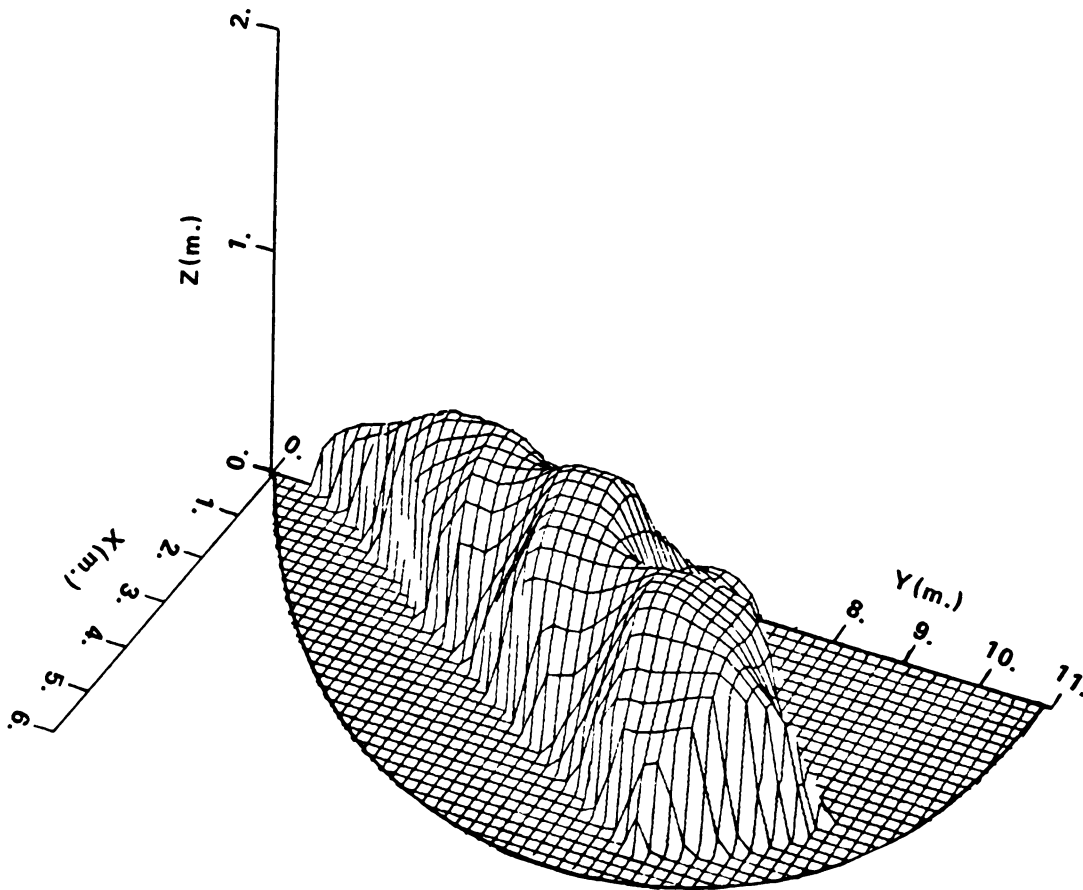


Figure 5-14b. Constant velocity surface for the Y-duct perforated floor system (at azimuth = 115).



*** 3-D VELOCITY DISTRIBUTION(AT 3.0 M/MIN.),Y-DUCT ***
* * * * *
PLOT NO. 3 DATE 03/11/83 TIME 17.15.18
AZIM = -30.0 ELEV = 40.0 DIST = 100

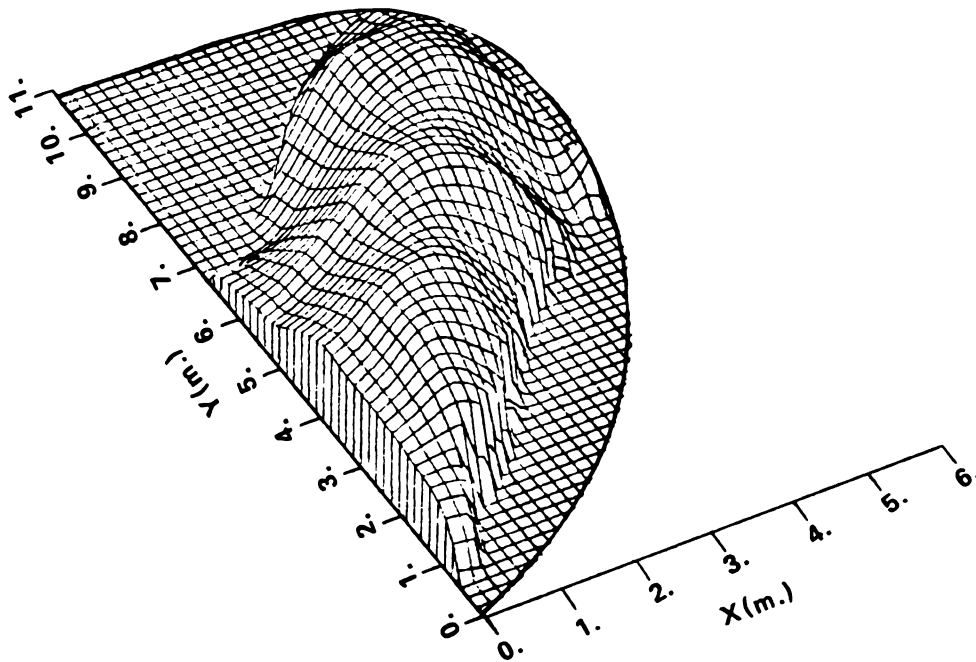


Figure 5-14c. Constant velocity surface for the Y-duct perforated floor system (at azimuth = -30).

the viewing point information including the type of the grain storage and pressure or velocity value to be displayed. The same viewing points were used for each bin analyzed. The pressure and velocity values displayed were selected large enough to hit the floor of the grain storage in order to be able to see the shape and its behavior clearly.

The following abbreviations need to be defined for better understanding the three-dimensional displays.

Azimuth (AZIM) defines the observer's viewing angle from the grid diagram. The parameter is expressed in degrees of rotation from the south (y-axis).

Elevation (ELEV) defines the elevation of the observer's view point above the grid diagram.

Distance (DIST) defines the distance (in map units of x and y) from the point of observation to the center of the grid diagram.

Because of symmetry, only a quarter section of the straight duct and square duct perforated floor system are displayed while a half section of the Y-duct perforated floor system is displayed.

The three-dimensional pressure distribution displays of the straight duct perforated floor system at 50% of the perforated floor pressure were presented in Figures 5-9a through 5-9c. The pressure is quite uniform along the length of duct (in the y direction) but it decreases rapidly in the x-direction. The three-dimensional pressure distribution at y equal zero (along the x-axis) in Figures 9-

5a and 9-5c is matched very well with the two-dimensional pressure distribution display in Figure 5-6c.

The velocity distributions of the straight duct perforated floor system at 3.6 m/min. are shown in Figure 5-10a through 5-10c. The velocity decreases rapidly in all directions beyond the end of the perforated floor. Again, the three-dimensional velocity distribution displays at y equal zero (along the x -axis) in Figure 5-10a and 5-10c can be compared favorably with the two-dimensional velocity distribution (at 3.6 m/min.) in Figure 5-6f.

Note that the surfaces of the three-dimensional displays are smoother than the constant pressure or velocity lines in the two-dimensional displays because the three-dimensional computer program uses arithmetic averaging (or smoothing) of adjacent z values in the grid matrix. The purpose of smoothing is to eliminate undesired "noise" or small variation scale variability that may be present in the original grid matrix (details in Sampson, 1978).

Figures 5-11a through 5-11c show the pressure distribution at 70% of the perforated floor pressure for the square duct perforated floor system. The pressure decreases smoothly as the distance increases from the center of the perforated floor.

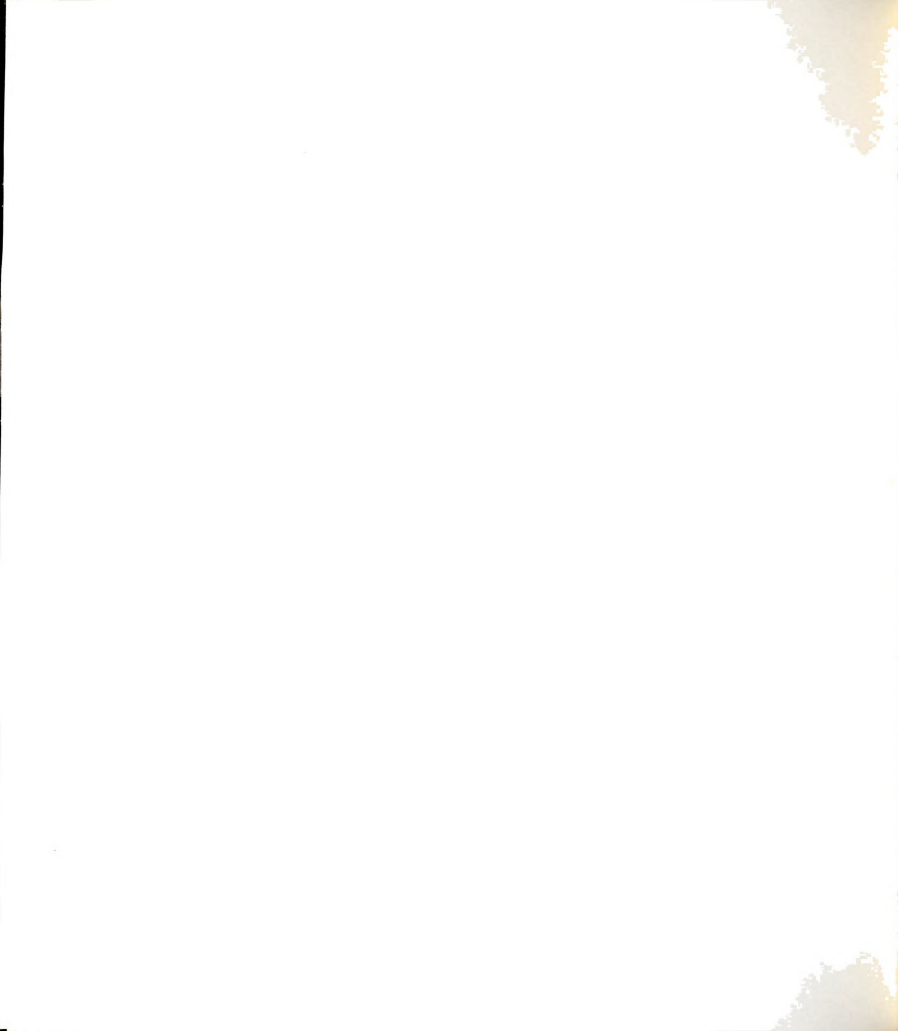
The velocity distribution at 2.4 m/min. for the square duct perforated floor system is presented in Figures 5-12a through 5-12c. The velocity gradient is quite high near the edge of the perforated floor. Both the pressure and velocity distributions are nearly square in shape. The

magnitude and shape of the pressure (or velocity) surfaces along the x- and y- axis are the same.

The three-dimensional pressure and velocity displays of the square duct perforated floor system in Figures 5-11a through 5-11c and Figures 5-12a through 5-12c match very well with the two-dimensional displays (at the same pressure and velocity values) in Figures 5-7c and 5-7f, respectively. A small variation is due to the smoothing calculations for the grid matrix generating process.

The most complicated configuration in this study is the Y-duct perforated floor system. Twenty vertical cutting planes were used to obtain enough data points to cover a half section of this grain storage system. Figures 5-13a through 5-13c show the three-dimensional pressure distribution displays at 70% of the perforated floor pressure of the Y-duct perforated floor system. It is quite clear that the pressure moves along the perforated floor. The pressure tends to spread upward along the y-direction and it decreases rapidly at the end of perforated floor. These three-dimensional displays match quite well with the two-dimensional displays (70% pressure line) in Figures 5-8c and 5-8d.

The three-dimensional velocity distribution displays for 3.0 m/min. of the Y-duct perforated floor system are presented in Figures 5-14a through 5-14c. The velocity moves along the perforated floor and tends to spread upward in the y-direction in the same manner as pressure. The three-dimensional displays in Figures 5-14a and 5-14c compare



favorably with the two-dimensional displays (at 3.0 m/min. line) in Figures 5-8f and 5-8g. Again a small variation exists because of the smoothing calculations for the grid matrix generating process.

The surfaces of the three-dimensional pressure and velocity distribution displays for the Y-duct perforated floor system are not as smooth as the surfaces of the three-dimensional pressure and velocity displays for the straight duct and square duct perforated floor system even when more data points are used.

Note that the maximum magnitude of pressure in the z direction for the Y-duct perforated floor system (Figure 5-13a) occurs at a height of about 1.0 m. It is only about 40% of the maximum magnitude of pressure in the z direction for the square duct perforated floor system (Figure 5-11a) at the same 70% of the perforated floor pressure (350 pascals).

CHAPTER VI

CONCLUSIONS

The finite element method was used to solve the three-dimensional nonlinear airflow equation. The computer program developed was capable of calculating the pressure distribution, pressure gradient and velocity distribution within a cylindrical grain storage but the program can be modified to handle other shapes of grain storages.

Four types of perforated floor system for the cylindrical grain storage were studied. Shelled corn was the grain media. The cutting plane technique was used in order to display the two-dimensional pressure and velocity distributions within the grain storages. The three-dimensional pressure and velocity distribution displays were developed from the numerical results of the cutting planes to improve visibility and for better understanding the airflow patterns.

Based on the numerical and graphical results in two and three-dimensions, it is concluded that:

- 1) The finite element method is an acceptable solution tool and capable of obtaining results for the three-dimensional nonlinear airflow problem a cylindrical grain storage.

- 2) SURFACE II is an appropriate computer graphic software to plot the three-dimensional display. It is not complicated to use or modify. The contents of the grid matrix need to be stored in local code file in order to reduce execution costs for run of SURFACE II which use the same data set.
- 3) The velocity in vertical (z) direction plays an important role in the velocity distribution within the cylindrical grain storage. Apparent (or resultant) velocity was used for all the velocity distribution displays.
- 4) The minimum velocity regions of the grain storages under study were located.

Two minimum velocity regions for the straight duct perforated floor system are located on the floor of the bin at the greatest distance from the center of the bin at the greatest distance from the center of the perforated floor and perpendicular to the length of the perforated floor (Figure 5-6i).

There are four minimum velocity regions for the square duct perforated floor system. These regions are located on the floor of the bin at the greatest distance perpendicular to the perforated floor (Figure 5-7i).

Three minimum velocity regions for the Y-duct perforated floor system are located at the intersection between the floor and the bin wall. Two are located at the greatest possible distance perpendicular to the sides of perforated floor.

The other region is on the axis of symmetry at the top of Y-shape (Figure 5-8i).

- 5) The pressure and velocity distributions of the cylindrical grain storage are mostly effected by the perforated floor patterns.

CHAPTER VII
SUGGESTIONS FOR FUTURE WORK

Future work should be aimed at using the techniques developed in this study to analyze the following:

- 1) Simulation using the actual perforated floor pressure for each type of the grain storage.
- 2) Substitute alternate grains for shelled corn (i.e., soybeans, rice, wheat, etc.)
- 3) Study the effect of perforated floor configuration on the minimum velocity regions.
- 4) Study the effect of the top configuration of the grain storage.
- 5) Study the effect of nonuniform grain distribution.

The results of this study would also be useful references for developing a similar study for an optimum or a practical grain storage.

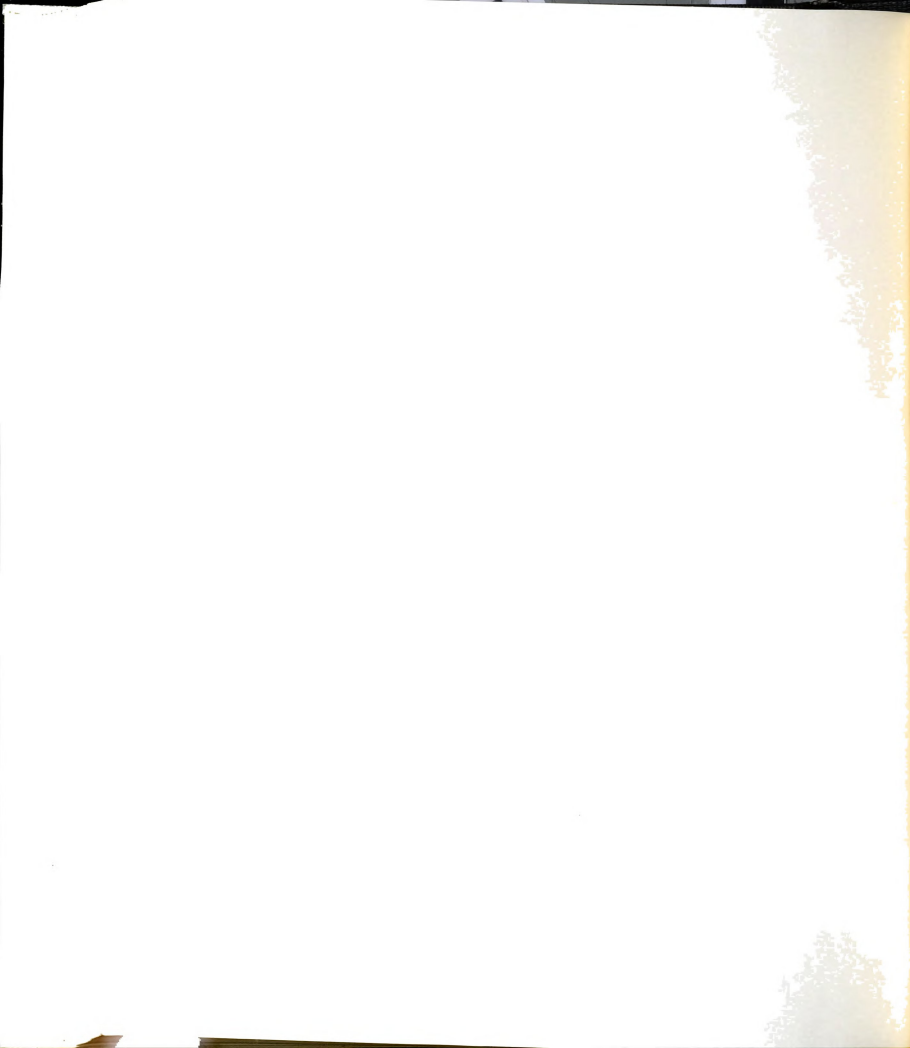


BIBLIOGRAPHY

- Barrowman, R. and Boyce, D.S., 1966. Air Distribution from Lateral Ducts in Barley, *Journal of Agricultural Engineering Research*, 11:243-247.
- Brook, R. C., 1979. Aeration System for Dry Grain, *Agricultural Engineering Information, eais.*, No. 391, File No. 18.151, Michigan State University, East Lansing, Michigan.
- Brooker, D. B., 1958. Lateral Duct Airflow Patterns in Grain Drying Bins, *Agricultural Engineering*, 39:348-351.
- Brooker, D. B., 1961. Pressure Patterns in Grain-Drying System Established by Numerical Mehtods, *Transactions of ASAE*, 4:72-77.
- Brooker, D. B., 1969. Computing Air Pressure and Velocity Distribution When Air Flow Through a Porous Medium and Nonlinear Velocity Pressure Relationships Exist, *Transactions of ASAE*, 12:118-120.
- Brooker, D. B., Bakker-Arkema, F. W., and Hall, C. W., 1981. *Drying Cereal Grains*, The AVI Publication Company, Incorporated, Connecticut, pp. 123-129.
- Bunn, J. M. and Hukill, W.V., 1963. Pressure Pattern Predictions for Nonlinear Airflow Trhough Porous Media, *Transactions of ASAE*, 6(1):32-36.
- Conte, S. D., and Boor, C. D., 1978. *Elementary Numerical Analysis*, McGraw-Hill, New York, pp. 86-90.
- Ergun, S., 1952. Fluid Flow Through Packed Columns, *Chemical Engineering*, 48:89-94.
- Foley, J. D., and Dam, A. V., 1982. *Fundamentals of Interactive Computer Graphics*, Addison-Wesley Publication Company, Reading, Massachusetts, pp. 245-252.
- Hornbeck, R. B., 1975. *Numerical Methods*, Quantum Publishers, Incorporated, New York, pp. 66-70.

- Iranmenesh, A. A., 1981. Numerical Simulation of Heat Transfer and Stress Analysis of Continuous casting, Ph.D. Dissertation, Michigan State University, East Lansing, Michigan, pp. 20-25.
- James, M. L., and Smith, G. M., 1975. Analog and Digital Computer Methods in Engineering Analysis, International Textbook, Scranton, Pennsylvania.
- Jindal, V. K., and Thomson, T. L., 1972. Air Pressure Patterns and Flow Paths in Two-Dimensional Triangular-Shaped pile of Sorghum Using Force Convection, Transactions of ASAE, 15:737-741.
- Lai, F. S., 1980. Three-Dimensional Flow of Air Through Nonlinear Grain Beds, Transactions ASAE, 23:729-734.
- Marchant, J. A., 1976a. Prediction of Fan Pressure Requirements in the Drying of Large Hay Bales, Journal of Agricultural Engineering Research, 21:333-346.
- Marchant, J.A., 1976b. The Prediction of Airflows in Crop Drying Systems by the Finite Element Method, Journal of Agricultural Engineering Research, 21:417-429.
- Noyes, R. T., 1967. Aeration for Safe Grain Storage, Co.-Extension Service, AE-71, Purdue University, LaFayette, Indiana.
- Pierce, R. O., and Thomson, T. L., 1975. Airflow Patterns in Conical-Shaped Piles of Grain, Transactions of ASAE 18:946-949.
- Rogers, D. F., and Adams, J. A., 1976. Mathematical Elements for Computer Graphics, McGraw-Hill, New York.
- Sampson, R. J., 1978. SURFACE II Graphics System, Computer Services Section, Kansas Geological Survey, Lawrence, Kansas.
- Segerlind, L. J., 1976. Applied Finite Element Analysis, John Wiley and Sons, New York.
- Segerlind, L. J., 1982. Solving the Nonlinear Airflow Equation, American Society Agricultural Engineering, paper 82-3017.
- Shedd, C. K., 1951. Some New Data on Resistance of Grain to Airflow, Agricultural Engineering, 32:493-496.

- Smith, E. A., 1982. Three-Dimensional Analysis of Air Velocity and Pressure in Beds of Grain and Hay, *Journal of Agricultural Research*, 27:101-117.
- Smith, G. D., 1975. *Numerical Solution of Partial Differential Equations*, Oxford, London.
- Steven, L. H., 1978. *Plotting and Graphics, User's Guide Volume VII*, Computer Laboratory, Michigan State University, East Lansing, Michigan.
- Zienkiewicz, O. C., 1978. *The Finite Element Method*, McGraw-Hill Publication, 3rd Ed.



MICHIGAN STATE UNIV. LIBRARIES



31293006394054